Nanoparticles in the MnO_x-SiO_2 System for the Applications to the Combinational Anticancer Therapies of Immunotherapy and Other Therapies

MnO_x-SiO_2系ナノ粒子の免疫療法および他療法との併用療法への応用

February 2023

Xueping Yu

余　雪萍

Nanoparticles in the MnO_x-SiO_2 System for the Applications to the Combinational Anticancer Therapies of Immunotherapy and Other Therapies

MnO_x-SiO_2系ナノ粒子の免疫療法および他療法との併用療法への応用

February 2023

Waseda University

Graduate School of Creative Science and Engineering

Department of Earth Sciences, Resources and Environmental Engineering

Research on Applied Mineralogy

Xueping Yu

余　雪萍

Abstract

Different anticancer therapies have been developed to treat cancers. Although many good outcomes have been achieved in both clinical and preclinical practice, most single or combinational anticancer therapies are still faced with different limitations in inhibiting tumor growth due to the complex TME. Moreover, it is much more difficult to inhibit tumor metastasis, the main reason for death from cancers, due to the immunosuppressive status in tumor tissue. Therefore, it may be promising to improve the efficiency of present existing anticancer therapies on both tumor growth and tumor metastasis through regulating TME and activating immune responses. In this thesis, Mn-based and Si-based nanomaterials were adopted and synthesized into different nanoparticles to enhance the effect of the combinational anticancer therapies of immunotherapy and other kinds of present existing anticancer therapies. These synthesized Mn-Si-based NPs showed regulation functions to TME and potential in immune activation. For in vivo anticancer effect, these synthesized Mn-Si-based NPs induced an obvious inhibitory effect on both the primary tumors and metastatic tumors in different combinational anticancer therapies using a bilateral animal model. The effect of Mn-Si-based nanomaterials-enhanced different combinational anticancer therapies were described in the following.

First, Mn was coated onto Si-based nanoparticles to form the first kind of Mn-Si-based NPs (SM NPs) for enhancing the combinational anticancer therapy of immunotherapy and radiotherapy. SM NPs showed obvious regulation functions to

TME, including relieving hypoxia status through the catalytical properties of MnO_2 to H_2O_2, breaking the redox balance through the ROS generation and GSH depletion, as well as immune activation. SM NPs enhanced the cell-killing effect of RT due to enhanced DNA damage. In a bilateral animal model, the combination of radiation and SM NPs and the combination of radiation, SM NPs, and the anti-CTLA-4 antibody showed a clearly better inhibitory effect on the growth of primary tumors and distant untreated tumors, compared with radiation alone and the combination of radiation and the anti-CTLA-4 antibody, respectively.

Second, Mn was doped into MSNs to form the second kind of Mn-Si-based NPs (MM NPs) for enhancing the combinational anticancer therapy of immunotherapy and chemotherapy. Mn-doping not only endowed MSNs with regulation functions to TME through oxygenation, generation of highly cytotoxic reactive oxygen species of •OH, and depletion of GSH, enhanced immune activation capability, but also improved the degradation of MSNs, one of the limitations for their clinical application in chemotherapy. In a bilateral animal model, MM NPs obviously enhanced the inhibitory effect on the growth of distant untreated tumors and improved immune activation-related cytokines secretion from splenocytes when combined with the immune checkpoint blockers of the anti-CTLA-4 antibody.

Third, MM NPs were further used to load a photo agent of IR 780. IR 780-loaded MM NPs were further coated with Mn to form the third kind of Mn-Si-based NPs (IMM) for enhancing the combinational anticancer therapy of immunotherapy and

phototherapy. Compared with IR 780 alone, IR 780-loaded IMM showed better photostability, indicated by the better photothermal capability in generating heat even after 4 cycles of laser irradiation and stored in darkness for 2 weeks at room temperature, and the better photodynamic capability in producing singlet oxygen species even after stored in darkness for 2 weeks at room temperature. Moreover, IMM also showed obvious regulation functions to TME, including oxygenation, generation of highly cytotoxic reactive oxygen species of •OH, and depletion of GSH. In a bilateral animal model, the combination of an 808nm laser irradiation and IMM obviously induced a better inhibitory effect on both the primary tumors and distant untreated tumors, compared with the combination of an 808nm laser irradiation and IR 780.

In the different combinational anticancer therapies, Mn-Si-based NPs played an important role in regulating TME through oxygenation, ROS generation, and GSH depletion and immune activation, which synergistically contributed to the enhanced inhibitory effect on both primary tumors and metastatic tumors. Therefore, this study may provide a new strategy for improving the inhibitory effect of present existing anticancer therapies on tumor growth and metastasis.

Key words: Manganese, Silica, Tumor microenvironment, Immune activation, Radiotherapy, Chemotherapy, Phototherapy, Immunotherapy

Contents

Abbreviations

Abbreviations	Definition
RT	Radiotherapy
CDT	Chemodynamic Therapy
PTT	Photothermal Therapy
PDT	Photodynamic Therapy
Radio-immunotherapy	The combinational anticancer therapy of immunotherapy and radiotherapy
Chemo-immunotherapy	The combinational anticancer therapy of immunotherapy and chemotherapy
Photo-immunotherapy	The combinational anticancer therapy of immunotherapy and phototherapy
NPs	Nanoparticles
SM NPs	Mn-coated SiO_2 NPs
MSNs	Mesoporous Silica Nanoparticles
MM NPs	Mn-doped MSNs
IMM	Mn-coated IR 780-loaded MM NPs
LLC	Lewis Lung Carcinoma
MOC2	Mouse Oral Squamous Cell Carcinoma
DOX	Doxorubicin
PA	Photothermal Agents
PS	Photosensitizers
TME	Tumor Microenvironment
ROS	Reactive Oxygen Species
•OH	Hydroxyl Radical
GSH	Glutathione
GPx-4	Glutathione Peroxidase 4
LPO	Lipid Peroxide
ACT	Adoptive Cell Transfer
ICBs	Immune Checkpoint Blockers
PD-1	Programmed Cell Death 1
CTLA-4	Cytotoxic T Lymphocyte Antigen 4
MDSCs	Myeloid-derived Suppressor Cells
TAMs	Tumor-associated Macrophages
Tregs	Regulatory T Cells
Th 1 cells	T Helper 1 cells
HIF	Hypoxia-inducible Factor
NK cells	Natural Killer Cells
DCs	Dendritic Cells
CTLs	Cytotoxic T Lymphocytes

ICD	Immunogenic Cell Death
MHC - I	Major Histocompatibility Complex Class I
DAMPs	Damaged-associated Molecular Patterns
CD8/4	Cluster of Differentiation 8/4

Chapter 1 Introduction

1.1 Background

Cancer has been a dominant cause of death, which ranks as the first or second dominant cause of death for people before the age of 70 in 112 of 183 countries and third or fourth in 23 other countries, respectively [1]. The data from Globacan 2020 (Figure 1-1) showed that the estimated number of new cases and total deaths in 2020 from cancers was around 19 million and 10 million, respectively.

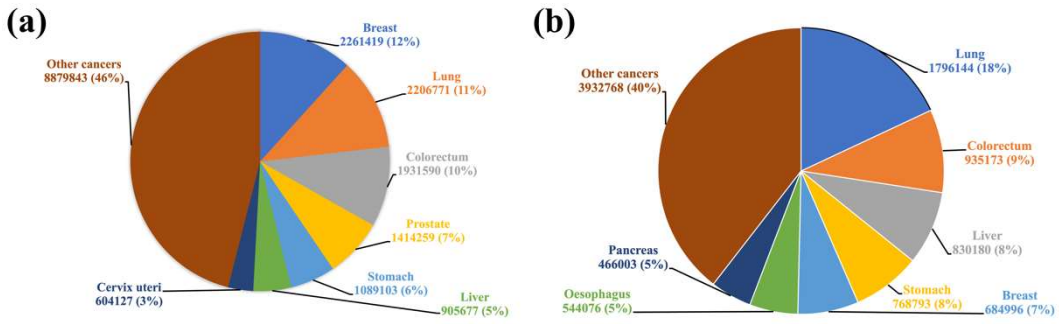

Figure 1-1 Estimated number of new cases (a) and deaths (b) in 2020 (world, both sexes, and all ages)

Nowadays, the clinically used anticancer therapies are still surgery, RT, and chemotherapy. Whereas these anticancer therapies are still faced with different limitations. Therefore, many efforts have been done to develop new anticancer therapies, such as PTT, PDT, CDT, and so on. Although these anticancer therapies have shown some good outcomes, their effects are still far from satisfactory due to the complex TME, which is usually featured with hypoxia, acidic pH value, elevated H_2O_2 level, and the powerful antioxidant system [2, 3]. For example, the high cell

proliferation and impaired vascularization-induced oxygen diffusion difficulty and hypoxia in TME [4] cause resistance to many anticancer therapies. Hypoxia can limit the effect of RT through decreasing the generation of oxygen-derived free •OH, slowing proliferation kinetics, and inducing genome changing [5]. Besides, hypoxia also causes drug resistance in chemotherapy through influencing the effect of some drugs that need cellular O_2, reducing the drug distribution, slowing down the cell cycle, and changing genomes [6]. Moreover, immune escape and metastasis also influence the efficiency of different anticancer therapies on both primary tumors and metastatic tumors. The metastatic tumors have been the main cause (around 90%) of death from cancers, rather than primary tumors [7], and only one out of five patients who are diagnosed with metastatic cancer can survive more than 5 years [8]. Metastatic tumors usually respond poorly to clinically used anticancer therapies, including surgery, RT, and chemotherapy [9, 10]. It is also suggested that some conventional anticancer therapies, like chemotherapy and RT, hinge their long-term efficiency on the ability to reinstate immunosurveillance [11]. Therefore, a new anticancer therapy named immunotherapy has been developed to focus on metastatic tumors, which takes effect through activating the host's immune systems [12, 13]. Immunotherapy includes different kinds of strategies, such as adoptive cell transfer (ACT), cytokines, and ICBs. For example, ICBs are developed to "unleash" powerful T cell responses [14], which have shown efficacy in many kinds of cancer, such as melanoma, non-small cell lung cancer, head and neck squamous cell carcinoma, and so on [15]. And one of the T cell immune

checkpoint molecules of CTLA-4 has been approved by the FDA in 2011, which is the first T cell immune checkpoint molecule to be clinically targeted and one of the most widely studied T cell immune checkpoint molecules including in preclinical and clinical experiments with an effect of prolonging the survival for metastatic melanoma to 10 years [16]. Although immunotherapy has shown efficacy in some patients, no immune responses (primary resistance) can be observed, or the immune responses couldn't keep a long time (acquired resistance) for most patients. For example, it has been reported that 50%-60% of patients showed low or no response to ICBs [17]. One of the major reasons for the low responses is related to the immunosuppressive TME, in which there are few T cells and a high number of immunosuppressive cells, including MDSCs, TAMs, and Tregs [18]. And the immunosuppressive TME is also related to the complex TME features. For example, the hypoxia in TME not only strongly limits the efficiency of RT and chemotherapy for primary tumors, but also affects the efficiency of immunotherapy for metastatic tumors [19-24]. Previous studies showed that hypoxia is related to the renewal of cancer stem cells, the transition from epithelial to mesenchymal, immune surveillance, and therapy resistance [25]. Specifically, hypoxia induces cellular responses of the HIF activation, which further induces expression of multidrug resistance protein, metabolic enzyme pyruvate kinase M2, production of vascular endothelial growth factor, angiogenesis, recruitment of tumor-associated macrophage, and suppression of cytotoxic CD 8-T and NK cells [25-27]. Besides, hypoxic cancer cells get energy through glycolysis and produce lactic, whose

accumulation further leads to an acidic pH value of TME, which also impedes the normal immune cells [28]. Moreover, the fast growth of cancer cells induces a high level of the by-product of ROS. On the one hand, the high-level ROS causes cell death, on the other hand, the high-level ROS promotes the formation of a powerful antioxidant system to maintain the redox balance and protect cells from death. GSH, one of the major antioxidants in the powerful antioxidant systems, is often considered as the most important non-enzymatic antioxidant in cells [29], which not only plays a role in maintaining ROS level in different ways to protect cancer cells from death and promote tumor progression but also affects the immune responses in many different anticancer therapies [30, 31]. Due to the role of ROS in both innate and adaptive immune responses, including promoting the maturation of DCs, inducing the activation and proliferation of effector T cells, and causing ICD (A kind of cell death modality that can stimulate the host's immune response using dead-cell antigens [32]), increase in GSH can decrease ROS level and influence the immune responses indirectly [33].

In conclusion, most of anticancer therapies are limited by the features of the complex TME and lack enough effect on inhibiting metastasis. Therefore, designing strategies to improve present existing anticancer therapies becomes more important than developing new anticancer therapies [34].

Firstly, combining different anticancer therapies with immunotherapy to synergistically inhibit the primary tumors and metastatic tumors can be one of the effective strategies to solve the limitation of most single anticancer therapies that are

not effective enough on metastasis inhibitory and cannot meet the actual treatment requirements [35]. For example, chemotherapeutic drugs can induce ICD to activate DCs and specific T-cell responses and enhance tumor immunogenicity [36-41], which is usually not enough to generate strong tumor immunogenicity and even has potential to induce metastases [35, 42-45]. Therefore, the strategy of combining immunotherapy with chemotherapy to acquire a higher level of anticancer immune responses and better anticancer effect has been studied widely and has induced some good outcomes [46]. Besides, RT has been also proven to have the potential to induce ICD, improve chemokines secretion, promote antigen promotion on MHC-I molecules and further stimulate immune responses, which is called an abscopal effect [47-50] and has been found in many different cancers, including melanoma [51], hepatocellular carcinoma [52], NSCLC [53], and renal cell carcinoma [54]. Whereas, it is seen in only 10% of cases in clinical practice [55]. Additionally, it has also been reported that RT can induce the inactivation of immune cells directly and the recruitment of MDSCs and Treg cells in TME to enhance the immune tolerance to the cancer cells [56, 57]. Interestingly, combining RT with ICBs makes the abscopal effect more common [58, 59]. Except for the conventional anticancer therapies, newly developed anticancer therapies like phototherapy have also been found to induce ICD and activate immune systems through releasing DAMPs recently. For example, an increase in body temperature induced by PTT has the potential to promote the homing of immune cells, the activation of immune cells of CTLs, DCs, and NK cells, and the inhibition of immune suppression [60].

Whereas the high temperature for rapid tumor ablation is unfavorable for immune activation. The tumor temperature above 45 ºC may induce damage to the vasculature, chemokines, and cytokines, thus influencing the strength of immune responses, which leads to a common case of relapse of large tumors [61]. Therefore the combinational anticancer therapy of immunotherapy and phototherapy has shown the potential to address this limitation [62, 63].

Secondly, using nanotechnology to regulate TME to a better status for anticancer therapies has also been considered to be a promising strategy to enhance the effect of different anticancer therapies [64]. For example, Mn-based materials not only play an important role in many in vivo processes of neuronal function, immune regulation, antioxidant defenses, and the biosynthesis of some metalloenzymes [65, 66], but also have been widely explored for their potential functions of TME regulation [67-69], including catalyzing the H_2O_2 to produce O_2, depleting GSH, and producing highly cytotoxic ROS of •OH, and their capability of activating immune systems, which have been proved to enhance different kinds of anticancer therapies, such as PDT, RT, sonodynamic therapy, as well as immunotherapy [70-75]. What's more, Si-based materials have been also widely studied in anticancer therapy. MSNs not only have shown advantages in chemotherapy owing to their facile synthesis and functionalization, high pore volume and surface area, controllable pore size and morphology, as well as good physicochemical stability and biocompatibility, but also have shown the capacity of immune activation as shown in previous studies [76-83].

1.2 Research objectives

There have been many kinds of research using the strategy of combining immunotherapy with other anticancer therapies or regulating TME to enhance the inhibitory effect on primary tumors and many good outcomes have been achieved. Whereas there is little research about the strategy that combines immunotherapy with other anticancer therapies and regulates TME to synergistically enhance the inhibitory effect on both primary tumors and metastasis.

In this study, Mn-Si-based NPs were synthesized and applied to regulate TME in different combinational anticancer therapies of immunotherapy with other anticancer therapies and inhibit both tumor growth and metastasis, as shown in Figure 1-2. The regulation functions to TME by these nanoparticles were carefully investigated both in solutions and in different cancer cells. The inhibitory effect on tumor growth and tumor metastasis was evaluated using a bilateral animal model.

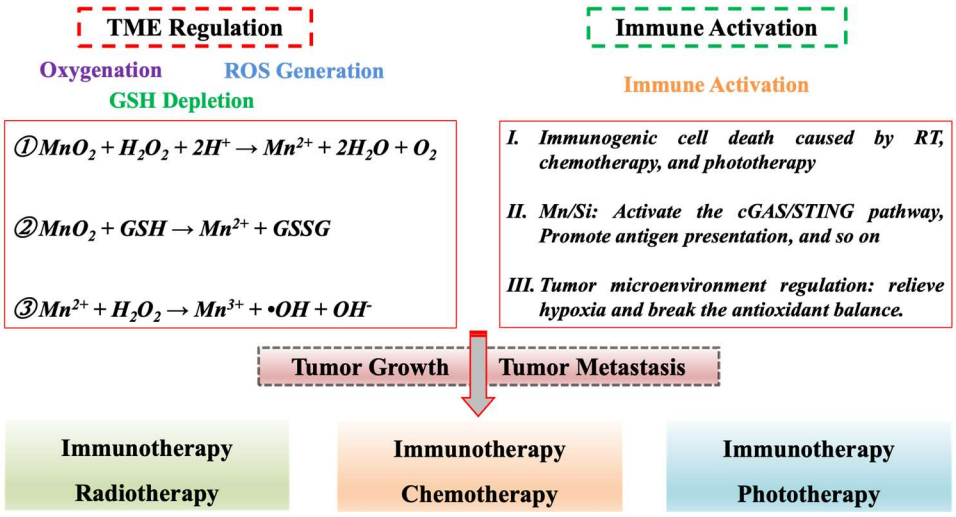

Figure 1-2 Mn-Si-based NPs enhance combinational anticancer therapy through TME regulation and immune activation

In chapter 2, Mn-covered-SiO_2 composite nanoparticles (SM NPs) were synthesized and applied to the combinational anticancer therapies of immunotherapy with RT. The functions of oxygenation, ROS generation, GSH depletion, and immune activation induced by SM NPs were carefully investigated. Moreover, the intracellular change after exposure to X-ray radiation, such as ROS levels, DNA damage, GPX-4, and LPO levels, was also analyzed. Finally, SM NPs were further analyzed in vivo to investigate the inhibitory effect on both primary tumors and distant untreated tumors with or without the presence of the anti-CTLA-4 antibody utilizing a bilateral animal model. And the mechanisms of in vivo immune activation were also analyzed.

In chapter 3, Mn-doped MSNs (MM NPs) were synthesized and applied to the combinational anticancer therapies of immunotherapy with chemotherapy. The influences of Mn-doping and Mn concentration doped into MSNs on the regulation functions to TME were carefully analyzed through investigating the capacities of GSH depletion, ROS generation, oxygenation, cell-killing effect, immune activation, and degradation promotion. Moreover, the in vivo anticancer effects of the combination of DOX, MM, and the anti-CTLA-4 on inhibiting primary tumors and metastatic tumors were further analyzed utilizing a bilateral animal model, including the monitoring of tumor size and measurement of cytokine secretion from splenocytes.

In chapter 4, MM NPs, loaded with the photo agent of IR 780 and further covered by Mn were synthesized (IMM) and applied to the combinational anticancer therapy of immunotherapy with phototherapy. The photothermal effect and photodynamic effect

induced by IMM were carefully investigated using different power densities, IR 780 concentrations, and irradiation time periods. Additionally, IMM protected IR 780 from degradation and induced better photostability indicated by the stable photothermal and photodynamic capability induced by IMM stored in darkness for 2 weeks. The regulation functions to TME were also investigated, including GSH depletion, ROS generation, and oxygenation. And the oxygenation improved the photodynamic capability. Moreover, the in vivo anticancer effects of the combination of an 808nm laser irradiation and IMM on the inhibitory of primary tumors and metastatic tumors after laser irradiation were evaluated utilizing a bilateral animal model.

Reference

1. Sung H, Ferlay J, Siegel RL, Laversanne M, Soerjomataram I, Jemal A, Bray F: **Global cancer statistics 2020: GLOBOCAN estimates of incidence and mortality worldwide for 36 cancers in 185 countries**. *CA: a cancer journal for clinicians* 2021, **71**(3):209-249.

2. Swartz MA, Iida N, Roberts EW, Sangaletti S, Wong MH, Yull FE, Coussens LM, DeClerck YA: **Tumor Microenvironment Complexity: Emerging Roles in Cancer TherapyTumor Microenvironment**. *Cancer research* 2012, **72**(10):2473-2480.

3. Sies H: **Hydrogen peroxide as a central redox signaling molecule in physiological oxidative stress: Oxidative eustress**. *Redox biology* 2017, **11**:613-619.

4. Martin JD, Fukumura D, Duda DG, Boucher Y, Jain RK: **Reengineering the tumor microenvironment to alleviate hypoxia and overcome cancer heterogeneity**. *Cold Spring Harbor perspectives in medicine* 2016, **6**(12):a027094.

5. Harrison L, Blackwell K: **Hypoxia and anemia: factors in decreased sensitivity to radiation therapy and chemotherapy?** *The oncologist* 2004, **9**(S5):31-40.

6. Shannon AM, Bouchier-Hayes DJ, Condron CM, Toomey D: **Tumour hypoxia, chemotherapeutic resistance and hypoxia-related therapies**. *Cancer*

treatment reviews 2003, **29**(4):297-307.

7. Lambert AW, Pattabiraman DR, Weinberg RA: **Emerging biological principles of metastasis**. *Cell* 2017, **168**(4):670-691.

8. Time CS: **SEER cancer statistics review 1975-2008**. 2011.

9. Zhang P, Zhai Y, Cai Y, Zhao Y, Li Y: **Nanomedicine-based immunotherapy for the treatment of cancer metastasis**. *Advanced Materials* 2019, **31**(49):1904156.

10. Schroeder A, Heller DA, Winslow MM, Dahlman JE, Pratt GW, Langer R, Jacks T, Anderson DG: **Treating metastatic cancer with nanotechnology**. *Nature Reviews Cancer* 2012, **12**(1):39-50.

11. Zitvogel L, Galluzzi L, Smyth MJ, Kroemer G: **Mechanism of action of conventional and targeted anticancer therapies: reinstating immunosurveillance**. *Immunity* 2013, **39**(1):74-88.

12. Couzin-Frankel J: **Cancer immunotherapy**. In.: American Association for the Advancement of Science; 2013.

13. Sharma P, Hu-Lieskovan S, Wargo JA, Ribas A: **Primary, adaptive, and acquired resistance to cancer immunotherapy**. *Cell* 2017, **168**(4):707-723.

14. Waldman AD, Fritz JM, Lenardo MJ: **A guide to cancer immunotherapy: from T cell basic science to clinical practice**. *Nature Reviews Immunology* 2020, **20**(11):651-668.

15. Meric-Bernstam F, Larkin J, Tabernero J, Bonini C: **Enhancing anti-tumour**

efficacy with immunotherapy combinations. *The Lancet* 2021, **397**(10278):1010-1022.

16. Hodi FS, O'day SJ, McDermott DF, Weber RW, Sosman JA, Haanen JB, Gonzalez R, Robert C, Schadendorf D, Hassel JC: **Improved survival with ipilimumab in patients with metastatic melanoma**. *New England Journal of Medicine* 2010, **363**(8):711-723.

17. Cogdill AP, Andrews MC, Wargo JA: **Hallmarks of response to immune checkpoint blockade**. *British journal of cancer* 2017, **117**(1):1-7.

18. Song C, Phuengkham H, Kim YS, Dinh VV, Lee I, Shin IW, Shin HS, Jin SM, Um SH, Lee H: **Syringeable immunotherapeutic nanogel reshapes tumor microenvironment and prevents tumor metastasis and recurrence**. *Nature communications* 2019, **10**(1):1-15.

19. Lequeux A, Noman MZ, Xiao M, Sauvage D, Van Moer K, Viry E, Bocci I, Hasmim M, Bosseler M, Berchem G: **Impact of hypoxic tumor microenvironment and tumor cell plasticity on the expression of immune checkpoints**. *Cancer Letters* 2019, **458**:13-20.

20. Daniel S, Sullivan K, Labadie K, Pillarisetty V: **Hypoxia as a barrier to immunotherapy in pancreatic adenocarcinoma**. *Clinical and translational medicine* 2019, **8**(1):1-17.

21. Chouaib S, Messai Y, Couve S, Escudier B, Hasmim M, Noman MZ: **Hypoxia promotes tumor growth in linking angiogenesis to immune escape**.

Frontiers in immunology 2012, **3**:21.

22. Chouaib S, Janji B, Tittarelli A, Eggermont A, Thiery JP: **Tumor plasticity interferes with anti-tumor immunity**. *Critical Reviews™ in Immunology* 2014, **34**(2).

23. Hasmim M, Messai Y, Ziani L, Thiery J, Bouhris J-H, Noman MZ, Chouaib S: **Critical role of tumor microenvironment in shaping NK cell functions: implication of hypoxic stress**. *Frontiers in immunology* 2015, **6**:482.

24. TERRY CK, JANJI B, CHOUAIB S: **HYPOXIA: A KEY PLAYER IN ANTI-TUMOR IMMUNE RESPONSE**. 2015.

25. Peitzsch C, Perrin R, Hill RP, Dubrovska A, Kurth I: **Hypoxia as a biomarker for radioresistant cancer stem cells**. *International journal of radiation biology* 2014, **90**(8):636-652.

26. Kitamura T, Qian B-Z, Pollard JW: **Immune cell promotion of metastasis**. *Nature Reviews Immunology* 2015, **15**(2):73-86.

27. Peng G, Liu Y: **Hypoxia-inducible factors in cancer stem cells and inflammation**. *Trends in pharmacological sciences* 2015, **36**(6):374-383.

28. Lardner A: **The effects of extracellular pH on immune function**. *Journal of leukocyte biology* 2001, **69**(4):522-530.

29. Kennedy L, Sandhu JK, Harper M-E, Cuperlovic-Culf M: **Role of glutathione in cancer: From mechanisms to therapies**. *Biomolecules* 2020, **10**(10):1429.

30. Chen Y-J, Lu C-T, Lee T-Y, Chen Y-J: **dbGSH: a database of S-**

glutathionylation. *Bioinformatics* 2014, **30**(16):2386-2388.

31. Lermant A, Murdoch CE: **Cysteine glutathionylation acts as a redox switch in endothelial cells**. *Antioxidants* 2019, **8**(8):315.

32. Green DR, Ferguson T, Zitvogel L, Kroemer G: **Immunogenic and tolerogenic cell death**. *Nature Reviews Immunology* 2009, **9**(5):353-363.

33. Xiong Y, Xiao C, Li Z, Yang X: **Engineering nanomedicine for glutathione depletion-augmented cancer therapy**. *Chemical Society Reviews* 2021, **50**(10):6013-6041.

34. Kemp JA, Kwon YJ: **Cancer nanotechnology: current status and perspectives**. *Nano convergence* 2021, **8**(1):1-38.

35. Yu W-D, Sun G, Li J, Xu J, Wang X: **Mechanisms and therapeutic potentials of cancer immunotherapy in combination with radiotherapy and/or chemotherapy**. *Cancer letters* 2019, **452**:66-70.

36. Apetoh L, Ghiringhelli F, Tesniere A, Obeid M, Ortiz C, Criollo A, Mignot G, Maiuri MC, Ullrich E, Saulnier P: **Toll-like receptor 4–dependent contribution of the immune system to anticancer chemotherapy and radiotherapy**. *Nature medicine* 2007, **13**(9):1050-1059.

37. Fucikova J, Kralikova P, Fialova A, Brtnicky T, Rob L, Bartunkova J, Špíšek R: **Human tumor cells killed by anthracyclines induce a tumor-specific immune response**. *Cancer research* 2011, **71**(14):4821-4833.

38. Sancho D, Joffre OP, Keller AM, Rogers NC, Martinez D, Hernanz-Falcón P,

Rosewell I: **Identification of a dendritic cell receptor that couples sensing of necrosis to immunity**. *Nature* 2009, **458**(7240):899-903.

39. Ma Y, Adjemian S, Mattarollo SR, Yamazaki T, Aymeric L, Yang H, Catani JPP, Hannani D, Duret H, Steegh K: **Anticancer chemotherapy-induced intratumoral recruitment and differentiation of antigen-presenting cells**. *Immunity* 2013, **38**(4):729-741.

40. Danesi R, Fogli S, Gennari A, Conte P, Del Tacca M: **Pharmacokinetic-pharmacodynamic relationships of the anthracycline anticancer drugs**. *Clinical pharmacokinetics* 2002, **41**(6):431-444.

41. Pol J, Vacchelli E, Aranda F, Castoldi F, Eggermont A, Cremer I, Sautes-Fridman C, Fucikova J, Galon J, Spisek R: **Trial Watch: Immunogenic cell death inducers for anticancer chemotherapy**. *Oncoimmunology* 2015, **4**(4):e1008866.

42. Martin OA, Anderson RL, Narayan K, MacManus MP: **Does the mobilization of circulating tumour cells during cancer therapy cause metastasis?** *Nature reviews Clinical oncology* 2017, **14**(1):32-44.

43. Ibragimova MK, Tsyganov MM, Litviakov N: **Natural and chemotherapy-induced clonal evolution of tumors**. *Biochemistry (Moscow)* 2017, **82**(4):413-425.

44. Daenen LG, Roodhart JM, van Amersfoort M, Dehnad M, Roessingh W, Ulfman LH, Derksen PW, Voest EE: **Chemotherapy Enhances Metastasis**

Formation via VEGFR-1–Expressing Endothelial CellsChemotherapy-Induced Metastases. *Cancer research* 2011, **71**(22):6976-6985.

45. Wu YJ, Muldoon LL, Dickey DT, Lewin SJ, Varallyay CG, Neuwelt EA: **Cyclophosphamide enhances human tumor growth in nude rat xenografted tumor models**. *Neoplasia* 2009, **11**(2):187-195.

46. Pujol J-L, Vansteenkiste JF, De Pas TM, Atanackovic D, Reck M, Thomeer M, Douillard J-Y, Fasola G, Potter V, Taylor P: **Safety and immunogenicity of MAGE-A3 cancer immunotherapeutic with or without adjuvant chemotherapy in patients with resected stage IB to III MAGE-A3-positive non-small-cell lung cancer**. *Journal of Thoracic Oncology* 2015, **10**(10):1458-1467.

47. Formenti SC, Demaria S: **Systemic effects of local radiotherapy**. *The lancet oncology* 2009, **10**(7):718-726.

48. Lugade AA, Moran JP, Gerber SA, Rose RC, Frelinger JG, Lord EM: **Local radiation therapy of B16 melanoma tumors increases the generation of tumor antigen-specific effector cells that traffic to the tumor**. *The Journal of Immunology* 2005, **174**(12):7516-7523.

49. Matsumura S, Wang B, Kawashima N, Braunstein S, Badura M, Cameron TO, Babb JS, Schneider RJ, Formenti SC, Dustin ML: **Radiation-induced CXCL16 release by breast cancer cells attracts effector T cells**. *The Journal of Immunology* 2008, **181**(5):3099-3107.

50. Reits EA, Hodge JW, Herberts CA, Groothuis TA, Chakraborty M, K. Wansley E, Camphausen K, Luiten RM, de Ru AH, Neijssen J: **Radiation modulates the peptide repertoire, enhances MHC class I expression, and induces successful antitumor immunotherapy**. *The Journal of experimental medicine* 2006, **203**(5):1259-1271.

51. Castleman B: **Case records of the Massachusetts General Hospital-case 46262**. *N Engl J Med* 1960, **262**:1334-1338.

52. Okuma K, Yamashita H, Niibe Y, Hayakawa K, Nakagawa K: **Abscopal effect of radiation on lung metastases of hepatocellular carcinoma: a case report**. *Journal of medical case reports* 2011, **5**(1):1-4.

53. Golden EB, Demaria S, Schiff PB, Chachoua A, Formenti SC: **An abscopal response to radiation and ipilimumab in a patient with metastatic non–small cell lung cancer**. *Cancer immunology research* 2013, **1**(6):365-372.

54. Fairlamb D: **Spontaneous regression of metastases of renal cancer: a report of two cases including the first recorded regression following irradiation of a dominant metastasis and review of the world literature**. *Cancer* 1981, **47**(8):2102-2106.

55. Ngwa W, Irabor OC, Schoenfeld JD, Hesser J, Demaria S, Formenti SC: **Using immunotherapy to boost the abscopal effect**. *Nature Reviews Cancer* 2018, **18**(5):313-322.

56. McGinnes K, Florence J, Penny R: **The effect of radiotherapy on the natural**

killer (NK)-cell activity of cancer patients. *Journal of clinical immunology* 1987, **7**(3):210-217.

57. Bos PD, Plitas G, Rudra D, Lee SY, Rudensky AY: **Transient regulatory T cell ablation deters oncogene-driven breast cancer and enhances radiotherapy**. *Journal of Experimental Medicine* 2013, **210**(11):2435-2466.

58. Dewan MZ, Galloway AE, Kawashima N, Dewyngaert JK, Babb JS, Formenti SC, Demaria S: **Fractionated but Not Single-Dose Radiotherapy Induces an Immune-Mediated Abscopal Effect when Combined with Anti–CTLA-4 AntibodyFractionated Radiation Synergizes with Immunotherapy**. *Clinical Cancer Research* 2009, **15**(17):5379-5388.

59. Dovedi SJ, Cheadle EJ, Popple AL, Poon E, Morrow M, Stewart R, Yusko EC, Sanders CM, Vignali M, Emerson RO: **Fractionated Radiation Therapy Stimulates Antitumor Immunity Mediated by Both Resident and Infiltrating Polyclonal T-cell Populations when Combined with PD-1 BlockadeFractionated RT Modulates the Local TCR Repertoire**. *Clinical Cancer Research* 2017, **23**(18):5514-5526.

60. Yagawa Y, Tanigawa K, Kobayashi Y, Yamamoto M: **Cancer immunity and therapy using hyperthermia with immunotherapy, radiotherapy, chemotherapy, and surgery**. *Journal of Cancer Metastasis and Treatment* 2017, **3**:218-230.

61. Xie Z, Fan T, An J, Choi W, Duo Y, Ge Y, Zhang B, Nie G, Xie N, Zheng T:

Emerging combination strategies with phototherapy in cancer nanomedicine. *Chemical Society Reviews* 2020, **49**(22):8065-8087.

62. Wang C, Xu L, Liang C, Xiang J, Peng R, Liu Z: **Immunological responses triggered by photothermal therapy with carbon nanotubes in combination with anti-CTLA-4 therapy to inhibit cancer metastasis**. *Advanced materials* 2014, **26**(48):8154-8162.

63. Chen Q, Xu L, Liang C, Wang C, Peng R, Liu Z: **Photothermal therapy with immune-adjuvant nanoparticles together with checkpoint blockade for effective cancer immunotherapy**. *Nature communications* 2016, **7**(1):1-13.

64. Ji T, Zhao Y, Ding Y, Nie G: **Using functional nanomaterials to target and regulate the tumor microenvironment: diagnostic and therapeutic applications**. *Advanced Materials* 2013, **25**(26):3508-3525.

65. Horning KJ, Caito SW, Tipps KG, Bowman AB, Aschner M: **Manganese is essential for neuronal health**. *Annual review of nutrition* 2015, **35**:71.

66. Waldron KJ, Rutherford JC, Ford D, Robinson NJ: **Metalloproteins and metal sensing**. *Nature* 2009, **460**(7257):823-830.

67. Guo Sy, Sun D, Ni Dl, Yu Mr, Qian K, Zhang W, Yang Yw, Song S, Li Y, Xi Zy: **Smart tumor microenvironment-responsive Nanotheranostic agent for effective cancer therapy**. *Advanced Functional Materials* 2020, **30**(17):2000486.

68. Miao Y, Qiu Y, Zhang M, Yan K, Zhang P, Lu S, Liu Z, Shi X, Zhao X: **Aqueous**

self-assembly of block copolymers to form manganese oxide-based polymeric vesicles for tumor microenvironment-activated drug delivery. *Nano-micro letters* 2020, **12**(1):1-15.

69. Zhang C, Ni D, Liu Y, Yao H, Bu W, Shi J: **Magnesium silicide nanoparticles as a deoxygenation agent for cancer starvation therapy**. *Nature Nanotechnology* 2017, **12**(4):378-386.

70. Lin LS, Song J, Song L, Ke K, Liu Y, Zhou Z, Shen Z, Li J, Yang Z, Tang W: **Simultaneous Fenton-like ion delivery and glutathione depletion by MnO2-based nanoagent to enhance chemodynamic therapy**. *Angewandte Chemie* 2018, **130**(18):4996-5000.

71. Yao Y, Li N, Zhang X, Ong'achwa Machuki J, Yang D, Yu Y, Li J, Tang D, Tian J, Gao F: **DNA-templated silver nanocluster/porphyrin/MnO2 platform for label-free intracellular Zn2+ imaging and fluorescence-/magnetic resonance imaging-guided photodynamic therapy**. *ACS applied materials & interfaces* 2019, **11**(15):13991-14003.

72. Yi X, Chen L, Zhong X, Gao R, Qian Y, Wu F, Song G, Chai Z, Liu Z, Yang K: **Core–shell Au@ MnO2 nanoparticles for enhanced radiotherapy via improving the tumor oxygenation**. *Nano Research* 2016, **9**(11):3267-3278.

73. Sun P, Deng Q, Kang L, Sun Y, Ren J, Qu X: **A smart nanoparticle-laden and remote-controlled self-destructive macrophage for enhanced chemo/chemodynamic synergistic therapy**. *ACS nano* 2020, **14**(10):13894-

13904.

74. Gao F, Tang Y, Liu WL, Zou MZ, Huang C, Liu CJ, Zhang XZ: **Intra/extracellular lactic acid exhaustion for synergistic metabolic therapy and immunotherapy of tumors**. *Advanced materials* 2019, **31**(51):1904639.

75. Lv M, Chen M, Zhang R, Zhang W, Wang C, Zhang Y, Wei X, Guan Y, Liu J, Feng K: **Manganese is critical for antitumor immune responses via cGAS-STING and improves the efficacy of clinical immunotherapy**. *Cell research* 2020, **30**(11):966-979.

76. Zhou S, Zhong Q, Wang Y, Hu P, Zhong W, Huang C-B, Yu Z-Q, Ding C-D, Liu H, Fu J: **Chemically engineered mesoporous silica nanoparticles-based intelligent delivery systems for theranostic applications in multiple cancerous/non-cancerous diseases**. *Coordination Chemistry Reviews* 2022, **452**:214309.

77. Li X, Wang X, Qian G, Ito A: **Synergistical chemotherapy and cancer immunotherapy using dual drug-delivering and immunopotentiating mesoporous silica**. *Applied Materials Today* 2019, **16**:102-111.

78. Wang X, Li X, Ito A, Sogo Y, Ohno T: **Particle-size-dependent toxicity and immunogenic activity of mesoporous silica-based adjuvants for tumor immunotherapy**. *Acta biomaterialia* 2013, **9**(7):7480-7489.

79. Wang X, Li X, Ito A, Sogo Y, Ohno T: **Pore size-dependent immunogenic activity of mesoporous silica-based adjuvants in cancer immunotherapy**.

Journal of Biomedical Materials Research Part A: An Official Journal of The Society for Biomaterials, The Japanese Society for Biomaterials, and The Australian Society for Biomaterials and the Korean Society for Biomaterials 2014, **102**(4):967-974.

80. Wang X, Li X, Ito A, Sogo Y, Watanabe Y, Tsuji NM, Ohno T: **Biodegradable metal ion-doped mesoporous silica nanospheres stimulate anticancer Th1 immune response in vivo**. *ACS applied materials & interfaces* 2017, **9**(50):43538-43544.

81. Wang X, Li X, Ito A, Watanabe Y, Sogo Y, Tsuji NM, Ohno T: **Stimulation of in vivo antitumor immunity with hollow mesoporous silica nanospheres**. *Angewandte Chemie* 2016, **128**(5):1931-1935.

82. Wang X, Li X, Ito A, Yoshiyuki K, Sogo Y, Watanabe Y, Yamazaki A, Ohno T, Tsuji NM: **Hollow structure improved anti-cancer immunity of mesoporous silica nanospheres in vivo**. *Small* 2016, **12**(26):3510-3515.

83. Wang X, Ihara S, Li X, Ito A, Sogo Y, Watanabe Y, Tsuji NM, Yamazaki A: **Si-doping increases the adjuvant activity of hydroxyapatite nanorods**. *Colloids and Surfaces B: Biointerfaces* 2019, **174**:300-307.

Chapter 2 Radio-immunotherapy enhanced by SM NPs

2.1 Introduction

RT is one of the vital cancer treatment strategies in clinical practice, and one of the major radio-toxic effects of RT is DNA damage [1, 2]. In recent years, the abscopal effect of RT has been proven to stimulate immune responses, but it is seen in only 10% of cases in clinical practice [3]. Therefore, the inhibitory effect of RT on tumor metastasis is still far from satisfactory [4, 5]. Immunotherapy has emerged in recent years with promising clinical applications owing to its modulation functions for immune responses [6]. Interestingly, compared with RT alone, the abscopal effect of RT can become more common when combined with immunotherapy both in preclinical and clinical models of PD-1 and CTLA-4 inhibitors [7, 8]. However, owing to the host mechanism to remain immunologically silent after cell death caused by DNA damage, the DNA damage generated will be inactivated through many mechanisms, including cancer cell autophagy [9], apoptotic caspase activation during apoptosis [10], and digestion by host deoxyribonuclease (DNase) [10, 11]. Moreover, the efficacy of RT and immunotherapy is limited by the complex TME, which is usually characterized by hypoxia, acidic pH value [12], elevated H_2O_2 levels [13], and powerful antioxidative systems [14]. Hypoxia of TME contributes to tumor recurrence and poor prognosis in RT [15] and limits the efficacy of RT through the support of the development of cancer stem cells and inhibition of the radical generation [16, 17]. Specifically, hypoxic cells

require a threefold higher dose of radiation than normoxic cells [18]. Moreover, a hypoxic TME can suppress anticancer immune responses through the promotion of the infiltration and accumulation of suppressor T-cells and the inhibition of the adaptive immune system, resulting in tumor angiogenesis and cancer metastasis [19, 20]. Moreover, GSH, one of the main reducing agents of antioxidative systems in cancer cells, can scavenge ROS, which decreases the efficacy of ROS-based therapies and promotes the expression of glutathione peroxidase 4 (GPX-4), which further enhances the antioxidation barrier in TME, thus strongly suppressing the efficacy of RT [14]. These findings emphasize the fact that regulating TME can be a promising strategy to enhance the synergistic efficacy of radio-immunotherapy. In recent years, TME-responsive anticancer therapies have been widely studied, which modulate TME through the unique physical and chemical properties of nanomaterials [21, 22]. They have been proved effective in improving treatment outcomes of various anticancer therapies [23, 24]. For example, H_2O_2, an ideal prodrug for Fenton reactions or Fenton-like reactions in CDT, can react with various nanomaterials to produce highly toxic •OH, such as Mn^{2+} [25-27]. Whereas, Recently, Mn-based nanomaterials have attracted tremendous interest in the field of anticancer therapies. Mn plays an important role in many in vivo processes, such as neuronal function, immune regulation, antioxidant defenses, and the biosynthesis of some metalloenzymes [28, 29]. Studies have shown that Mn^{2+} can be excreted rapidly by the kidneys leading to fewer side effects on the body [30]. Moreover, its unique properties in regulating TME make Mn-based

nanomaterials potentially applicable to anticancer therapies. Typically, Mn-based nanomaterials can induce an increase in O_2 and ROS levels through reactions with H_2O_2 and GSH in TME, thus enhancing the efficacy of many anticancer therapies [31-33]. Notably, Mn^{2+} has been proved by recent studies to have immune stimulation potential [34-38]. It has been proved that Mn^{2+} is critical in the innate immune sensing of tumors and enhancing adaptive immune responses, which can promote the sensitivity of the DNA sensor of the cyclic GMP - AMP synthase (cGAS) and the stimulator of interferon genes (STING) [34, 35]. Interestingly, RT-induced DNA damage has also been proved to activate the cGAS/STING pathway and enhance immune responses [39, 40]. Therefore, Mn-based nanomaterials may be promising in enhancing the immune responses and the abscopal effect of RT. Except for Mn-based nanomaterials, various inorganic nanomaterials have been proved to stimulate immune responses [41], especially silica. In the previous studies, silica-based nanomaterials have shown significant immunogenicity, which can promote antigen presentation, cytokine secretion, CD 4+ and CD 8+ T cell proliferation, and effector memory T cell population [42-49].

Therefore, it is considered that combining different nanomaterials with immune stimulation capacity may maximize the immune responses in immunotherapy. However, the applications of Mn-Si-based NPs to RT to synergistically inhibit both tumor growth and tumor recurrence and metastasis through the regulation of TME and immune responses are still rare. Whereas tumor recurrence and metastasis are still challenging

for tumor treatment by RT, indicating that simply aiming at enhancing primary tumor treatment is far from satisfaction, and the problems of tumor recurrence and metastasis are urgent to be solved. The Mn-Si-based NPs have been synthesized to regulate the TME to a beneficial status before exposure to radiation in radio-immunotherapy from different aspects: oxygenation, GSH depletion, ROS generation, and immune activation. Notably, due to the ROS-involved redox metabolism equilibrium, only generating ROS may trigger more GSH production and result in more ROS consumption by GSH. Here, Mn-based nanomaterials not only induce ROS generation, but also deplete GSH, which breaks the ROS-involved redox metabolism equilibrium to regulate TME. In conclusion, the Mn-Si-based NPs have not only acted as the radiosensitizer to enhance the treatment of primary tumors by RT at a low dose of radiation, but also played a role in activating immune response to inhibit the tumor recurrence and metastasis.

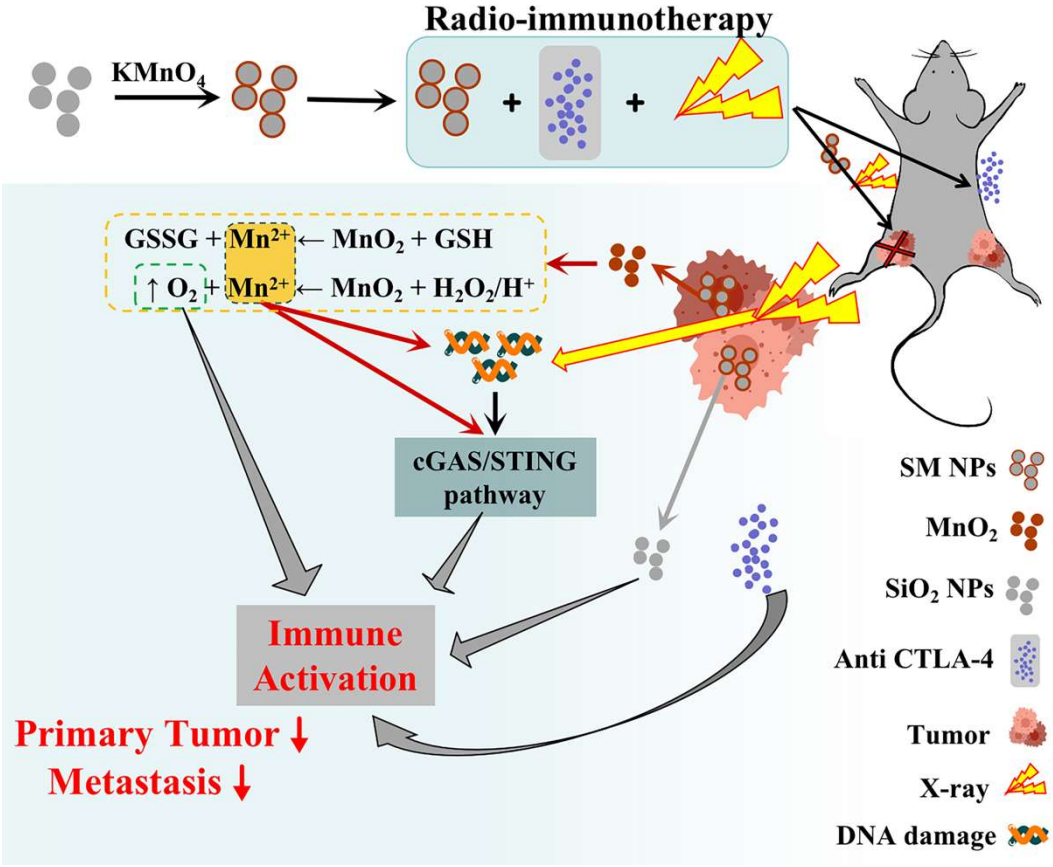

Scheme 2-1 Synergistic efficacy of SM NPs-enhanced radio-immunotherapy through TME regulation and immune activation

2.2 Materials and methods

2.2.1 Materials

Hexadecyltrimethylammonium bromide (CTAB), tetraethyl orthosilicate (TEOS), potassium permanganate ($KMnO_4$), and N - acetyl - l - cysteine (NAC) were from Wako Chemical, Ltd. MB and hydrogen peroxide (H_2O_2, 30%) were from FUJIFILM Wako Pure Chemical Co. 5 mol L^{-1} - sodium hydroxide solution (NaOH) was from Nacalai Tesque, Inc. Glutathione reduced form (GSH) was from Tokyo Chemical Industry Co.,

Ltd. Liperfluo was from Dojindo Molecular Technologies, Inc. The anti-CTLA-4 antibody (9D9; Cat. #BE0164) was from BioXcell.

2.2.2 Synthesis of Mn-coated SiO_2 NPs (SM NPs)

Firstly, SiO_2 NPs were prepared in accordance with a previously published protocol with modification [50]. 1 g of CTAB was dissolved in 480 mL of ultrapure water containing 1.4 mL of NaOH (5 mol). Then, the as-prepared solution was stirred for 1 h in a water bath at 70°C. Finally, 6.7 mL of TEOS was added and stirred for 2 h in the water bath. The precipitates were collected by centrifugation and washed three times in ultrapure water. SiO_2 nanoparticles were obtained by drying at 60°C for 8 h and heating at 600°C for 5 h.

Then, SM NPs were prepared by the hydrothermal method. The as-prepared SiO_2 nanoparticles (200 mg) were mixed with $KMnO_4$ (75 mg) in ultrapure water (60 mL) and maintained at 160°C for 22 h. The precipitates were washed in ultrapure water 10 times to remove any remaining $KMnO_4$. SM NPs were obtained by drying the precipitates at 60°C for 8 h. For intracellular and in vivo experiments, the obtained SM NPs were sterilized by heating at 160°C for 3 h using a drying sterilizer (SG 600, Yamato Scientific, Japan).

2.2.3 Characterization of SM NPs

The morphology and chemical composition of SM NPs were observed by field emission scanning electron microscopy (FE-SEM, HITACHI, Japan) and field

emission transmission electron microscopy with energy dispersive X-ray spectroscopy (TEM – EDS, JEOL 2100F, Japan). The phase of SM NPs was characterized by X-ray powder diffraction (XRD, RINT 2550, RIGAKU, Japan) analysis. The valence state of constituent elements of SM NPs was determined by X - ray photoelectron spectroscopy (XPS, PHI 5000 VersaProbe III, ULVAC - PHI, Japan). The Si/Mn ratio in SM NPs was measured by inductive coupled plasma atomic emission spectrometer (ICP – AES, SPS7800, Seiko Instruments, Japan).

2.2.4 Regulation functions to TME

2.2.4.1 Oxygenation

(1) In solutions

The oxygenation induced by SM NPs was firstly investigated in solutions containing H_2O_2 with an O_2 probe of ruthenium-tris (4,7-diphenyl-1,10-phenanthroline) dichloride (RDPP, Santa Cruz Biotechnology, USA) in the presence of H_2O_2. The fluorescence of RDPP can be strongly reduced by molecular oxygen because of the dynamic quenching. Therefore, RDPP has been widely utilized to detect and quantify oxygen level. SM NPs were mixed with RDPP in PBS (-) solution, then H_2O_2 (100 mM) was added. The fluorescence of RDPP (Ex / Em = 450 nm / 630 nm) was measured at determined time points using a microplate reader (MTP-900, Corona Electric, Japan). Data were normalized to the control group.

(2) In LLC cells

Then the intracellular oxygenation induced by SM NPs was also investigated with RDPP. First, LLC cells (4×10^5 cells mL^{-1}, Riken Bio Resource Center, Japan) were seeded in 96-well plates and cultured overnight at 37°C in a 5 % CO_2 humidified atmosphere. Next, RDPP (3 μmol) was added after washing the cells with PBS (-) once. After incubation with RDPP for 4h, SM NPs (30 μg mL^{-1}) were added and the fluorescence (Ex / Em = 450 nm / 630 nm) of RDPP was measured at determined time points using the microplate reader, and the fluorescence images were obtained by fluorescence microscopy. Data from the microplate reader were normalized to the control group.

2.2.4.2 ROS generation

(1) In solutions

ROS generation induced by SM NPs in solutions containing H_2O_2 was analyzed according to a previously published method.[53] First, chemodynamic activity was analyzed in H_2O. SM NPs (30 μg mL^{-1}) were firstly dispersed in GSH - H_2O solution with different GSH concentrations (0, 1, 5, and 10 mM) and then reacted with H_2O_2 (10 mM) and MB for 30 min. Then, the absorption intensity of MB at 665 nm was measured using an ultraviolet-visible (UV - vis) absorption spectrometer (V - 550, JASCO, Japan).

Then, the ROS generation induced by SM NPs was investigated in $NaHCO_3$ solution. In particular, SM NPs at different concentrations (0, 30, and 90 μg mL^{-1}) were firstly dispersed in $NaHCO_3$ solution (25 mM) containing GSH (5 mM) and then maintained

at 37ºC for 10 min. Then, MB (10 μg mL^{-1}) and H_2O_2 (10 mM) were added to the as-prepared solution and maintained at 37ºC for another 30 min. Finally, the absorption intensity of MB at 630 nm was measured using the microplate reader.

(2) In LLC cells

The ROS generation capacity of SM NPs was analyzed using a DCFDA / H2DCFDA -cellular ROS assay kit (Abcam, USA). DCFDA/H2DCFDA can be deacetylated by cellular esterases after diffusion into cells and converted to a non-fluorescent compound, which can be oxidized by ROS and converted to DCF, a highly fluorescent compound, which can be detected by fluorescence spectroscopy. In particular, LLC cells (2.5×10^5 cells mL^{-1}) were seeded in 96-well plates and cultured for 24 h followed by incubation for another 6 h with SM NPs of different concentrations (10, 30, and 50 μg mL^{-1}) after washing with PBS (-). Then, the cells were washed with PBS (-) and incubated with DCFDA (30 μmol) for 45 min. After that, the fluorescence (Ex / Em = 492 nm / 530 nm) of DCF was measured using the microplate reader, and the fluorescence images were obtained by fluorescence microscopy.

2.2.4.3 GSH depletion

(1) In solutions

To explore the ROS scavenging effect of GSH, SM NPs (90 μg mL^{-1}) were firstly mixed with GSH of different concentrations (0, 1, 5, and 10 mM) in 25 mM $NaHCO_3$ solution and maintained at 37 ºC for 10 min. Then, MB (10 μg mL^{-1}) and H_2O_2 (10 mM) were added to the as-prepared solution and maintained at 37ºC for another 30 min.

Finally, the absorption intensity of MB at 630 nm was measured using the microplate reader.

Additionally, to simulate the slightly acidic TME, 20 mM GSH solution and 50 mM $NaHCO_3$ solutions were mixed with the volume ratio of 1:1 to prepare the slightly acidic solution (pH 6.92) containing 10 mM GSH and 25 mM $NaHCO_3$. SM NPs of different concentrations were added to the slightly acidic solution and maintained at 37 ^oC for 10 min. Then, MB (10 μg mL^{-1}) and H_2O_2 (10 mM) were added to the as-prepared solution and maintained at 37 ^oC for another 30 min. Finally, the mixed solution was diluted to 2 mL and the solution absorbance of MB was measured using an ultraviolet-visible (UV - vis) absorption spectrometer (V – 730, JASCO, Japan).

We further analyzed the oxygenation induced by SM NPs in the presence of GSH (10 mM) using the O_2 probe of RDPP. SM NPs (100 μg mL^{-1}) were added to the mixed solution containing GSH (10 mM), H_2O_2 (100 mM), and RDPP (3 μM). Then the fluorescence of RDPP (Ex / Em = 450 nm / 630 nm) was measured at determined time points using a microplate reader. Data were normalized to the control group.

We further analyzed the release of Mn induced by GSH through ICP-AES analysis. SM NPs (10 mg mL^{-1}) were dispersed in an acetic acid buffer solution containing GSH (10 mM) at 37 ^oC. At determined time points, the acetic acid buffer solution containing SM NPs and GSH was centrifuged at 10000 rpm for 10 min. The obtained supernatant was collected, and 1 mL of acetic acid buffer solution was added. The release of Mn

from SM NPs was measured by the ICP-AES analysis and the images of SM NPs at 1d, 3d, and 5d were observed by TEM.

(2) In LLC cells

To confirm the intracellular GSH depletion by SM NPs, the GSH content in LLC cells cocultured with SM NPs was measured using a GSSG / GSH quantification kit (Dojindo Molecular Technologies, Japan). First, LLC cells (5×10^5 cells $well^{-1}$) were precultured in a 6-well plate overnight before incubation with SM NPs (30 μg mL^{-1}) for another 6 h. Then the intracellular GSH content was measured in accordance with the manufacturer's instructions.

2.2.4.4 Immune activation

To evaluate the immunogenic activity of SM NPs, the amounts of cytokines (IL-1β and TNF-α) secreted by macrophage-like cells cultured with SM NPs were measured. First, macrophage-like cells were obtained by culturing human monocytic leukemia cells (THP-1, Riken BioResource Research Center, Japan) in a conditioned medium containing 90 vol.% RPMI 1640 (Invitrogen, USA), 10 vol.% FBS, and 0.5 μmol phorbol 12 - myristate 13 - acetate (PMA, Sigma, USA) for 3 h. Next, the as-obtained macrophage-like cells were seeded in 96 - well plates (2×10^6 cells mL^{-1}) and cultured overnight. Then, the cells were incubated with SM NPs (30 μg mL^{-1}) for 1 day. Finally, the amounts of IL-1β and TNF-α secreted were measured using human IL-1β and TNF-α kits (BD Bioscience, USA) in accordance with the manufacturer's instructions.

To evaluate the antigen presentation in vitro, THP-1 cells were firstly differentiated to macrophage-like cells with the same method as described in 2.13. The obtained macrophage-like cells were precultured in a 48-wells plate for 24h. SM NPs were mixed with ovalbumin (OVA) solution at 4°C for 24h with a concentration of 25 μg mL^{-1} for SM NPs and 5 μg mL^{-1} for OVA before coculturing with macrophage-like cells. After coculturing overnight, macrophage-like cells were stained with anti-mouse OVA257-264 (SIINFEKL) peptide bound to H-2Kb Ab (BioLegend) and analyzed by flow cytometry.

2.2.5 In vitro radiosensitization effect of SM NPs

2.2.5.1 Cellular uptake of SM NPs-RhB

The SM NPs uptake by LLC cells was analyzed by confocal laser scanning microscopy (CLSM, Leica Confocal IP / FCS, German). SM-RhB were firstly prepared. SM NPs, rhodamine B, and 3-triethoxysilylpropylamine (APTES, Aldrich, USA) were mixed in anhydrous ethanol and stirred at room temperature for 48 h. Then, the mixed solution was centrifuged, and the obtained precipitants were washed in ethanol. After drying the precipitants at room temperature for 5 d, SM - RhB were obtained. LLC cells (2×10^5 cells mL^{-1}) were cocultured with the obtained SM - RhB in a glass - bottom plate overnight. Then the cells were incubated with LysoTracker Green (50 nmol) at 37°C for 2 h. After washing the cells with a medium containing 90 vol.% low-glucose Dulbecco's modified Eagle's medium (L - DMEM, Wako, Japan) and 10 vol.% fetal

bovine serum (FBS, Invitrogen, USA), the cells were incubated with Hoechst (2.5 μg mL^{-1}) at 37ºC for 6 min. After washing the cells with PBS (-), an anti - fade reagent was added, and the cells were incubated for 15 min on ice followed by fluorescence observation by CLSM.

2.2.5.2 Cytotoxicity after exposure to radiation

LLC cells (5×10^4 cells mL^{-1}) were preseeded in 96 - well plates. After incubation overnight, the medium was changed with a fresh medium containing SM NPs of different concentrations (0, 10, 20, 30, 40, and 50 μg mL^{-1}). After further incubation for 6 h, the cells were exposed to radiation at a dose of 4 Gy (150 kV, 20 mA) using an X-ray generator (MBR-1520R-4, Hitachi Power Solutions, Ibaraki, Japan). Then, the cells were incubated with a fresh medium for another 1 d or 2 d to take the fluorescence images of LLC cells using a calcein - AM (green fluorescence) / PI (red fluorescence) double staining kit and measure the cell viability by a cell counting kit - 8 (CCK - 8) assay. Data from the CCK-8 assay were normalized to the control group.

2.2.5.3 Intracellular ROS generation after exposure to radiation

In particular, LLC cells (2.5×10^5 cells mL^{-1}) were seeded in 96-well plates and cultured overnight followed by incubation with SM NPs of different concentrations (0, 10, 30, and 50 μg mL^{-1}) for another 6h after washing with PBS (-). Next, the cells were washed with PBS (-) and further incubated with DCFDA (30 μmol) for 45 min. Then, the cells were exposed to radiation at a dose of 4 Gy and the fluorescence (Ex / Em =

492 nm / 530 nm) of DCF was immediately measured using a microplate reader. Data were normalized to the control group.

2.2.5.4 Intracellular GPX-4 and LPO level after exposure to radiation

First, LLC cells (7.5×10^5 cells mL^{-1}) were seeded in 6 - well plates and cultured overnight. Next, the cells were incubated with SM NPs (30 μg mL^{-1}) for 6 h followed by exposure to radiation at a dose of 4 Gy. After incubation overnight, GPx-4 and LPO levels were measured by flow cytometry (BD Accuri C6 Plus, aSan Jose, CA, USA). Data were normalized to the control group.

For GPx-4 level measurement, cells were collected and fixed in 4% paraformaldehyde phosphate buffer solution (PFA, Wako, Japan) for 10 min at room temperature. Cells were washed with permeabilization wash buffer (PWB) twice, incubated with PWB at room temperature for 10 min, and then incubated with an anti-GPx-4 antibody (AB125066) at 4ºC overnight. After washing with PWB, the cells were further incubated with a secondary antibody (AB150077) at room temperature for 30 min. Finally, PWB was added, and the fluorescence of cells was assayed by flow cytometry.

For LPO level measurement, cells were collected, washed with RPMI, and incubated with Liperfluo (Dojindo, Japan) at room temperature for 30 min. Finally, the fluorescence of cells was assayed by flow cytometry.

2.2.5.5 Intracellular DNA damage level after exposure to radiation

To confirm DNA damage level, the fluorescence of γ - H2AX, a marker used for DNA damage, was detected using DNA damage detection kit - γ - H2AX - Green (Dojindo, Japan). First, 4×10^6 cells were cultured in a 75 cm^2 flask for 24 h. Next, the cells were incubated with SM NPs (30 μg mL^{-1}) for 6 h and then exposed to radiation at a dose of 4 Gy. After incubation for another 2 h, the density of γ - H2AX foci was measured by flow cytometry. In particular, cells treated with SM NPs and radiation were first fixed in 4% PFA for 5 min, washed with PBS (-) three times, and then stored in PBS (-) at 4°C overnight. After centrifugation and washing in PBS (-), the cells were lysed with 0.05% TritonX-100 for 5 min on ice followed by washing in PBS (-) twice. Then the cells were exposed to blocking buffer for 1h at room temperature, washed in PBS (-), and incubated with an anti-γ-H2AX antibody staining solution at 4°C overnight. After washing with PBS (-) twice, the cells were further incubated with a secondary antibody staining solution for 1 h at room temperature, washed in PBS (-), and dispersed in PBS (-). Finally, the fluorescence of γ-H2AX was measured by flow cytometry. Data were normalized to the control group.

2.2.6 In vivo anticancer effect of SM NPs

The animal experiments were approved by the Ethical Committee of the National Institute of Advanced Industrial Science and Technology (AIST). All of the animal

experiments and feeding were carried out in accordance with the guidelines of the Ethical Committee of AIST, Japan.

2.2.6.1 In vivo anticancer effect of SM NPs - enhanced radio - immunotherapy

Mice (C57BL / 6JJcl, female, 7 weeks old, CLEA, Japan) were randomly divided into three groups (n = 5). On day 0, the mice were subcutaneously injected with live LLC cells into the left hind legs (5×10^5 cells mouse^{-1}) and into the right hind legs (10×10^4 cells mouse^{-1}) to simulate primary tumors and metastatic tumors, respectively. On days 7, 9, and 11, the mice were treated as follows. Mice in group 1 were treated with an intratumor injection of saline (50 μL). Mice in group 2 were treated with radiation on the left hind legs alone at a dose of 6 Gy. Mice in group 3 were treated with an intratumor injection of SM NPs (0.4 mg mouse^{-1}) in saline (50 μL), followed by radiation on the left hind legs at a dose of 6 Gy 3 h later. Before radiation, the mice in all groups were anesthetized using a mixture of three types of anesthetic agents, 0.75 mg kg^{-1} medetomidine (Nippon Zenyaku Kogyo, Fukushima, Japan), 4.0 mg kg^{-1} midazolam (Maruishi Pharmaceutical, Osaka, Japan), and 5.0 mg kg^{-1} butorphanol (Meiji Seika Pharma, Tokyo, Japan). After radiation, the mice were injected with 0.75 mg kg^{-1} atipamezole (Nippon Zenyaku Kogyo, Japan) to reverse the effects of medetomidine. The tumor diameters on both sides of the hind legs were measured using a caliper at determined time points.

On days 23 after LLC cell injection, spleens were collected and digested with a tissue protein extraction reagent (Thermo Scientific, USA) for cytokine analysis. The extract

was centrifuged, and the supernatant was collected. The amount of TNF-α secreted was measured using mouse TNF-α kits (BD Bioscience, USA) in accordance with the manufacturer's instructions.

2.2.6.2 In vivo anticancer effect of SM NPs-enhanced radio-immunotherapy in combination with the anti-CTLA-4 antibody

Mice (C57BL / 6JJcl, female, 6 weeks old, CLEA, Japan) were randomly divided into five groups ($n = 5$). On day 0, the mice were subcutaneously injected with live LLC cells into the left hind leg (5×10^5 cells mouse^{-1}) and into the right hind legs at a concentration of 5×10^4 cells mouse^{-1} to simulate primary tumors and metastatic tumors, respectively. On days 7, 9, and 14, the mice were treated as follows. Mice in group 1 were treated with an intratumor injection of saline (50 μL). Mice in group 2 were treated with radiation on the left hind legs alone at a dose of 4 Gy. Mice in group 3 were treated with an intratumor injection of SM NPs (1 mg mouse^{-1}) in saline (50 μL) followed by radiation on left hind legs at a dose of 4 Gy 3 h later. Mice in group 4 were treated with an intraperitoneal injection of the anti-CTLA-4 antibody (2 mg mL^{-1}) in saline (100 μL), followed by radiation on left hind legs at a dose of 4 Gy 3 h later. Mice in group 5 were treated with an intratumor injection of SM NPs (1 mg mouse^{-1}) in saline (50 μL) and an intraperitoneal injection of the anti-CTLA-4 antibody (2 mg mL^{-1}) in saline (100 μL), followed by radiation on left hind legs at a dose of 4 Gy 3 h later. Before and after radiation, the mice were anesthetized as described in 2.15. The tumor diameters on both sides of legs were measured using a caliper at determined time points.

On days 21 after LLC cell injection, spleens were collected and digested with a tissue protein extraction reagent. The extract was centrifuged, and the supernatant was collected. The amounts of cytokines secreted were measured using mouse IFN-γ, IL-1β, and IL-6 kits (BD Bioscience, USA) in accordance with the manufacturer's instructions.

2.2.6.3 Analysis of activated immune cells in SM NPs-enhanced radio-immunotherapy in combination with the anti-CTLA-4 antibody

Mice (C57BL / 6JJcl, female, 7 weeks old, CLEA, Japan) were randomly divided into five groups ($n = 3$). On day 0, the mice were subcutaneously injected with live LLC cells into the left hind leg (5×10^5 cells mouse^{-1}) and into the right hind legs at a concentration of 5×10^4 cells mouse^{-1} to simulate primary tumors and metastatic tumors, respectively. On days 7 and 9, the mice were treated as follows. Mice in group 1 were treated with radiation on the left hind legs alone at a dose of 4 Gy. Mice in group 2 were treated with an intratumor injection of SM NPs (1 mg mouse^{-1}) in saline (50 μL) followed by radiation on the left hind legs at a dose of 4 Gy 3 h later. Mice in group 3 were treated with an intraperitoneal injection of the anti-CTLA-4 antibody (2 mg mL^{-1}) in saline (100 μL), followed by radiation on the left hind legs at a dose of 4 Gy 3 h later. Mice in group 4 were treated with an intratumor injection of SM NPs (1 mg mouse^{-1}) in saline (50 μL) and an intraperitoneal injection of the anti-CTLA-4 antibody (2 mg mL^{-1}) in saline (100 μL), followed by radiation on the left hind legs at a dose of

4 Gy 3 h later. On days 12, the spleen was collected, stained with anti - mouse CD 4 and anti-mouse CD 8α Abs (Biolegend), and analyzed by flow cytometry.

2.3 Results

2.3.1 Characterization of SM NPs

Uniform SM NPs were obtained by coating Mn onto SiO_2 NPs through the hydrothermal method as shown in the SEM images (Figure 2-1a). And no obvious difference in the shape and size between SiO_2 NPs and SM NPs was observed. As shown in the TEM images (Figure 2-1b), the surface mesoporous structure of SiO_2 NPs almost disappeared after Mn coating, which indicated the successful coating of Mn. Moreover, as shown in Figure 2-2, the elemental distribution confirmed the presence of Mn on the surface of SM NPs.

Besides, the phase and valence state of coated Mn were analyzed through XRD and XPS analysis, respectively. As shown in the XRD results of Figure 2-3a, there were three new diffraction peaks for SM NPs, compared with SiO_2 NPs, which were attributed to the (001), (111), and (020) planes of birnessite - type δ - MnO_2 (JCPDS No. 42 - 1317) [51]. As shown in the XPS results of Figure 2-3b, the Si 2p, Mn 2p, and O 1s signals were clearly observed, indicating the presence of Si, Mn, and O on the surface of SM NPs. Moreover, the high-resolution XPS spectra of Mn 2p and Si 2p (Figure 2-2c) further confirmed the presence of Mn and Si. The high-resolution XPS spectra of Mn 2p showed that the bandgap value between Mn 2p3/2 and Mn 2p1/2 was

around 11.8ev, suggesting the presence of the MnO_2 phase with Mn^{4+} ions in SM NPs [52]. The mass ratio of Mn in SM NPs analyzed through ICP analysis was 14.0% ± 2.6%.

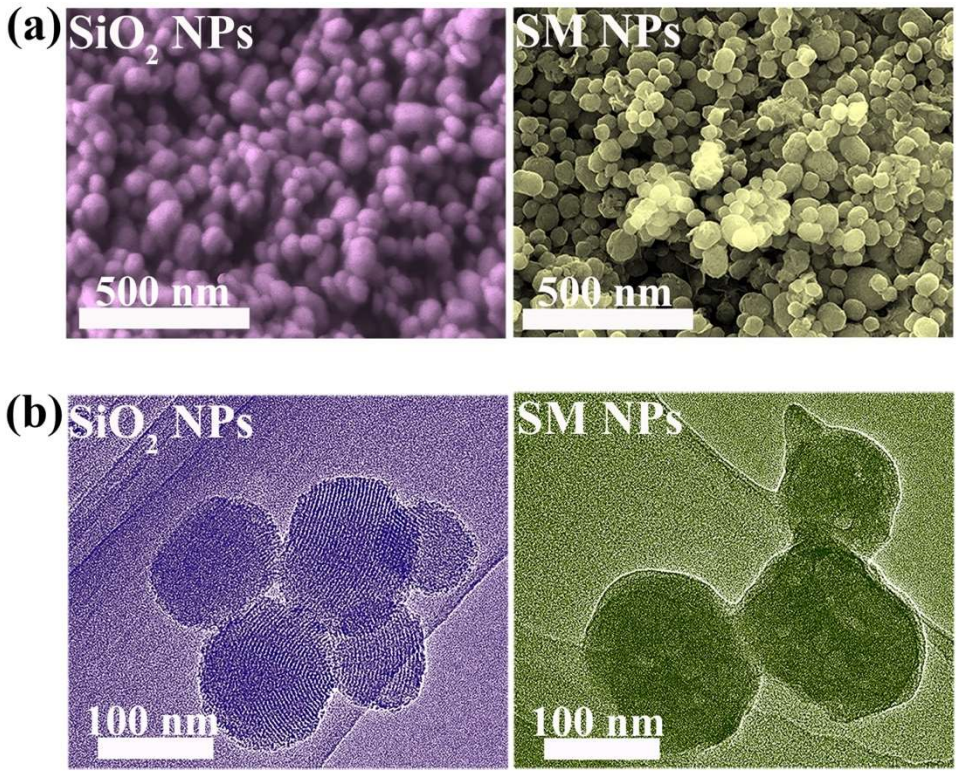

Figure 2-1 Morphology of SiO_2 NPs and SM NPs. (a) SEM images of SiO_2 NPs and SM NPs; (b) TEM images of SiO_2 NPs and SM NPs.

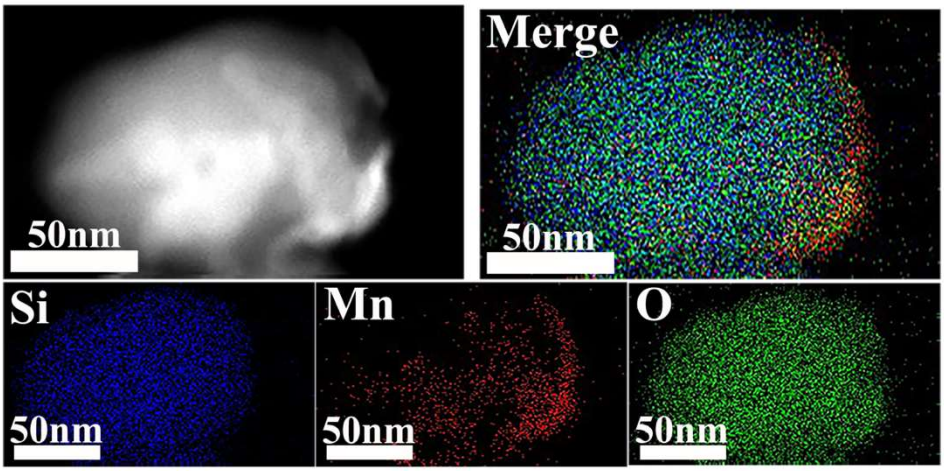

Figure 2-2 Element distribution of SM NPs

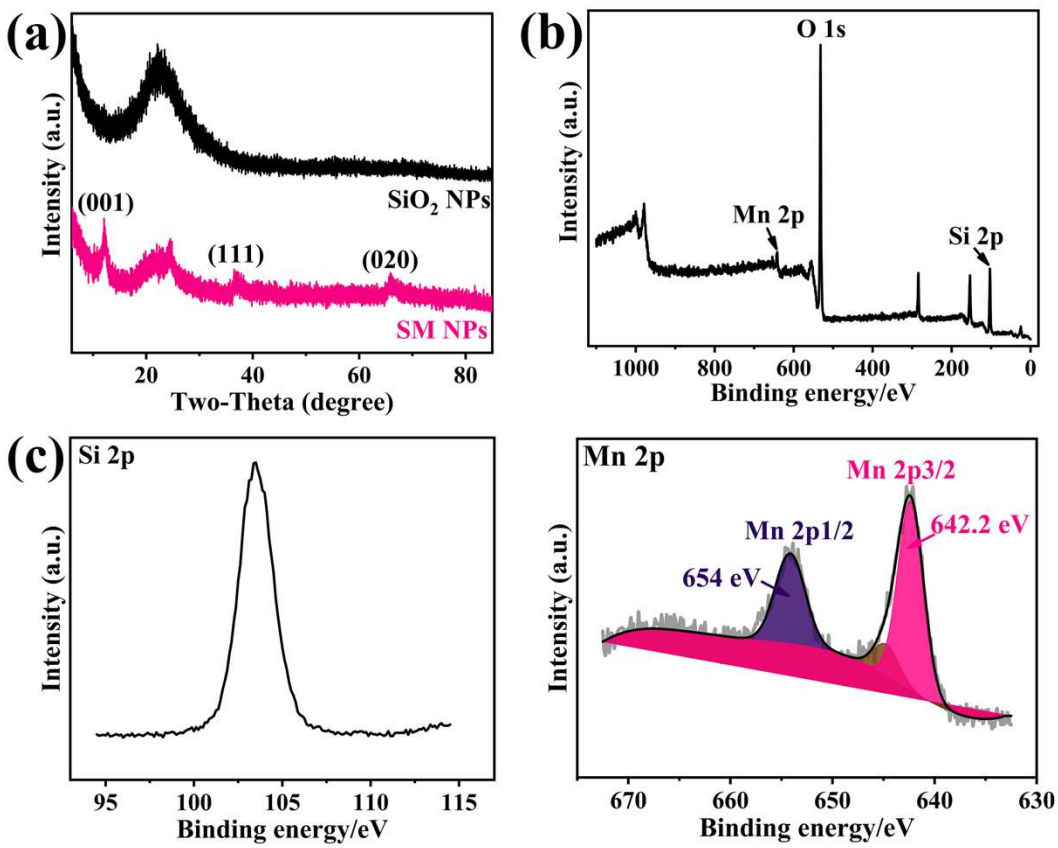

Figure 2-3 The phase and valence analysis. (a) XRD patterns of SiO_2 NPs and SM NPs; (b) Wide scan XPS spectra of SM NPs; (c) High - resolution XPS spectra of Si 2p and Mn 2p.

2.3.2 Regulation functions to TME

2.3.2.1 Oxygenation

SM NPs induced obvious oxygenation in solutions and LLC cells. The oxygenation was characterized by the fluorescence intensity decrease of $[Ru(dpp)_3]Cl_2$ (RDPP), which was used as an O_2 probe and its fluorescence can be quenched by O_2 [53].

2.3.2.1.1 Oxygenation in solutions

Firstly, the oxygenation induced by SM NPs was investigated in solutions containing H_2O_2 (Figure 2-4a). For the control group (solutions without SM NPs), the RDPP fluorescence intensity showed almost no change after 15 min of reaction, indicating that there was no change in O_2 level. On the other hand, for the group containing SM NPs of different concentrations, the RDPP fluorescence intensity decreased immediately after H_2O_2 was added and remained low, indicating that there was a marked increase in O_2 level. Besides, with the change in concentration of SM NPs or H_2O_2, the speed of decrease in RDPP fluorescence intensity was different, indicating the roles of SM NPs and H_2O_2 in inducing oxygenation.

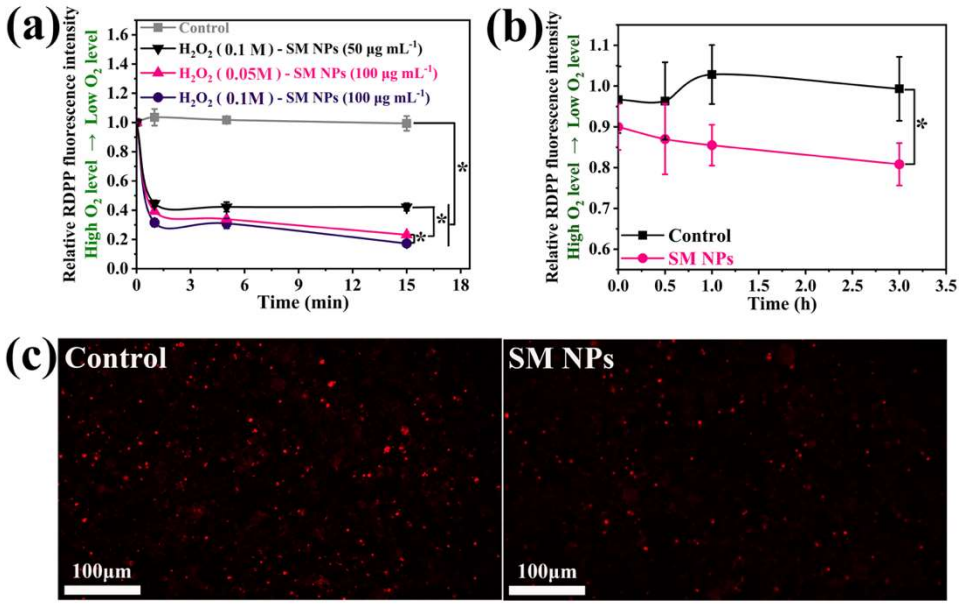

Figure 2-4 Oxygenation induced by SM NPs. (a) Extracellular oxygenation induced by SM NPs of different concentrations (n = 5); (b) Intracellular oxygenation level in LLC cells stained with RDPP measured with microplate reader (n = 6); (c) Fluorescence images of intracellular O_2 level of LLC cells stained with RDPP.

2.3.2.1.1 Oxygenation in LLC cells

Then, the intracellular oxygenation was further investigated in LLC cells using the O_2 probe of RDPP. As shown in Figure 2-4b, the RDPP fluorescence intensity in LLC cells stayed almost the same, indicating that there was no change in intracellular O_2 level, even after a 3h reaction. However, the RDPP fluorescence intensity in LLC cells incubated with SM NPs obviously decreased after a 3h reaction, indicating an obvious increase in intracellular O_2 level. Moreover, the fluorescence images in LLC cells also confirmed the oxygenation induced by SM NPs. As shown in Figure 2-4c, the red fluorescence of LLC cells incubated with SM NPs was lower than that of LLC cells, indicating that SM NPs could induce intracellular oxygenation and potentially relieve the intracellular hypoxia state in LLC cells.

2.3.2.2 ROS generation

The ROS generation induced by SM NPs was investigated in solutions and LLC cells. Mn^{2+} was proved to induce Fenton-like reactions to catalyze H_2O_2 and produce the highly cytotoxic ROS of •OH. In solutions, the level of •OH was detected through measuring the degradation of MB, and the factors that influence •OH generation were carefully investigated, including the role of HCO_3^-, the concentration of SM NPs, and the influence of GSH. In LLC cells, a probe of DCFDA was used to measure the level of all the kinds of ROS.

2.3.2.2.1 ROS generation in solutions

Firstly, H_2O containing SM NPs, H_2O_2, and GSH was utilized to investigate the •OH generation. As shown in Figure 2-5, no obvious MB degradation was observed in H_2O, indicating that SM NPs, H_2O_2, and GSH cannot generate •OH in H_2O.

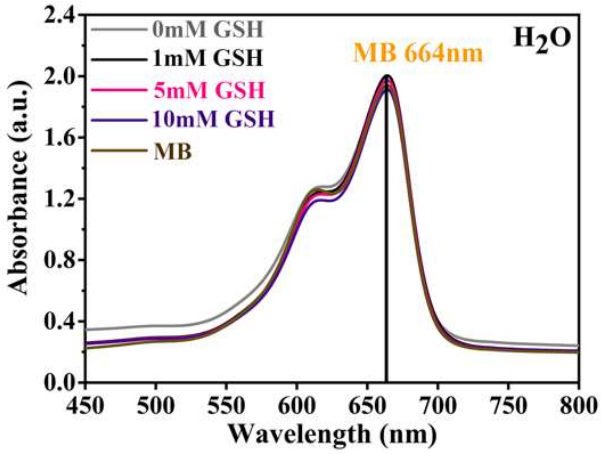

Figure 2-5 •OH generation induced by SM NPs in H_2O containing H_2O_2 and GSH of different concentrations (SM NPs = 30 μg mL^{-1}, H_2O_2 = 10 mM, MB = 10 μg mL^{-1}, reaction time = 0.5 h).

Then, the $NaHCO_3$ solution containing SM NPs, H_2O_2, and GSH was utilized to investigate the •OH generation. And the influence of the concentration of SM NPs and GSH was analyzed. Firstly, the influence of the concentration of SM NPs was investigated. As shown in Figure 2-6a, an obvious degradation of MB was observed in $NaHCO_3$ solution, and the degradation of MB showed the SM NPs concentration-dependent manner. At the SM NPs concentration of 90μg mL^{-1}, over 80% of MB was degraded, indicating the high efficiency of •OH generation induced by SM NPs at 90μg

mL^{-1}. Additionally, the •OH generation induced by SM NPs was further analyzed in a slightly acidic solution to mimic the acidic TME. As shown in Figure 2-6b, the SM NPs induced an obvious degradation of MB in a concentration-dependent manner, indicating that SM NPs could also induce the •OH generation in the slightly acidic solution.

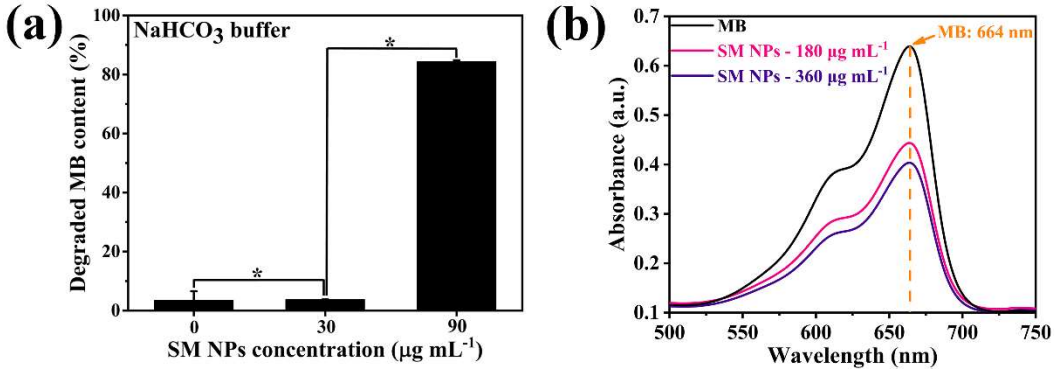

Figure 2-6 •OH generation induced by SM NPs in NaHCO3 solution. (a) •OH generation induced by SM NPs of different concentrations in GSH/NaHCO3 solution (n = 3, GSH = 5 mM, H2O2 = 10 mM, MB = 10 μg mL-1, reaction time = 0.5 h). (b) •OH generation induced by SM NPs in the slightly acidic solution.

Then, the influence of the concentration of GSH was investigated. As shown in Figure 2-7a, about 52% of MB was degraded in the $NaHCO_3$ solution without GSH, indicating a significant increase in the level of •OH generated through the Fenton-like reaction of Mn^{2+} degraded from SM NPs. With the increase in GSH concentration from 0 mM to 5 mM, the concentration of MB degraded tended to increase and reached the maximum of about 88%. Besides, the solution also showed different colors after the

reaction between SM NPs and GSH of different concentrations. With the increase in GSH concentration, the solution color changed from brown to colorless.

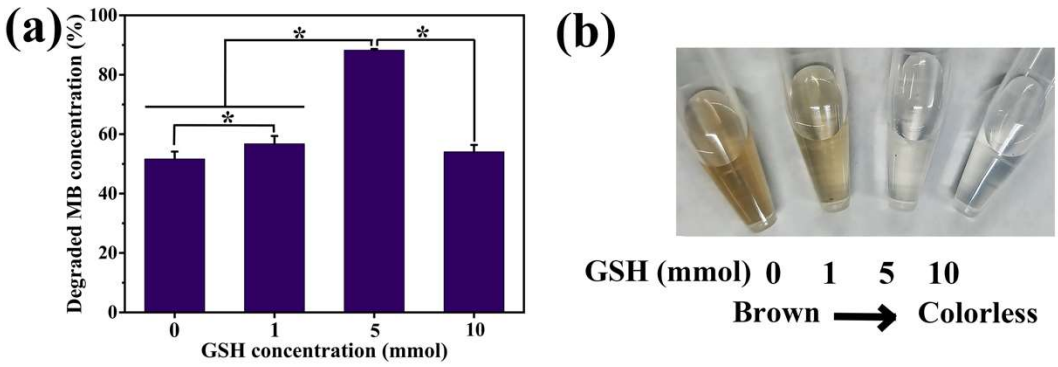

Figure 2-7 The effect of GSH on •OH generation. (a) The effect of different GSH concentrations on •OH generation (n = 5, SM NPs = 90 μg mL^{-1}, H_2O_2 = 10 mM, MB = 10 μg mL^{-1}, reaction time = 0.5 h). (b) The appearances of SM NPs - GSH solutions after 10 min reaction (SM NPs = 90 μg mL^{-1}, GSH = 0, 1, 5 and 10 mM)

Interestingly, after adding H_2O_2 and MB, the solution also showed different colors and air bubbles, as shown in Figure 2-8. With the increase in GSH concentration from 0 mM to 10 mM, the color changed from brown to colorless and blue. Moreover, with the increase in GSH concentration from 0 mM to 10 mM, the air bubbles decreased gradually. To further confirm the influence of GSH on oxygenation, the O_2 probe of RDPP was utilized to analyze the oxygenation in the H_2O_2 solution containing SM NPs and GSH. As shown in Figure 2-9, for the group containing SM NPs, the RDPP fluorescence intensity decreased to a low level after reaction for 15min, compared with the control group. Whereas the RDPP fluorescence intensity for the group containing SM NPs +GSH was higher than that for the group containing SM NPs after reaction for

15 min, indicating that GSH influenced the oxygenation induced by SM NPs. Notably, with extended reaction time, the RDPP fluorescence for the group containing SM NPs + GSH decreased gradually and became similar to that for the group containing SM NPs after reaction for 45 min.

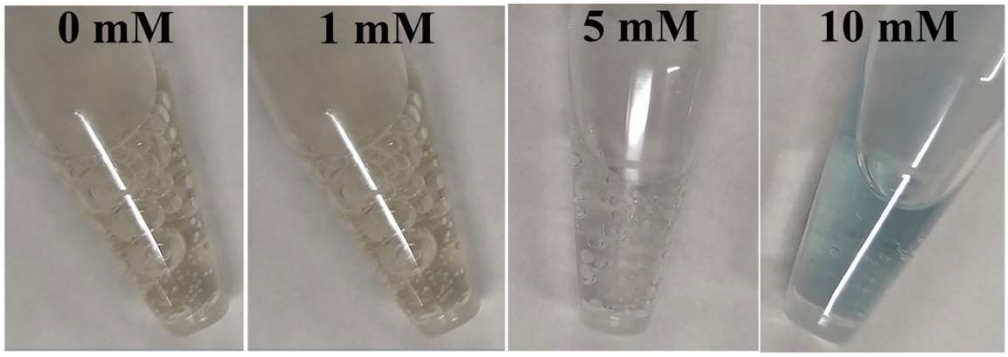

Figure 2-8 Images of air bubbles generated in SM NPs-GSH solutions after reaction with H_2O_2-MB for 30 min (SM NPs = 90 μg mL^{-1}, H_2O_2 = 40 mM, MB = 10μg mL^{-1})

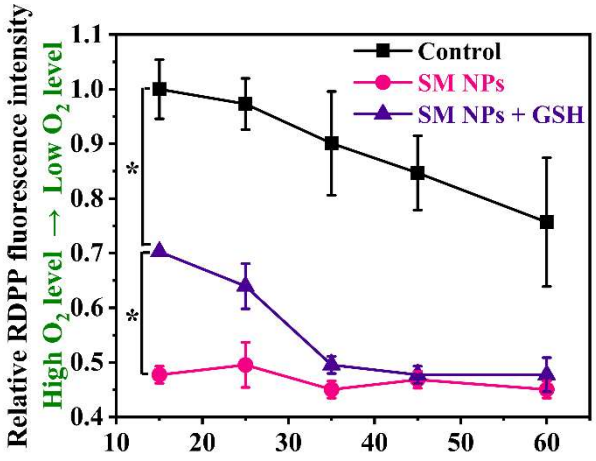

Figure 2-9 Oxygenation in H_2O_2 solution with the presence of GSH (10 mM) (n = 3).

Moreover, we measured the release of Mn from SM NPs in the acetic acid containing GSH (10 mM). As shown in Figure 2-10, the release of Mn increased with extended time. After reaction for 5d, the release of Mn almost showed no change compared with

4d, indicating that Mn was almost degraded 100%. And SM NPs showed different surface morphology with extended time as shown in Figure 2-11.

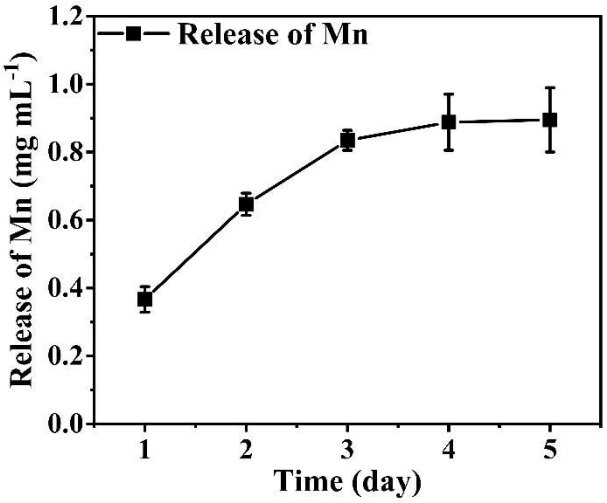

Figure 2-10 Mn release from SM NPs incubated with GSH (10 mM) (n = 3).

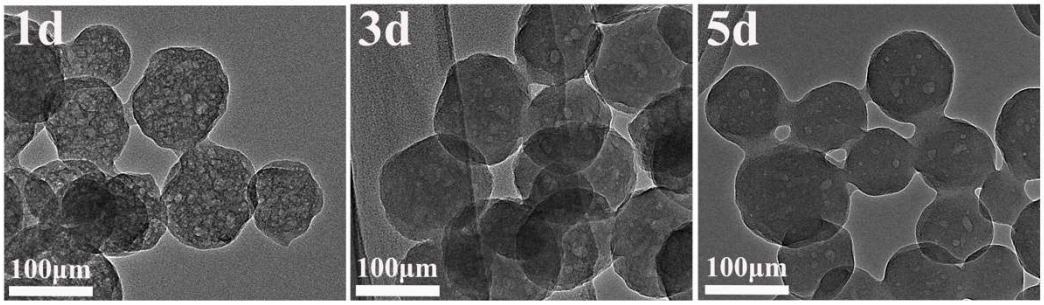

Figure 2-11 Degradation of SM NPs observed by TEM.

2.3.2.2.2 ROS generation in LLC cells

SM NPs obviously induced intracellular GSH depletion and ROS generation after incubation with LLC cells. The intracellular GSH content was tested using a GSSG/GSH quantification kit. As shown in Figure 2-12a, after incubation with LLC cells for 6h, SM NPs significantly induced a decrease in intracellular GSH content and

an increase in intracellular oxidized form glutathione (GSSG) content, indicating that SM NPs depleted GSH through converting the reduced GSH to oxidized GSSG in LLC cells. Moreover, GSH depletion can decrease ROS consumption and lead to more H_2O_2 remaining in cancer cells, thus enhancing the Fenton-like reaction to increase the •OH level in TME [57]. As shown in Figure 2-12b, SM NPs induced an obvious increase in intracellular ROS level after incubation with LLC cells in a concentration-dependent manner, which was consistent with the results shown in Figure 2-6a. Moreover, the fluorescence images (Figure 2-12c) of LLC cells incubated with SM NPs at different concentrations also showed that the SM NPs induced an obvious increase in intracellular ROS levels.

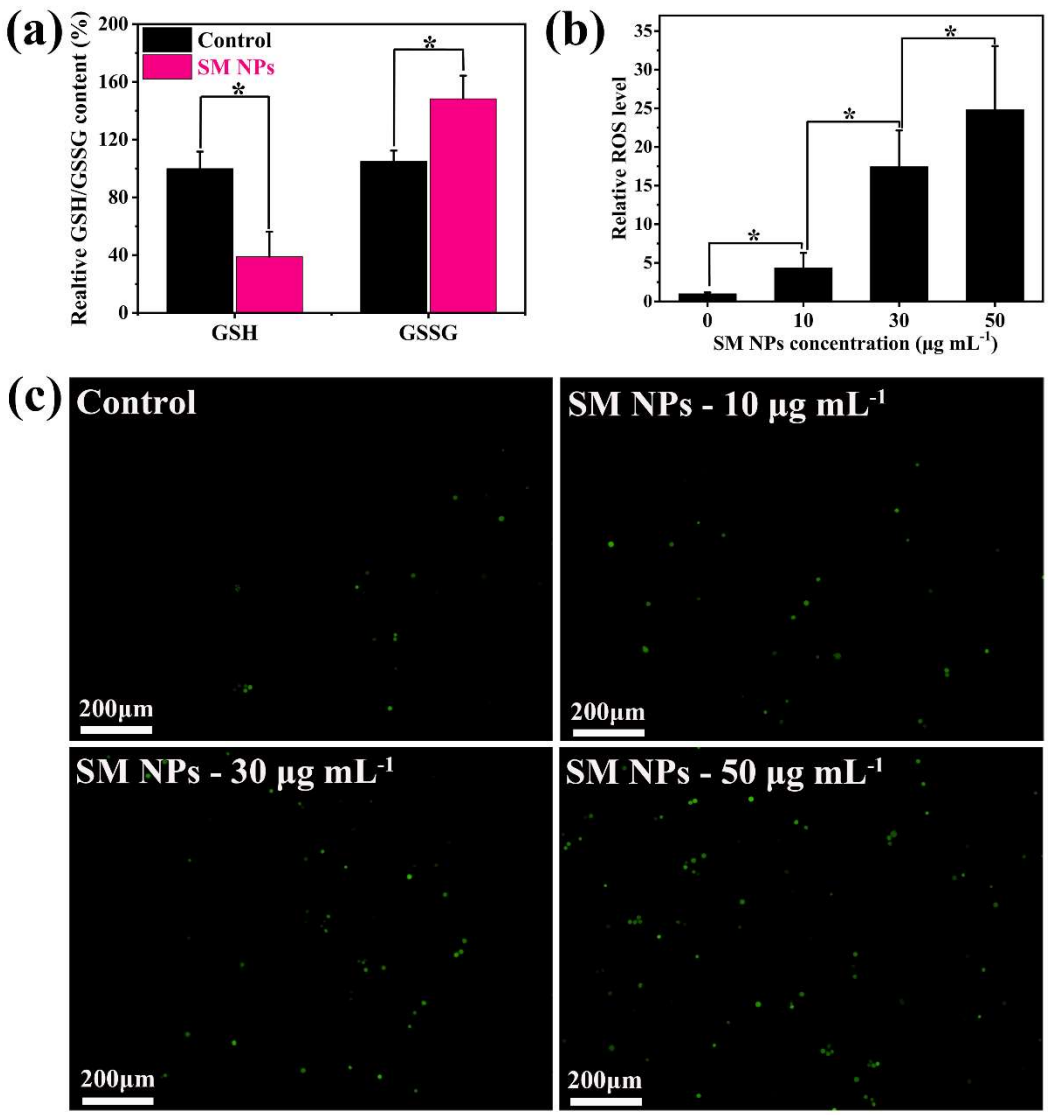

Figure 2-12 The effect of increasing ROS level induced by SM NPs. (a) Intracellular GSH/GSSG concentrations in LLC cells incubated with SM NPs (30 μg mL^{-1}) for 6 h (n = 3); (b) Intracellular ROS levels in LLC cells stained with DCFDA measured with microplate reader (n = 10); (c) Fluorescence images of intracellular ROS level of LLC cells stained with DCFDA. (Bar = 200 μm).

2.3.3 In vitro radiosensitization

2.3.3.1 Cytotoxicity

Firstly, the distribution of SM NPs in LLC cells was investigated through incubating the RhB-conjugated SM NPs (SM-RhB) with LLC cells overnight and observing the distribution of SM-RhB with a confocal laser scanning microscopy. As shown in Figure 2-13, the distribution of SM-RhB fluorescence signals overlapped almost completely with LysoTracker Green fluorescence signals, indicating that SM-RhB were mainly localized in lysosomes after cellular internalization.

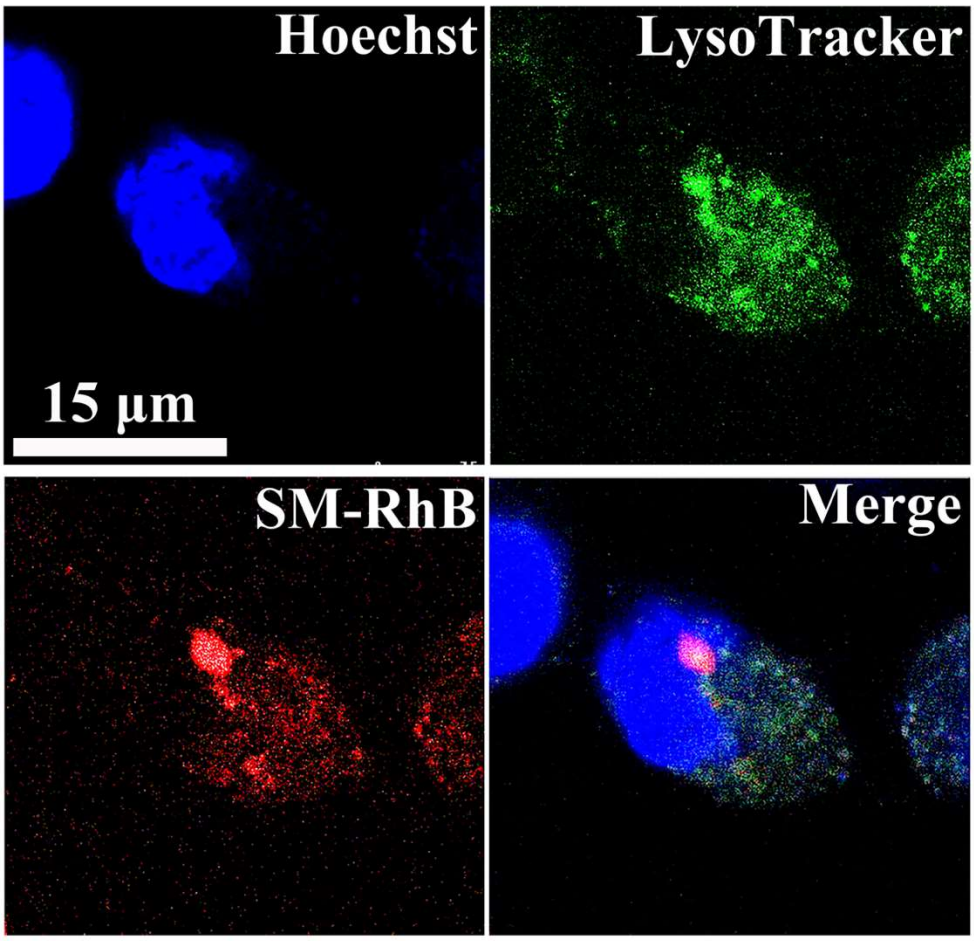

Figure 2-13 Confocal laser scanning microscopy images of LLC cells incubated with SM NPs (10 μg mL-1) (Bar = 15 μm).

Then the intracellular radiosensitization capacity of SM NPs was investigated. Different concentrations of SM NPs were incubated with LLC cells for 6h before exposure to radiation at 4Gy. As shown in Figure 2-14a, LLC cells treated with radiation alone showed almost the same viability as the non-treated LLC cells, indicating that radiation at 4Gy cannot kill LLC cells. However, when LLC cells were incubated with SM NPs alone at a concentration of 50 μg mL^{-1}, the SM NPs were obviously cytotoxic to LLC cells, indicating that SM NPs alone can produce enough highly cytotoxic •OH in TME to induce cell death [51]. Interestingly, the viability of LLC cells treated with the combination of radiation and SM NPs was more obviously reduced than that of LLC cells treated with SM NPs alone, indicating that SM NPs functioned as not only a CDT agent but also a radiosensitizer to improve RT efficacy in killing cancer cells. Furthermore, the radiosensitization capacity of SM NPs was confirmed by the live/dead cell staining as shown in Figure 2-14b. The combination of radiation and SM NPs induced the death of a large number of LLC cells, as indicated by the obvious red fluorescence signal.

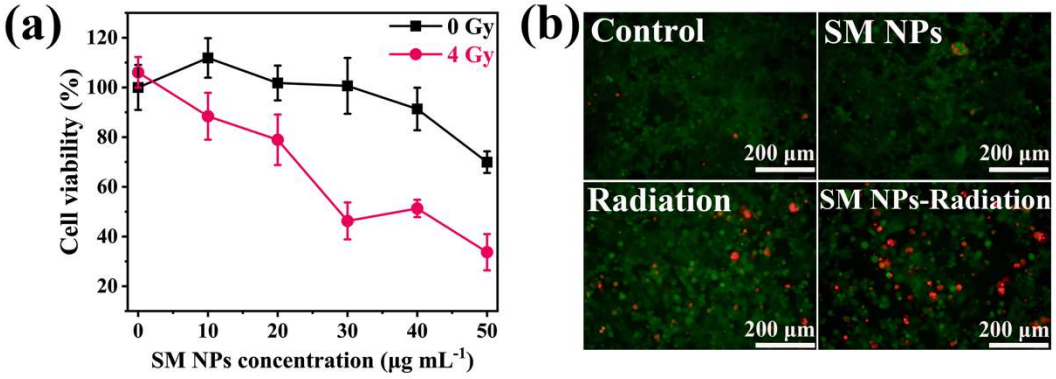

Figure 2-14 Radiosensitization induced by SM NPs. (a) Viability of LLC cells treated with the combination of radiation and SM NPs of different concentrations (n = 7); (b)

Fluorescence images of calcein - AM (green fluorescence)/PI (red fluorescence)-stained LLC cells treated with the combination of radiation and SM NPs (30 μg mL^{-1}) (Bar = 200 μm); (c) Confocal laser scanning microscopy images of LLC cells incubated with SM NPs (10 μg mL-1) (Bar = 15 μm).

2.3.3.2 In vitro mechanisms analysis

Since SM NPs obviously enhanced the cell-killing effect of radiation to LLC cells as shown in Figure 2-14, the cellular change in different aspects after radiation exposure was carefully investigated to reveal the mechanisms of radiosensitization induced by SM NPs, including the influence of ROS, GSH, GPx-4, LPO, DNA damage, and cytokine secretion.

1) ROS

SM NPs obviously enhanced intracellular ROS generation after radiation exposure. The intracellular ROS level in LLC cells after radiation exposure was also measured using the ROS probe of DCFDA. As shown in Figure 2-15a, radiation alone showed a very low level of ROS generated (about 2.4 times that of the control group), of which almost no cell death was induced as shown in Figure 2-14a. Whereas in the combination of radiation and SM NPs, the intracellular ROS level was significantly increased in an SM NPs concentration-dependent manner (15–56 times that of the control group), which was consistent with the results shown in Figure 2-7.

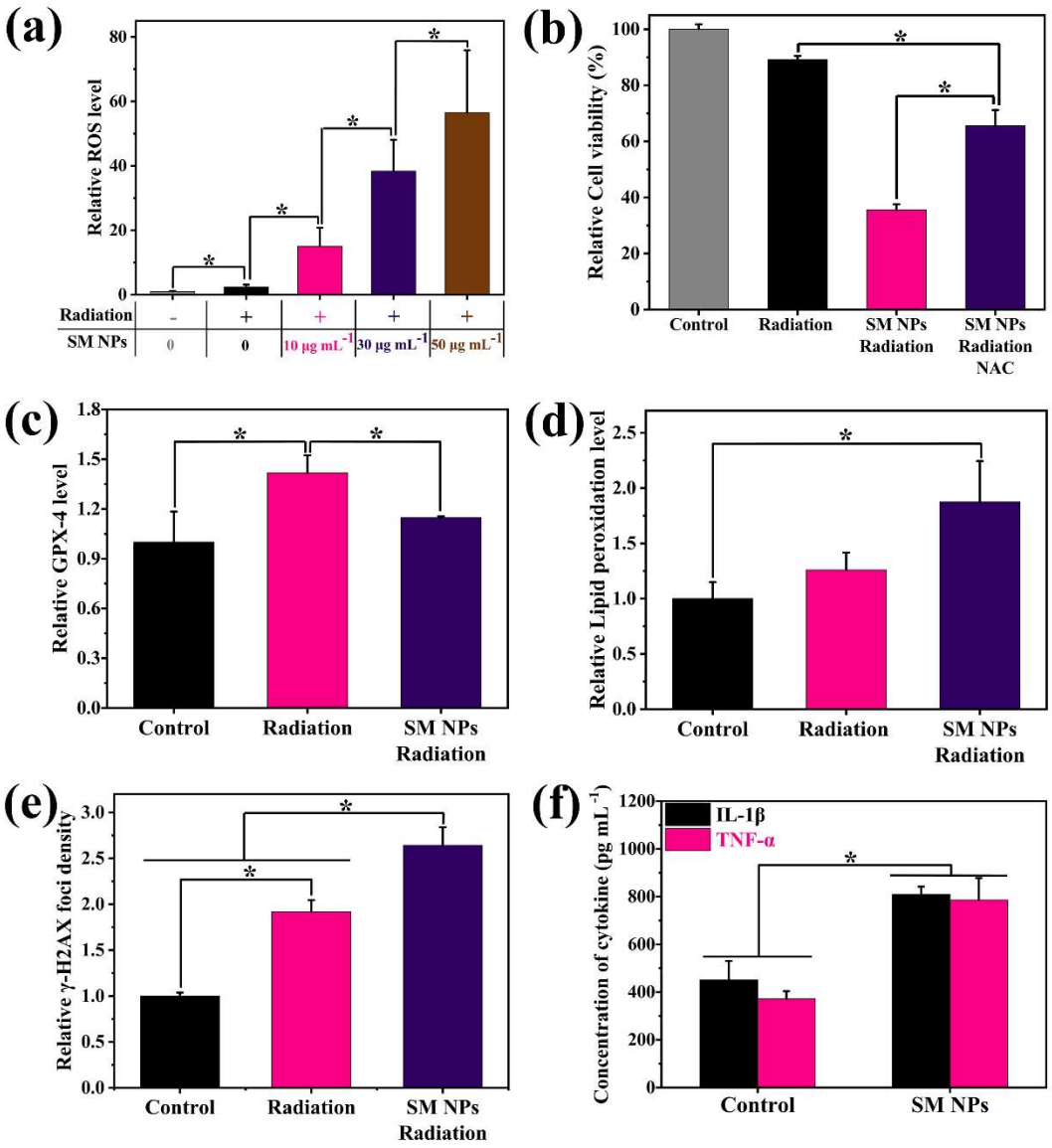

Figure 2-15 Mechanisms analysis of the radiosensitization induced by SM NPs. (a) Intracellular ROS levels (n = 10); (b) Influence of NAC on cell viability (n = 3); (c) Intracellular GPX - 4 levels (n = 3); (d) Intracellular LPO levels (n = 3); (e) Intracellular DNA damage levels (n = 3); (f) Amounts of cytokines secreted by macrophage-like cells incubated with SM NPs (n = 4).

2) GSH influence

The GSH level showed an obvious influence on the radiosensitization capacity of SM NPs. N-acetyl-l-cysteine (NAC), a precursor of GSH biosynthesis, was utilized to increase the GSH level. As shown in Figure 2-15b, the combination of radiation and SM NPs markedly decreased cell viability, whereas NAC supplementation increased cell viability by about 50% compared to the combination group.

3) GPx-4

SM NPs induced an obvious decrease in intracellular GPx-4 level in LLC cells exposed to radiation. GPx-4 is an intracellular enzyme, which is highly dependent on GSH content and eliminates intracellular ROS to enhance the antioxidation barrier in TME [14]. As shown in Figure 2-15c, treatment with radiation alone increased the intracellular GPx - 4 level owing to the metabolic reprogramming-induced increase in GSH content [64]. While, compared with the treatment with radiation alone, cells treated with the combination of radiation and SM NPs showed a decreased intracellular GPX - 4 level.

4) LPO

SM NPs induced an obvious increase in intracellular LPO level, which was due to the decrease in intracellular GPx-4 level. As shown in Figure 2-15d, compared with the control group, radiation alone increased the intracellular LPO level by about 26%.

Whereas the combination of radiation and SM NPs increased the intracellular LPO level by about 87% compared with the control group, which was significantly higher than that in the radiation-alone group.

5) DNA damage

SM NPs induced an obvious increase in DNA damage, which was detected as the γ-H2AX foci density. As shown in Figure 2-15e, there was a clear increase in γ-H2AX foci density in the radiation-alone group compared with the control group, suggesting that radiation at 4Gy increased the DNA damage level to 1.92 times that in the control group. Interestingly, the group treated with the combination of radiation and SM NPs showed a clearer increase in γ-H2AX foci density, which was 2.64 times that in the control group, indicating that SM NPs significantly enhanced the intracellular DNA damage of LLC cells after radiation exposure.

6) In vitro immune activation

SM NPs showed an obvious capacity in activating the immune system in vitro indicated by the enhanced cytokine secretion and the antigen presentation in vitro. As shown in Figure 2-15f, the contents of IL-1β and TNF-α was measured. SM NPs significantly enhanced the secretion of IL-1β and TNF-α, which is useful for the stimulation of anticancer immune responses. As shown in Figure 2-16, the antigen presentation was analyzed through measuring the population of MHC I+ cells.

macrophage-like cells showed the MHC I+ cells population of 2.0%, 2.5%, and 3.0% for SM NPs, OVA, and SM NPs-OVA, respectively. SM NPs-OVA showed the highest MHC I+ cells population among all the groups.

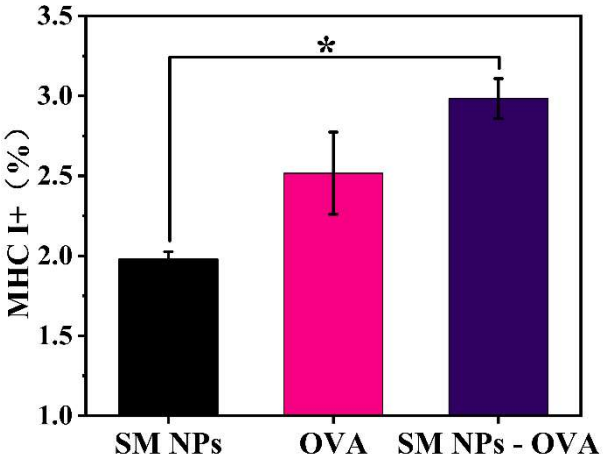

Figure 2-16 Quantitative analysis of MHC I+ cells population in macrophage-like cells cocultured with SM NPs - OVA (n = 3).

2.3.4 In vivo anticancer efficacy

2.3.4.1 In vivo anticancer effect of SM NPs-enhanced radio-immunotherapy

SM NPs obviously enhanced the abscopal effect of RT when mice were injected with SM NPs before exposure to radiation as shown in Figure 2-17a. As shown in Figure 2-17b, the growth of tumors in the mice treated with radiation alone or the combination of radiation and SM NPs was obviously inhibited compared with that of tumors in the mice not exposed to radiation (control group), suggesting the high efficacy of radiation at 6Gy. Notably, the distant untreated tumors in the hind legs on the right side showed different growth speeds depending on the treatment, as shown in Figure 2-17c. The

distant untreated tumors in the mice treated with radiation alone grew quickly; this observation was not significantly different from that in the mice not exposed to radiation (control group), suggesting that the abscopal effect of RT was far from satisfactory [4,5]. However, the combination of radiation and SM NPs clearly inhibited the growth of distant untreated tumors, suggesting that SM NPs can activate the anticancer immune responses and enhance the abscopal effect of RT at 6Gy. To further confirm the immune activation capacity of SM NPs, cytokine secretion from splenocytes was investigated. As shown in Figure 2-17d, a significant increase in the amount of TNF-α secreted was observed in splenocytes.

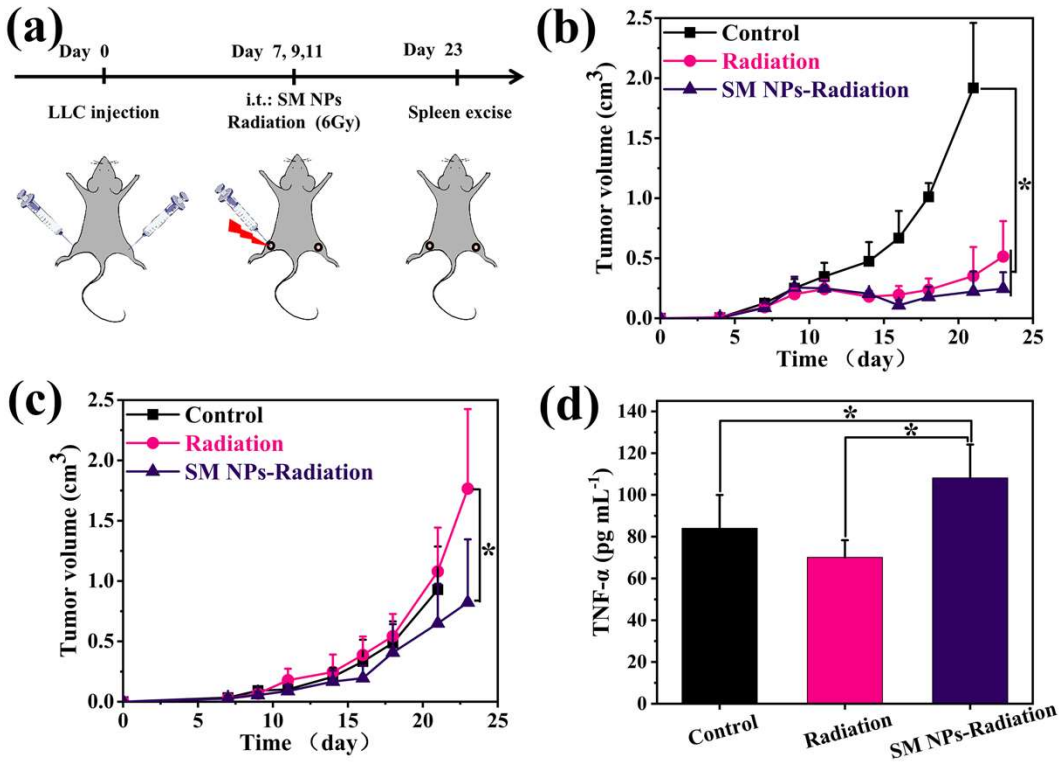

Figure 2-17 In vivo anticancer efficacy of SM NPs - enhanced radio-immunotherapy (n=5). (a) The scheme of experimental schedule of radio – immunotherapy; (b) Average tumor growth curves of primary tumors in the hind legs on the left side; (c) Average

tumor growth curves of distant untreated tumors in the hind legs on the right side; (d) Amounts of cytokine secreted from splenocytes.

2.3.4.2 In vivo anticancer effect of SM NPs - enhanced radio - immunotherapy in combination with the anti-CTLA-4 antibody

With the pre-injection of SM NPs and the anti-CTLA-4 antibody before exposure to radiation (Figure 2-18a), a more obvious inhibition effect on distant untreated tumors was observed at a lower radiation dose at 4Gy. To explore the in vivo radiosensitization capacity of SM NPs on the primary tumors and reduce the side effects of radiation on surrounding healthy tissues, we reduced the radiation dose to 4Gy. As shown in Figure 2-18b, the treatment of radiation alone only minimally inhibited primary tumor growth; this observation was not significantly different from that in the group not exposed to radiation (control group). However, combining radiation with SM NPs, the anti-CTLA-4 antibody or SM NPs and the anti-CTLA-4 antibody induced a clear inhibitory effect on primary tumor growth compared with treatment without radiation, suggesting that SM NPs improved the efficacy of RT at a low dose that does not have an inhibitory effect when used alone in vivo. These results were consistent with in vitro results as shown in Figure 2-14a. Figure 2-18c showed the growth of distant untreated tumors in the hind legs on the right side. Combining radiation with SM NPs and the anti-CTLA-4 antibody significantly inhibited the growth of distant untreated tumors. However, combining radiation with SM NPs alone or the anti-CTLA-4 antibody alone did not

inhibit the growth of distant untreated tumors, and the tumors grew fast as shown in Figures 2-18(d–e), implying that SM NPs alone or the anti-CTLA-4 antibody alone did not enhance the abscopal effect of RT at 4Gy. Notably, among the mice treated with the combination of radiation and SM NPs and the anti-CTLA-4 antibody, 40% showed total suppression of tumor growth and 40% showed a slow tumor growth as compared with mice in other groups (Figure 2-18e), implying that the combination of SM NPs and the anti-CTLA-4 antibody synergistically enhanced the abscopal effect of RT at 4Gy. Specifically, mice treated without radiation, and those treated with radiation alone, the combination of radiation and SM NPs, the combination of radiation and the anti-CTLA-4 antibody, and the combination of radiation and SM NPs and the anti-CTLA-4 antibody were tumor-free at percentages of 0%, 0%, 0%, 0%, and 40% at distant untreated sites, respectively. Furthermore, the cytokine secretion from splenocytes indicated that the combination of radiation and SM NPs and the anti-CTLA-4 antibody induced the highest immune activation compared with other combinations. As shown in Figures 2-18(f-h), the secretions of interferon-γ (IFN-γ), IL-1β, and IL-6 were enhanced in mice treated with the combination of radiation and SM NPs and the anti-CTLA-4 antibody.

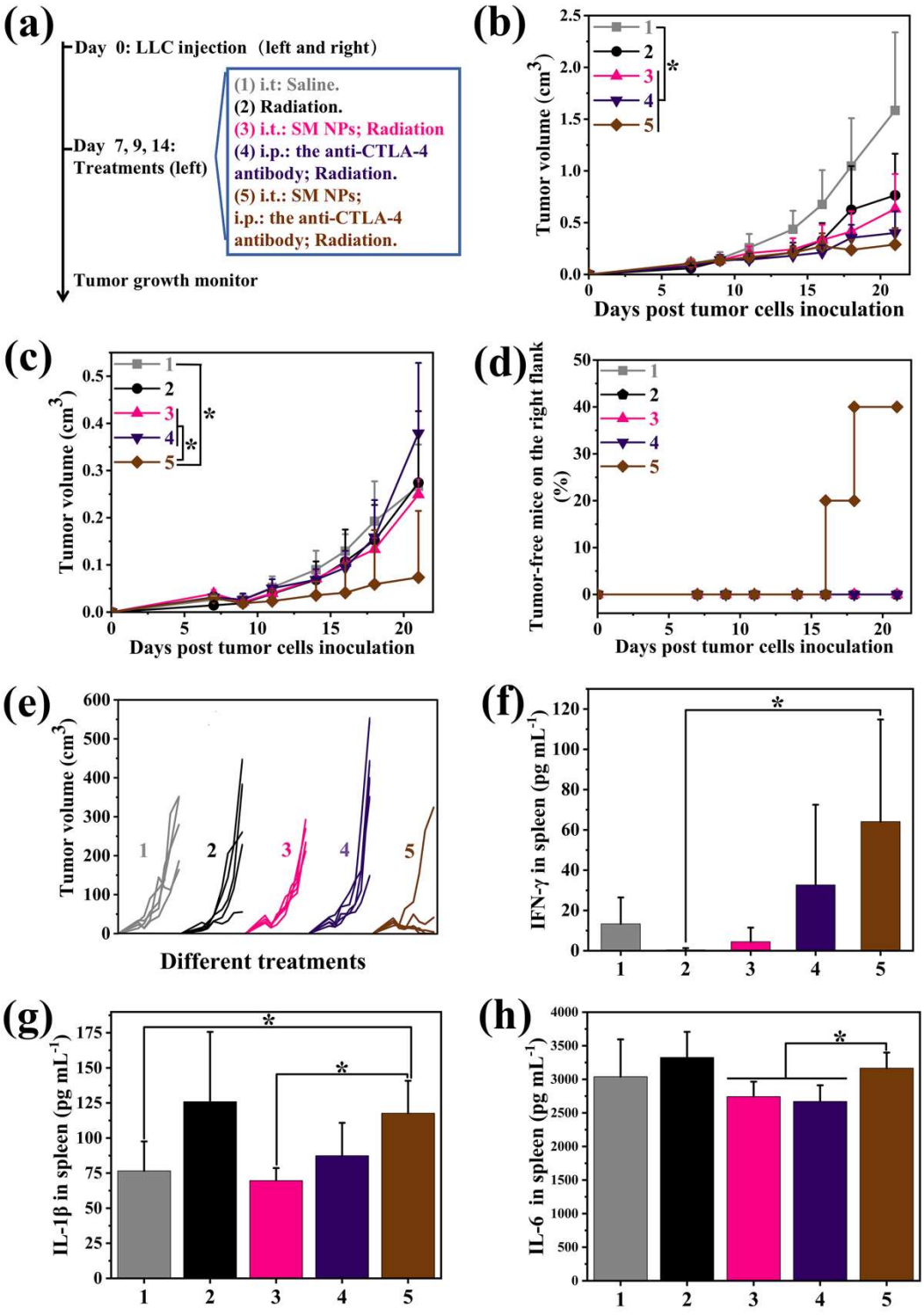

Figure 2-18 In vivo anticancer efficacy of SM NPs - enhanced radio - immunotherapy in combination with the anti - CTLA - 4 antibody (n = 5). (a) The scheme of the experimental schedule of radio-immunotherapy; (b) Average tumor growth curves of primary tumors in the hind legs on the left side; (c) Average tumor growth curves of

metastatic tumors in the hind legs on the right side; (d) The ratio of tumor - free mice in the hind legs on the right side; (e) Corresponding individual growth curves of tumors in the hind legs on the right side; (f) Amounts of IFN-γ secreted from splenocytes; (g) Amounts of IL - 1β secreted from splenocytes; (h) Amounts of IL - 6 secreted from splenocytes.

2.3.4.3 Analysis of activated immune cells in SM NPs-enhanced radio-immunotherapy in combination with the anti-CTLA-4 antibody

To further confirm the immune activation by SM NPs, the activated immune cells was analyzed. As shown in Figure 2-19, mice treated with radiation alone, the combination of radiation and SM NPs, the combination of radiation and the anti-CTLA-4 antibody, and the combination of radiation and SM NPs and the anti-CTLA-4 antibody showed the population of CD 8+ T cells of 9.2%, 10.5%, 9.4%, and 10.1%, respectively. Mice treated with radiation alone, the combination of radiation and SM NPs, the combination of radiation and the anti-CTLA-4 antibody, and the combination of radiation and SM NPs and the anti-CTLA-4 antibody showed a population of CD 4+ T cells of 10.9%, 10.4%, 12.3%, and 11.2%, respectively. Compared with mice treated with radiation alone, mice treated with the combination of radiation and SM NPs and the anti-CTLA-4 antibody obviously enhanced the population of CD 8+ T cells in splenocytes.

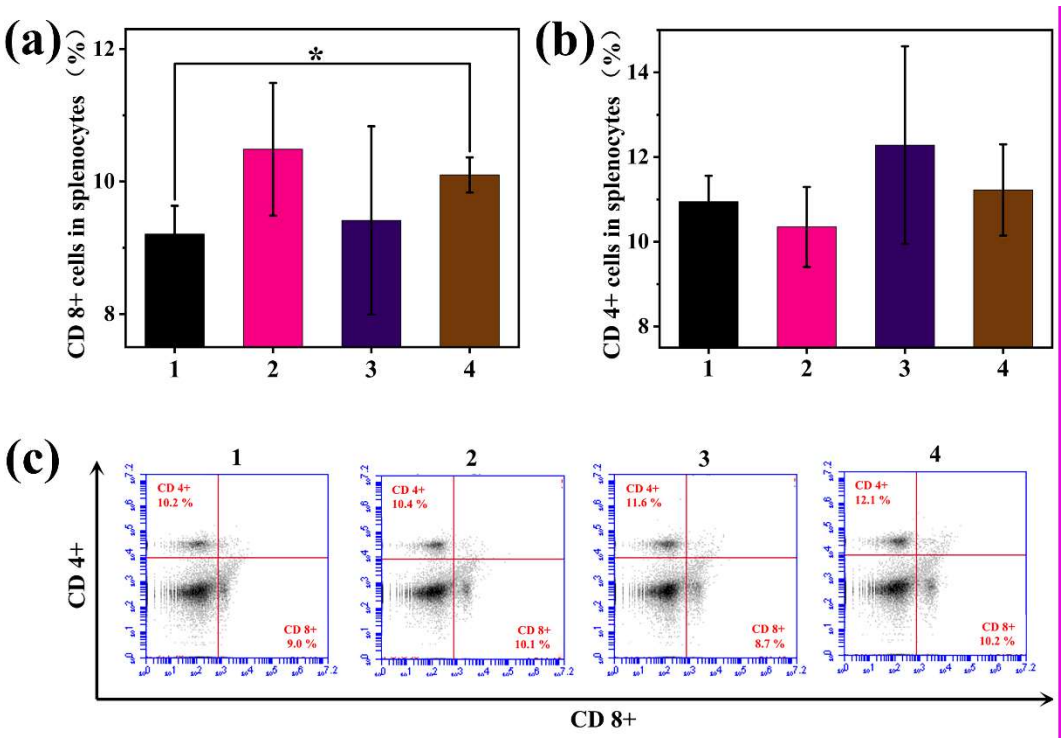

Figure 2-19 In vivo analysis of immune cells activated. (a) CD 8+ cells in splenocytes (n = 3); (b) CD 4+ cells in splenocytes (n = 3); (c) Representative flow cytometry histogram of activated immune cells in splenocytes

2.4 Discussion

According to the results of SEM (Figures 1-1), TEM (Figures 1-2), XRD, and XPS (Figure 2-3), Mn was successfully coated onto SiO_2 NPs through a simple hydrothermal method. The process of Mn coating showed no obvious influence on the size of SiO_2 NPs, as shown in Figure 2-1 and Figure 2-2. Moreover, the presence of the MnO_2 phase with Mn^{4+} ions was proved by XPS analysis as shown in Figures 1-3(b-c). MnO_2, as a kind of redox-active transition-metal dioxide nanomaterial, possesses the obvious catalytic ability, including the high reactivity toward H_2O_2 to produce O_2, due to the

intermediate valence state of Mn^{4+} [54]. Therefore, the presence of the MnO_2 phase with Mn^{4+} ions endowed SM NPs with the capacity of inducing oxygenation in the presence of H_2O_2 [33]. As shown in Figure 2-4a, SM NPs induced obvious oxygenation in solutions containing H_2O_2. Moreover, the complex TME is usually featured with hypoxia and elevated H_2O_2 levels (100 μM-1 mM), which is due to the high proliferation of cancer cells and the induced abnormal redox balance. Therefore, an obvious increase in O_2 was also observed in LLC cells incubated with SM NPs for 3h, as shown in Figures 1-4(b-c), which was consistent with the oxygenation in solutions containing H_2O_2 (Figure 2-4a).

Moreover, Mn-based nanomaterials have been widely applied to CDT due to the potential of Mn^{2+} in inducing Fenton-like reactions and producing •OH, one of the most cytotoxic ROS. Interestingly, TME is not only featured with hypoxia and elevated H_2O_2 levels, but also featured with abundant GSH, one of the essential antioxidants in the powerful antioxidative systems, and acidic pH values, which both contribute to reducing MnO_2 and producing Mn^{2+} as following equations (1) - (3). The produced Mn^{2+} can further trigger Fenton-like reactions and produce •OH, which contributed to the ROS generation in both solutions and LLC cells as shown in results from Figure 2-5 to Figure 2-12.

(1) $MnO_2 + GSH \rightarrow Mn^{2+} + GSSG$

(2) $MnO_2 + 2H^+ \rightarrow Mn^{2+} + H_2O + 1/2\ O_2$

(3) $MnO_2 + H_2O_2 + 2H^+ \rightarrow Mn^{2+} + 2H_2O + O_2$

As shown in results from Figure 2-5 to Figure 2-8, SM NPs could induce the generation of the highly cytotoxic ROS of •OH in the presence of the $NaHCO_3$ solution, which was consistent with former studies [51]. On the one hand, GSH can convert the MnO_2 in SM NPs to Mn^{2+} through reducing the -Mn-O- bonds to Mn^{2+} as described in the above equation (1) to enhance Mn^{2+}-induced Fenton-like reactions and increase the ROS levels. On the other hand, GSH, as one of the essential antioxidants in the powerful antioxidative systems to scavenge ROS can be also depleted by MnO_2 in SM NPs through oxidizing GSH to GSSG as described in the above equation (1), which further contributed to the increase in ROS levels. Therefore, GSH obviously promoted the generation of •OH when its concentration increased from 0 mM to 5 mM. Whereas a decrease in the generation of •OH after further increasing the concentration of GSH to 10 mM was observed. This was due to the excessive GSH scavenged parts of •OH generated, which impedes the effect of many ROS-based anticancer therapies. Besides, the color of solutions changing from brown to colorless after mixing SM NPs with GSH also suggested the redox reaction between SM NPs and GSH. And, after further adding H_2O_2 and MB, the mixed solutions showed different colors and air bubbles. Different colors indicated different levels of •OH generated. With the increase in GSH concentration from 0 mM to 10 mM, the appearances of the SM NPs-GSH-MB solutions changed from brown to colorless and blue. When the GSH concentration was increased to 10 mM, a portion of generated •OH was scavenged due to the excessive GSH, leading to a low •OH level and accordingly a low concentration of MB degraded.

Therefore, the SM NPs-GSH-MB solution appeared blue, indicating the presence of undegraded MB. Different air bubbles indicated different levels of O_2 generated. The amount of air bubbles in the SM NPs-GSH-MB solution without GSH was more obvious than that in the SM NPs-GSH-MB solutions containing GSH, suggesting that all of SM NPs acted as the enzyme to produce O_2. Whereas in the solution containing an excessive amount of 10 mM GSH, almost no air bubbles were produced, suggesting that SM NPs induced no oxygenation. This phenomenon may be caused by the strong redox reaction, by which MnO_2 in SM NPs was almost completely degraded by GSH (Fig. 1-3d). Accordingly, the oxygenation capacity of MnO_2 in SM NPs was suppressed. The redox reaction between SM NPs and GSH can be further confirmed by the release of Mn from SM NPs and the change in the morphology of SM NPs (Figure 2-10 and Figure 2-11). And the relationship between GSH, ROS, and SM NPs was also observed in LLC cells, which confirmed the intracellular GSH depletion and ROS generation induced by SM NPs (Figure 2-12).

The oxygenation, GSH depletion, and ROS generation induced by SM NPs synergistically contributed to the enhanced cell-killing effect of RT. As shown in Figure 2-14, SM NPs alone at the concentration of 50μg mL^{-1} and the combination of radiation and SM NPs at the concentration of 10-50μg mL^{-1} both caused obvious cytotoxicity to LLC cells, which was considered to be related to the intracellular change in TME after incubated with SM NPs. As shown in Figure 2-15, cells incubated with SM NPs before radiation showed obviously higher intracellular ROS levels than cells treated with

radiation alone. As the major source of oxidative stress, ROS has different types, including superoxide (O_2^-), hydroxyl radicals (•OH), hydrogen peroxide (H_2O_2), and singlet oxygen ($^1O_2$), which is mainly generated through the metabolism of oxygen [55] Firstly, SM NPs induced oxygenation utilizing the elevated H_2O_2 in TME, which enhanced the ROS generation through oxygen metabolism and radiation. Secondly, MnO_2 in SM NPs converted to Mn^{2+} in TME and Mn^{2+} generated induced the Mn^{2+}-based Fenton-like reaction to produce highly cytotoxic ROS of •OH. Thirdly, MnO_2 in SM NPs depleted abundant antioxidant GSH, which decreased the ROS consumption induced by GSH, thus increasing intracellular ROS levels indirectly. These three pathways synergistically contributed to the increase in intracellular ROS levels in LLC cells treated with SM NPs and radiation.

Additionally, there is a powerful antioxidative system in TME to keep the intracellular redox state balance, which contains antioxidative molecules and enzymes, including GSH, peroxiredoxin (Prx), thioredoxin (Trx), SOD, and catalase [56]. Take GSH for example, GSH can react with a cofactor of GSH per-oxidase (GPx) and/or participation in other antioxidant components [57, 58]. Therefore, using NAC to increase the synthesis of intracellular GSH could decrease the cytotoxicity induced by the combination of radiation and SM NPs (Figure 2-15b), which also confirmed the GSH depletion induced by SM NPs indirectly. Moreover, ROS generation and GSH depletion also induced other changes in TME. Firstly, an obvious change in the GPx-4 level was observed. GPx-4 is an intracellular enzyme that is highly dependent on GSH

content and eliminates intracellular ROS to enhance the anti-oxidation barrier in TME [14]. The intracellular GPx-4 level increased after radiation due to the metabolic reprogramming-induced increase in GSH content [59]. Whereas, the combination of radiation and SM NPs decreased the GPx-4 level, which was attributed to the SM NPs-induced decrease in GSH content and Mn^{2+}-driven Fenton-like reaction-induced increase in •OH level [14]. Both the GSH depletion and GPx-4 downregulation functions of SM NPs contributed to the weakening of the antioxidation barrier [60], which can further enhance the RT efficacy. Moreover, GPx-4 can reduce the accumulation of lipid free radicals through reducing toxic PL-PUFA-OOH to non-toxic PL-PUFA-OH, which was confirmed by the increase in LPO levels as shown in Figure 2-15d. Accordingly, the increased ROS and LPO reacted with DNA directly and induced an obvious increase in DNA damage, which was indicated by the increase in γ-H2AX foci density as shown in Figure 2-15e. Moreover, previous research indicated that Si-based and Mn-based could potentially activate the immune response [34-38, 42-49]. MS nanoparticles can significantly enhance the Th1 and Th2 immune responses and promote the accumulation of effector memory T cells. Mn^{2+} is important in the innate immune sensing of tumors, which can significantly enhance the maturation of dendritic cells (DCs) and macrophages, antigen presentation, as well as the activation of CD 8+ T cells and natural killer (NK) cells. In this study, SM NPs significantly enhanced the secretion of IL-1β and TNF-α in vitro, which is useful for the stimulation of anticancer immune responses. IL-1β and TNF-α are both important pro-

inflammatory cytokines, which can stimulate macrophage proliferation [61, 62]. Additionally, SM NPs-OVA also enhanced the antigen presentation in vitro indicated by the increased MHC I+ cells population as shown in Figure 2-16. MHC I molecules on the surface of macrophage-like cells were reported to mediate antigen presentation. The cross-presentation of exogenous antigens on MHC I molecules was essential for priming CD 8+ T - cell responses and played a vital role in anticancer immunity. Therefore, we considered that the SM NPs may have the potential to cure metastatic tumors through the activation of anticancer immune responses.

On the basis of the capacities of regulation functions to TME and stimulation of anticancer immune responses, SM NPs showed obvious enhancement in the in vivo anticancer effect of RT as shown in Figure 2-17. Mn^{2+} was proved to activate the DNA damage-induced cGAS/STING pathway and enhance the abscopal effect of RT [34-36]. Whereas radiation at 4Gy could not cause enough DNA damage because of no cells-killing effect as shown in Figure 2-14a. Therefore, we increased the radiation to 6Gy to induce higher cell-killing efficiency and higher DNA damage, which was furtherly combined with SM NPs to explore the enhancement on the abscopal effect of RT by SM NPs alone. As a result, SM NPs showed a clear enhancement on the abscopal effect of RT as indicated by the inhibitory effect on the growth of distant and untreated tumors. Moreover, SM NPs also improved the secretion of TNF-α by splenocytes, which was produced by T helper (Th) 1 cell and related to the cell-mediated inflammatory reaction,

as well as able to enhance the maturation of DCs and activation of CD 8+ T cells [63-65].

Whereas the enhanced abscopal effect of RT by SM NPs alone was far from satisfaction. Therefore, the anti-CTLA-4 antibody was utilized to further improve the abscopal effect of RT. According to some preclinical and clinical studies, the anti-CTLA-4 antibody made the abscopal effect of RT more common and RT could enhance the systemic response to the anti-CTLA-4 antibody [7, 66]. Moreover, considering the low tolerance of normal tissues to radiation, the radiation dose was reduced to 4Gy to reduce the side effects of radiation on surrounding healthy tissues. Interestingly, the combination of radiation and SM NPs and the anti-CTLA-4 antibody showed an obvious inhibitory effect on both primary tumors and distant untreated tumors, indicated by the inhibited growth of primary tumors and distant untreated tumors, the enhanced secretion of cytokines by splenocytes, as well as the increase in activated immune cells populations. Our results were consistent with previous studies, which showed that the combination of radiation and the anti-CTLA-4 antibody could synergistically activate the CD 8+ anticancer T-cell response and enhance the recruitment of activated CD 8+ cells to the tumor sites treated with radiation, thus inhibiting lung micrometastasis [7]. The activation of anticancer immune responses was considered to be related to four factors. Firstly, SM NPs significantly enhanced intracellular DNA damage after radiation exposure (Figure 2-15e), which may lead to the direct enhancement of the activation of the DNA damage-induced cGAS/STING

pathway in RT [39, 40]. DNA damage induced by the combination of radiation and SM NPs could leak into the cytosol, be recognized by cGAS, and induce cGAMP production, which further bind with STING and induce secretion of IFN and related proinflammatory cytokines [39, 40, 67-73]. Secondly, SM NPs generated Mn^{2+} after reaction with GSH, which may further enhance the activation of the cGAS/STING pathway. Mn^{2+} was reported to stimulate cGAS to synthesize 2′3′ - cyclic GMP-AMP (cGAMP) and augment cGAMP-STING binding affinity [34-36]. Thirdly, the intracellular oxygenation capacity of SM NPs was considered to potentially relieve the hypoxia in TME (Figure 2-4), which may also relieve the hypoxia-induced immunosuppression [74]. Lastly, our previous research studies showed that Si-based nanomaterials could activate immune responses, which accelerated the proliferation of lymphocytes, stimulated cytokine secretion, and improved the effector memory CD 4+ and CD 8+ T cell populations [42-49]. SiO_2 NPs could influence macrophage polarization and further influence immune responses [75, 76]. SiO_2 NPs could upregulate the level of MHC-II, CD 80, and CD 86 in DCs, and activate p38 and NF-κB [77]. This might also contribute to the activation of anticancer immune responses. Taken together, the immune activation potential of both Mn and Si endowed SM NPs with strong immune activation capacity to enhance the abscopal effect of RT. Therefore, combining radiation with SM NPs and the anti-CTLA-4 antibody induced a strong inhibitory effect on distant untreated tumors.

2.5 Conclusions

In this work, core-shell structured SM NPs were synthesized for use in synergistic radio-immunotherapy. SM NPs regulated TME to a status beneficial for radio-immunotherapy through O_2 production in situ to relieve hypoxia, •OH production, and GSH depletion to increase ROS levels, as well as through promotion of cytokine secretion to stimulate anticancer immune responses. Notably, SM NPs not only inhibited the growth of primary tumors at a low radiation dose at which radiation alone has no effect, but also suppressed the growth of distant untreated tumors. Taken together, these results demonstrated that the application of SM NPs may provide an effective choice for TME-responsive radio-immunotherapy. However, further research studies to analyze in detail the mechanism by which SM NPs function in radio-immunotherapy are required, including the in vivo regulation functions for TME, the type of dose fractionation regimen, the stimulation of the cGAS/STING pathway, the molecular mechanism of immune activation, the efficiency on other cancers and other anticancer therapies, and so on.

Reference

1. Ross G: **Induction of cell death by radiotherapy**. *Endocrine-related cancer* 1999, **6**(1):41-44.

2. Lomax M, Folkes L, O'neill P: **Biological consequences of radiation-induced DNA damage: relevance to radiotherapy**. *Clinical oncology* 2013, **25**(10):578-585.

3. Ngwa W, Irabor OC, Schoenfeld JD, Hesser J, Demaria S, Formenti SC: **Using immunotherapy to boost the abscopal effect**. *Nature Reviews Cancer* 2018, **18**(5):313-322.

4. Song G, Cheng L, Chao Y, Yang K, Liu Z: **Emerging nanotechnology and advanced materials for cancer radiation therapy**. *Advanced materials* 2017, **29**(32):1700996.

5. Wang C, Dong Z, Hao Y, Zhu Y, Ni J, Li Q, Liu B, Han Y, Yang Z, Wan J: **Coordination Polymer-Coated CaCO3 Reinforces Radiotherapy by Reprogramming the Immunosuppressive Metabolic Microenvironment**. *Advanced Materials* 2022, **34**(3):2106520.

6. Khalil DN, Smith EL, Brentjens RJ, Wolchok JD: **The future of cancer treatment: immunomodulation, CARs and combination immunotherapy**. *Nature reviews Clinical oncology* 2016, **13**(5):273-290.

7. Dewan MZ, Galloway AE, Kawashima N, Dewyngaert JK, Babb JS, Formenti SC, Demaria S: **Fractionated but Not Single-Dose Radiotherapy Induces an**

Immune-Mediated Abscopal Effect when Combined with Anti–CTLA-4 AntibodyFractionated Radiation Synergizes with Immunotherapy. *Clinical Cancer Research* 2009, **15**(17):5379-5388.

8. Dovedi SJ, Cheadle EJ, Popple AL, Poon E, Morrow M, Stewart R, Yusko EC, Sanders CM, Vignali M, Emerson RO: **Fractionated Radiation Therapy Stimulates Antitumor Immunity Mediated by Both Resident and Infiltrating Polyclonal T-cell Populations when Combined with PD-1 BlockadeFractionated RT Modulates the Local TCR Repertoire**. *Clinical Cancer Research* 2017, **23**(18):5514-5526.

9. Yamazaki T, Kirchmair A, Sato A, Buque A, Rybstein M, Petroni G, Bloy N, Finotello F, Stafford L, Navarro Manzano E: **Mitochondrial DNA drives abscopal responses to radiation that are inhibited by autophagy**. *Nature Immunology* 2020, **21**(10):1160-1171.

10. White MJ, McArthur K, Metcalf D, Lane RM, Cambier JC, Herold MJ, Van Delft MF, Bedoui S, Lessene G, Ritchie ME: **Apoptotic caspases suppress mtDNA-induced STING-mediated type I IFN production**. *Cell* 2014, **159**(7):1549-1562.

11. Ahn J, Xia T, Capote AR, Betancourt D, Barber GN: **Extrinsic phagocyte-dependent STING signaling dictates the immunogenicity of dying cells**. *Cancer cell* 2018, **33**(5):862-873. e865.

12. Swartz MA, Iida N, Roberts EW, Sangaletti S, Wong MH, Yull FE, Coussens

LM, DeClerck YA: **Tumor Microenvironment Complexity: Emerging Roles in Cancer TherapyTumor Microenvironment**. *Cancer research* 2012, **72**(10):2473-2480.

13. Sies H: **Hydrogen peroxide as a central redox signaling molecule in physiological oxidative stress: Oxidative eustress**. *Redox biology* 2017, **11**:613-619.

14. Liang K, Sun H, Yang Z, Yu H, Shen J, Wang X, Chen H: **Breaking the Redox Homeostasis: an Albumin-Based Multifunctional Nanoagent for GSH Depletion-Assisted Chemo-/Chemodynamic Combination Therapy**. *Advanced Functional Materials* 2021, **31**(22):2100355.

15. Brizel DM, Sibley GS, Prosnitz LR, Scher RL, Dewhirst MW: **Tumor hypoxia adversely affects the prognosis of carcinoma of the head and neck**. *International Journal of Radiation Oncology* Biology* Physics* 1997, **38**(2):285-289.

16. Van Den Beucken T, Koch E, Chu K, Rupaimoole R, Prickaerts P, Adriaens M, Voncken JW, Harris AL, Buffa FM, Haider S: **Hypoxia promotes stem cell phenotypes and poor prognosis through epigenetic regulation of DICER**. *Nature communications* 2014, **5**(1):1-13.

17. Al-Assar O, Demiciorglu F, Lunardi S, Gaspar-Carvalho MM, McKenna WG, Muschel RM, Brunner TB: **Contextual regulation of pancreatic cancer stem cell phenotype and radioresistance by pancreatic stellate cells**. *Radiotherapy*

and Oncology 2014, **111**(2):243-251.

18. Gray LH, Conger AD, Ebert M, Hornsey S, Scott O: **The concentration of oxygen dissolved in tissues at the time of irradiation as a factor in radiotherapy**. *The British journal of radiology* 1953, **26**(312):638-648.

19. Chiu DK-C, Tse AP-W, Xu IM-J, Di Cui J, Lai RK-H, Li LL, Koh H-Y, Tsang FH-C, Wei LL, Wong C-M: **Hypoxia inducible factor HIF-1 promotes myeloid-derived suppressor cells accumulation through ENTPD2/CD39L1 in hepatocellular carcinoma**. *Nature communications* 2017, **8**(1):1-12.

20. Li Y, Patel SP, Roszik J, Qin Y: **Hypoxia-driven immunosuppressive metabolites in the tumor microenvironment: new approaches for combinational immunotherapy**. *Frontiers in immunology* 2018, **9**:1591.

21. Gong F, Yang N, Wang X, Zhao Q, Chen Q, Liu Z, Cheng L: **Tumor microenvironment-responsive intelligent nanoplatforms for cancer theranostics**. *Nano Today* 2020, **32**:100851.

22. Peng J, Yang Q, Shi K, Xiao Y, Wei X, Qian Z: **Intratumoral fate of functional nanoparticles in response to microenvironment factor: Implications on cancer diagnosis and therapy**. *Advanced Drug Delivery Reviews* 2019, **143**:37-67.

23. Gong F, Cheng L, Yang N, Betzer O, Feng L, Zhou Q, Li Y, Chen R, Popovtzer R, Liu Z: **Ultrasmall oxygen-deficient bimetallic oxide MnWOX nanoparticles for depletion of endogenous GSH and enhanced**

sonodynamic cancer therapy. *Advanced Materials* 2019, **31**(23):1900730.

24. Wang H, Zhu W, Feng L, Chen Q, Chao Y, Dong Z, Liu Z: **Nanoscale covalent organic polymers as a biodegradable nanomedicine for chemotherapy-enhanced photodynamic therapy of cancer**. *Nano Research* 2018, **11**(6):3244-3257.

25. Zhang C, Bu W, Ni D, Zhang S, Li Q, Yao Z, Zhang J, Yao H, Wang Z, Shi J: **Synthesis of iron nanometallic glasses and their application in cancer therapy by a localized Fenton reaction**. *Angewandte Chemie* 2016, **128**(6):2141-2146.

26. Yang B, Ding L, Yao H, Chen Y, Shi J: **A Metal-Organic Framework (MOF) Fenton Nanoagent-Enabled Nanocatalytic Cancer Therapy in Synergy with Autophagy Inhibition**. *Advanced materials* 2020, **32**(12):1907152.

27. Zhu Y, Wang W, Cheng J, Qu Y, Dai Y, Liu M, Yu J, Wang C, Wang H, Wang S: **Stimuli-Responsive Manganese Single-Atom Nanozyme for Tumor Therapy via Integrated Cascade Reactions**. *Angewandte Chemie International Edition* 2021, **60**(17):9480-9488.

28. Horning KJ, Caito SW, Tipps KG, Bowman AB, Aschner M: **Manganese is essential for neuronal health**. *Annual review of nutrition* 2015, **35**:71.

29. Waldron KJ, Rutherford JC, Ford D, Robinson NJ: **Metalloproteins and metal sensing**. *Nature* 2009, **460**(7257):823-830.

30. Zhu W, Dong Z, Fu T, Liu J, Chen Q, Li Y, Zhu R, Xu L, Liu Z: **Modulation of**

hypoxia in solid tumor microenvironment with MnO2 nanoparticles to enhance photodynamic therapy. *Advanced Functional Materials* 2016, **26**(30):5490-5498.

31. Chen Q, Feng L, Liu J, Zhu W, Dong Z, Wu Y, Liu Z: **Intelligent albumin–MnO2 nanoparticles as pH-/H2O2-responsive dissociable nanocarriers to modulate tumor hypoxia for effective combination therapy**. *Advanced materials* 2016, **28**(33):7129-7136.

32. Fan H, Yan G, Zhao Z, Hu X, Zhang W, Liu H, Fu X, Fu T, Zhang XB, Tan W: **Inside Back Cover: A Smart Photosensitizer–Manganese Dioxide Nanosystem for Enhanced Photodynamic Therapy by Reducing Glutathione Levels in Cancer Cells (Angew. Chem. Int. Ed. 18/2016)**. *Angewandte Chemie International Edition* 2016, **55**(18):5611-5611.

33. Prasad P, Gordijo CR, Abbasi AZ, Maeda A, Ip A, Rauth AM, DaCosta RS, Wu XY: **Multifunctional albumin–MnO2 nanoparticles modulate solid tumor microenvironment by attenuating hypoxia, acidosis, vascular endothelial growth factor and enhance radiation response**. *ACS nano* 2014, **8**(4):3202-3212.

34. Lv M, Chen M, Zhang R, Zhang W, Wang C, Zhang Y, Wei X, Guan Y, Liu J, Feng K: **Manganese is critical for antitumor immune responses via cGAS-STING and improves the efficacy of clinical immunotherapy**. *Cell research* 2020, **30**(11):966-979.

35. Wang C, Sun Z, Zhao C, Zhang Z, Wang H, Liu Y, Guo Y, Zhang B, Gu L, Yu Y: **Maintaining manganese in tumor to activate cGAS-STING pathway evokes a robust abscopal anti-tumor effect**. *Journal of Controlled Release* 2021, **331**:480-490.

36. Wang C, Guan Y, Lv M, Zhang R, Guo Z, Wei X, Du X, Yang J, Li T, Wan Y: **Manganese increases the sensitivity of the cGAS-STING pathway for double-stranded DNA and is required for the host defense against DNA viruses**. *Immunity* 2018, **48**(4):675-687. e677.

37. Song Y, Liu Y, Teo HY, Hanafi ZB, Mei Y, Zhu Y, Chua YL, Lv M, Jiang Z, Liu H: **Manganese enhances the antitumor function of CD8+ T cells by inducing type I interferon production**. *Cellular & Molecular Immunology* 2021, **18**(6):1571-1574.

38. Hou L, Tian C, Yan Y, Zhang L, Zhang H, Zhang Z: **Manganese-based nanoactivator optimizes cancer immunotherapy via enhancing innate immunity**. *ACS nano* 2020, **14**(4):3927-3940.

39. Deng L, Liang H, Xu M, Yang X, Burnette B, Arina A, Li X-D, Mauceri H, Beckett M, Darga T: **STING-dependent cytosolic DNA sensing promotes radiation-induced type I interferon-dependent antitumor immunity in immunogenic tumors**. *Immunity* 2014, **41**(5):843-852.

40. Woo S-R, Fuertes MB, Corrales L, Spranger S, Furdyna MJ, Leung MY, Duggan R, Wang Y, Barber GN, Fitzgerald KA: **STING-dependent cytosolic**

DNA sensing mediates innate immune recognition of immunogenic tumors. *Immunity* 2014, **41**(5):830-842.

41. Li X, Wang X, Ito A: **Tailoring inorganic nanoadjuvants towards next-generation vaccines**. *Chemical Society Reviews* 2018, **47**(13):4954-4980.

42. Wang X, Li X, Ito A, Sogo Y, Ohno T: **Particle-size-dependent toxicity and immunogenic activity of mesoporous silica-based adjuvants for tumor immunotherapy**. *Acta biomaterialia* 2013, **9**(7):7480-7489.

43. Wang X, Li X, Ito A, Sogo Y, Ohno T: **Pore size-dependent immunogenic activity of mesoporous silica-based adjuvants in cancer immunotherapy**. *Journal of Biomedical Materials Research Part A: An Official Journal of The Society for Biomaterials, The Japanese Society for Biomaterials, and The Australian Society for Biomaterials and the Korean Society for Biomaterials* 2014, **102**(4):967-974.

44. Wang X, Li X, Yoshiyuki K, Watanabe Y, Sogo Y, Ohno T, Tsuji NM, Ito A: **Comprehensive Mechanism Analysis of Mesoporous-Silica-Nanoparticle-Induced Cancer Immunotherapy**. *Advanced healthcare materials* 2016, **5**(10):1169-1176.

45. Wang X, Li X, Ito A, Watanabe Y, Sogo Y, Tsuji NM, Ohno T: **Stimulation of in vivo antitumor immunity with hollow mesoporous silica nanospheres**. *Angewandte Chemie* 2016, **128**(5):1931-1935.

46. Wang X, Li X, Ito A, Yoshiyuki K, Sogo Y, Watanabe Y, Yamazaki A, Ohno T,

Tsuji NM: **Hollow structure improved anti-cancer immunity of mesoporous silica nanospheres in vivo**. *Small* 2016, **12**(26):3510-3515.

47. Wang X, Li X, Ito A, Sogo Y, Watanabe Y, Tsuji NM, Ohno T: **Biodegradable metal ion-doped mesoporous silica nanospheres stimulate anticancer Th1 immune response in vivo**. *ACS applied materials & interfaces* 2017, **9**(50):43538-43544.

48. Wang X, Li X, Ito A, Sogo Y, Watanabe Y, Hashimoto K, Yamazaki A, Ohno T, Tsuji NM: **Synergistic effects of stellated fibrous mesoporous silica and synthetic dsRNA analogues for cancer immunotherapy**. *Chemical Communications* 2018, **54**(9):1057-1060.

49. Wang X, Ihara S, Li X, Ito A, Sogo Y, Watanabe Y, Tsuji NM, Yamazaki A: **Si-doping increases the adjuvant activity of hydroxyapatite nanorods**. *Colloids and Surfaces B: Biointerfaces* 2019, **174**:300-307.

50. Zou Z, He X, He D, Wang K, Qing Z, Yang X, Wen L, Xiong J, Li L, Cai L: **Programmed packaging of mesoporous silica nanocarriers for matrix metalloprotease 2-triggered tumor targeting and release**. *Biomaterials* 2015, **58**:35-45.

51. Lin LS, Song J, Song L, Ke K, Liu Y, Zhou Z, Shen Z, Li J, Yang Z, Tang W: **Simultaneous Fenton-like ion delivery and glutathione depletion by MnO2-based nanoagent to enhance chemodynamic therapy**. *Angewandte Chemie* 2018, **130**(18):4996-5000.

52. Wang J-G, Yang Y, Huang Z-H, Kang F: **A high-performance asymmetric supercapacitor based on carbon and carbon–MnO2 nanofiber electrodes**. *Carbon* 2013, **61**:190-199.

53. Huang J, Huang Y, Xue Z, Zeng S: **Tumor microenvironment responsive hollow mesoporous Co9S8@ MnO2-ICG/DOX intelligent nanoplatform for synergistically enhanced tumor multimodal therapy**. *Biomaterials* 2020, **262**:120346.

54. Wen J, Yang K, Sun S: **MnO 2-Based nanosystems for cancer therapy**. *Chemical Communications* 2020, **56**(52):7065-7079.

55. Rice-Evans C, Halliwell B, Lunt G, Davies KJ: **Oxidative stress: the paradox of aerobic life**. In: *Biochemical Society Symposia: 1995*: Portland Press; 1995: 1-31.

56. Nicco C, Batteux F: **ROS modulator molecules with therapeutic potential in cancers treatments**. *Molecules* 2017, **23**(1):84.

57. Bigley R, Riddle M, Layman D, Stankova L: **Human cell dehydroascorbate reductase. Kinetic and functional properties**. *Biochimica et Biophysica Acta (BBA)-Enzymology* 1981, **659**(1):15-22.

58. Martensson J, Meister A, Mrtensson J: **Glutathione deficiency decreases tissue ascorbate levels in newborn rats: ascorbate spares glutathione and protects**. *Proceedings of the National Academy of Sciences* 1991, **88**(11):4656-4660.

59. Bansal A, Simon MC: **Glutathione metabolism in cancer progression and treatment resistance**. *Journal of Cell Biology* 2018, **217**(7):2291-2298.

60. Xu B, Cui Y, Wang W, Li S, Lyu C, Wang S, Bao W, Wang H, Qin M, Liu Z: **Immunomodulation-enhanced nanozyme-based tumor catalytic therapy**. *Advanced Materials* 2020, **32**(33):2003563.

61. Dinarello CA: **Interleukin-1**. *Cytokine & growth factor reviews* 1997, **8**(4):253-265.

62. Holbrook J, Lara-Reyna S, Jarosz-Griffiths H, McDermott MF: **Tumour necrosis factor signalling in health and disease**. *F1000Research* 2019, **8**(111):111.

63. Rincón M, Anguita J, Nakamura T, Fikrig E, Flavell RA: **Interleukin (IL)-6 directs the differentiation of IL-4–producing CD4+ T cells**. *The Journal of experimental medicine* 1997, **185**(3):461-470.

64. Locksley RM, Killeen N, Lenardo MJ: **The TNF and TNF receptor superfamilies: integrating mammalian biology**. *Cell* 2001, **104**(4):487-501.

65. Sallusto F, Cella M, Danieli C, Lanzavecchia A: **Dendritic cells use macropinocytosis and the mannose receptor to concentrate macromolecules in the major histocompatibility complex class II compartment: downregulation by cytokines and bacterial products**. *The Journal of experimental medicine* 1995, **182**(2):389-400.

66. Formenti SC, Rudqvist N-P, Golden E, Cooper B, Wennerberg E, Lhuillier C,

Vanpouille-Box C, Friedman K, Ferrari de Andrade L, Wucherpfennig KW: **Radiotherapy induces responses of lung cancer to CTLA-4 blockade**. *Nature medicine* 2018, **24**(12):1845-1851.

67. Parkes EE, Walker SM, Taggart LE, McCabe N, Knight LA, Wilkinson R, McCloskey KD, Buckley NE, Savage KI, Salto-Tellez M: **Activation of STING-dependent innate immune signaling by S-phase-specific DNA damage in breast cancer**. *Journal of the National Cancer Institute* 2017, **109**(1):djw199.

68. Ding L, Kim H-J, Wang Q, Kearns M, Jiang T, Ohlson CE, Li BB, Xie S, Liu JF, Stover EH: **PARP inhibition elicits STING-dependent antitumor immunity in Brca1-deficient ovarian cancer**. *Cell reports* 2018, **25**(11):2972-2980. e2975.

69. Pantelidou C, Sonzogni O, De Oliveria Taveira M, Mehta AK, Kothari A, Wang D, Visal T, Li MK, Pinto J, Castrillon JA: **PARP Inhibitor Efficacy Depends on CD8+ T-cell Recruitment via Intratumoral STING Pathway Activation in BRCA-Deficient Models of Triple-Negative Breast CancerPARP Inhibition Induces STING-Mediated T-cell Recruitment**. *Cancer discovery* 2019, **9**(6):722-737.

70. Sen T, Rodriguez BL, Chen L, Corte CMD, Morikawa N, Fujimoto J, Cristea S, Nguyen T, Diao L, Li L: **Targeting DNA Damage Response Promotes Antitumor Immunity through STING-Mediated T-cell Activation in Small**

Cell Lung CancerDDR Inhibition Enhances Antitumor Immunity in SCLC. *Cancer discovery* 2019, **9**(5):646-661.

71. Shen J, Zhao W, Ju Z, Wang L, Peng Y, Labrie M, Yap TA, Mills GB, Peng G: **PARPi Triggers the STING-Dependent Immune Response and Enhances the Therapeutic Efficacy of Immune Checkpoint Blockade Independent of BRCAnessPARP1 Inhibitors Trigger Antitumor Immunity**. *Cancer research* 2019, **79**(2):311-319.

72. Chabanon RM, Muirhead G, Krastev DB, Adam J, Morel D, Garrido M, Lamb A, Hénon C, Dorvault N, Rouanne M: **PARP inhibition enhances tumor cell–intrinsic immunity in ERCC1-deficient non–small cell lung cancer**. *The Journal of clinical investigation* 2019, **129**(3):1211-1228.

73. Sun L, Wu J, Du F, Chen X, Chen ZJ: **Cyclic GMP-AMP synthase is a cytosolic DNA sensor that activates the type I interferon pathway**. *Science* 2013, **339**(6121):786-791.

74. Murphy DA, Cheng H, Yang T, Yan X, Adjei IM: **Reversing hypoxia with PLGA-encapsulated manganese dioxide nanoparticles improves natural killer cell response to tumor spheroids**. *Molecular Pharmaceutics* 2021, **18**(8):2935-2946.

75. Lucarelli M, Gatti AM, Savarino G, Quattroni P, Martinelli L, Monari E, Boraschi D: **Innate defence functions of macrophages can be biased by nano-sized ceramic and metallic particles**. *European cytokine network* 2004,

15(4):339-346.

76. Kawasaki H: **A mechanistic review of silica-induced inhalation toxicity**. *Inhalation toxicology* 2015, **27**(8):363-377.

77. Winter M, Beer H-D, Hornung V, Krämer U, Schins RP, Förster I: **Activation of the inflammasome by amorphous silica and TiO2 nanoparticles in murine dendritic cells**. *Nanotoxicology* 2011, **5**(3):326-340.

Chapter 3 Chemo-immunotherapy enhanced by MM NPs

3.1 Introduction

Although chemotherapy has been widely utilized in clinical practice, its efficiency is still limited by many factors, including the complex TME, which is characterized by elevated H_2O_2 levels, hypoxia, acidic pH, and strong antioxidative systems [1-3]. The hypoxic TME can induce drug resistance and suppress the efficiency of chemotherapy [4, 5]. Immunotherapy, which emerged in recent years, has revolutionized cancer treatments, modulating the functions of specific immune cells to improve the efficiency of many cancer treatments [6-8]. One of the promising immunotherapy strategies is checkpoint blockade therapy, including anti-CTLA-4, anti-PD 1 and anti-PD-L1, which have been approved by the FDA for the clinical anticancer therapies recently [9, 10]. Moreover, chemo-immunotherapy has displayed the potential to maximize the anticancer efficiency [11, 12]. Except for the notable potential of chemo-immunotherapy, there are still remaining challenges for clinical translation. For example, the hypoxia in the TME can induce resistance to chemotherapy and form an immunosuppressive TME, thus limiting the efficiency of chemo-immunotherapy [13-15]. Interestingly, MSNs not only have shown advantages in chemotherapy owing to their facile synthesis and functionalization, high pore volume and surface area, controllable pore size and morphology, as well as good physicochemical stability and biocompatibility [16] but also have shown the capacity of immune activation as shown

in previous studies [17-24]. The mesoporous structure of MSNs contributes to the high specific surface area and pore volume, which is beneficial for drug loading. Moreover, due to their facile functionalization and controllable shape, size, and pore structures, MSNs can be utilized to load a series of drugs and manipulate the drug loading efficiency, including chemical drugs, proteins, and genetic molecules [25] but cannot regulate the TME, a factor that alters the cancer therapeutic efficiency. Moreover, owing to the stable Si-O-Si framework of MSNs, its degradation speed is relatively low [26]. Metal ion-doping has been proved to effectively weaken the Si-O-Si framework and promote the degradation of MSNs in our group's previous research studies [23]. In recent years, manganese (Mn)-based nanomaterials have shown potential in anticancer applications owing to their special functions for the regulation of the TME by inducing an increase in the concentration of O_2 and ROS, and the depletion of GSH [27-30]. GSH is one of the most abundant components in strong antioxidative systems, which consumes ROS to decrease the efficiency of ROS-based anticancer therapies [31, 32]. Moreover, Mn ions have shown a regulatory function for the immune responses through the activation of the cyclic GMP-AMP (cGAMP) synthase-a stimulator of the interferon gene (cGAS/STING) pathway, thus inducing the secretion of type I interferons (IFNs) and cytokines [33, 34], whereas the applications of Mn-doped MSNs with regulatory functions for the TME and immune responses to chemo-immunotherapy and simultaneously inhibit tumor growth and tumor metastasis are still rare. In this work, Mn-based nanomaterials were adopted to regulate the TME and

improve the degradation of MSNs, thus enhancing the efficiency of chemo-immunotherapy, as shown in Scheme 1. MM NPs were synthesized by introducing $KMnO_4$ during the synthesis process of MSNs. The amount of Mn doped into MSNs was adjusted by adjusting the concentration of $KMnO_4$ added during the synthesis process. Mn-doping endowed MSNs with six new TME regulatory functions, including GSH depletion, ROS generation, oxygenation, cell-killing effect, immune activation, and degradation promotion. Notably, in a bilateral animal model for synergistic chemoimmunotherapy, the combination of MM NPs, DOX, and the anti-CTLA-4 antibody showed an obvious inhibitory effect on the growth of primary tumors and distant untreated tumors. Therefore, it was considered that MM NPs with TME regulatory functions may provide a strategy for chemo-immunotherapy to inhibit both tumor growth and tumor metastasis.

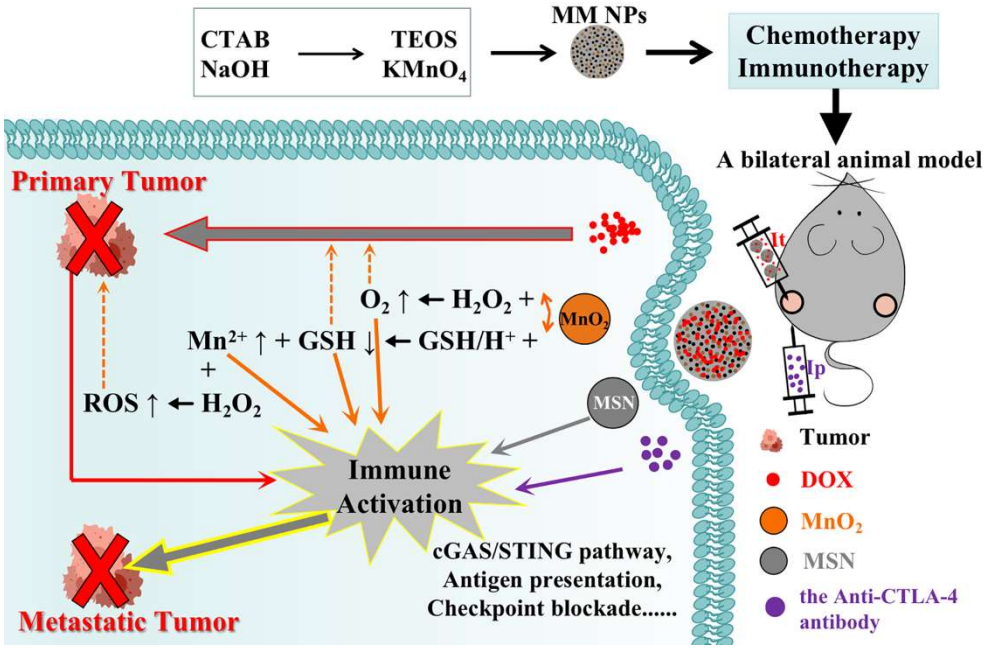

Scheme 3-1 Schematic illustration of MM NP synthesis and the synergistic efficiency of chemo-immunotherapy by MM NPs. (It: intratumor injection; Ip: intraperitoneal injection)

3.2 Materials and method

3.2.1 Materials

Tetraethyl orthosilicate (TEOS), hexadecyltrimethylammonium bromide (CTAB), potassium permanganate ($KMnO_4$), and doxorubicin hydrochloride (DOX) were bought from Wako Chemical Co., Ltd. Sodium hydroxide solution (NaOH, 5 mol L^{-1}) was bought from Nacalai Tesque Inc. Methylene blue (MB) and hydrogen peroxide (H_2O_2, 30%) were bought from FUJIFILM Wako Pure Chemicals Co. Glutathione in reduced form (GSH), and 5,5' -dithiobis (2-nitrobenzoic acid) (DTNB) were bought from Tokyo Chemical Industry Co., Ltd. The anti-CTLA-4 antibody (9D9; Cat. #BE0164) was bought from BioXcell.

3.2.2 Synthesis of Mn-doped MSNs

A total of 480 mL of ultrapure water containing 1 g of CTAB and 1.4 mL of NaOH (5 M) was stirred in a water bath (70 ^oC) for 1h. Then 5 mL of TEOS and 2 mL of $KMnO_4$ solution of different concentrations (Table 3-1) were added sequentially and stirred for 5h in the water bath. The obtained solution was centrifuged, and the precipitant was washed three times with ultrapure water and once with ethanol. NPs were obtained by drying the precipitant at 60 ^oC for 8 h followed by heating at 600 ^oC for 5h, which were named MSNs, MM1, and MM2, respectively.

Table 3-1 The concentration of KMnO4 added during the synthesis process

	MSNs	MM1	MM2
$KMnO_4$ (g mL^{-1})	0	0.08	0.1

For use in intracellular and in vivo experiments, the obtained NPs were sterilized by heating at 160 ºC for 3h using a drying sterilizer (SG 600, Yamato Scientific, Japan).

3.2.3 Characterization of NPs

The morphology of the NPs coated with platinum was observed by field emission scanning electron microscopy (FE-SEM, HITACHI, Japan) and field emission transmission electron microscopy (TEM-EDS, JEOL, Japan). The Si/Mn ratio and phase of the NPs were measured by inductively coupled plasma atomic emission spectroscopy (ICP-AES, SPS7800, Seiko Instruments, Japan) and X-ray diffractometry (XRD, RINT 2550, Rigaku, Japan), respectively. The chemical composition of the NPs was determined by X-ray photoelectron spectroscopy (XPS, PHI 5000 VersaProbe III, ULVAC-PHI, Japan). The zeta potential of the NPs dispersed in different buffer solutions was measured using the zeta-potential and particle size analyzer (ELSZ-1000, Otsuka Electronics, Japan). The surface area and pore size distribution were analyzed using a surface area and porosity analyzer (Micromeritics Tristar II 3020, Shimadzu, Japan) at 196 ºC. Buffer solution at pH 7.4 [PBS (-)] was prepared by dissolving PBS powders (4.80 g) (Dulbecco's PBS, Nissui Pharmaceutical, Japan) in ultrapure water

(500 mL). Buffer solution at pH 5 (Acetic acid buffer) was prepared by dissolving sodium acetate (3.014 g) (Wako, Japan) and acetic acid (1.17 mL) (Wako, Japan) in ultrapure water (500 mL).

3.2.4 DOX loading efficiency of NPs

DOX (2 mg mL^{-1}) and NPs (2 mg mL^{-1}) in PBS(-) were mixed with a volume ratio of 1 : 1. Then the mixed solution was shaken at a speed of 1000 rpm for 24 h. The DOX loading efficiency is defined as follows:

DOX loading efficiency (%) = 100 x (Amount of DOX added - Amount of DOX in the supernatant) / (Amount of DOX added).

3.2.5 Regulation functions to TME

3.2.5.1 GSH depletion induced by MM

GSH depletion induced by NPs was investigated using DTNB. The relative GSH level was detected as the generated TNB concentration [35], which was converted from DTNB by GSH. GSH (2 mM) and NPs (1 mg mL^{-1}) were mixed in acetic acid buffer solution and cultured at 37 ^{o}C. After 1 h and 2 h, the mixed solutions were centrifuged at 10 000 rpm for 1 min. Then, the supernatants were mixed with DTNB (0.1 mg mL^{-1}) and reacted for 10 min. The solution absorbance of TNB at 415 nm was measured after being diluted to 2 mL using an ultraviolet-visible (UV-vis) absorption spectrometer (V-730, JASCO, Japan). The concentration of Mn generated after reaction between NPs and GSH was confirmed by ICP-AES analysis. NPs (1 mg mL^{-1}) were

mixed with GSH (10 mM)-PBS (-) solution and reacted for 2h. Then, the NPs-GSH-PBS (-) solution was centrifuged (10 000 rpm for 10 min) and the supernatant was collected for further ICP-AES analysis.

3.2.5.2 ROS generation induced by NPs

The ROS generation in aqueous solutions induced by NPs was analyzed in accordance with a previously published method [36]. In particular, NPs (20 mg mL^{-1}) were dispersed in 25 mM $NaHCO_3$ solution containing H_2O_2 (10 mM) and methylene blue (MB) (10 mg mL^{-1}), followed by incubation at 37 ºC. The absorbance of MB at 664 nm was measured at determined time points using a UV-vis absorption spectrometer.

The ROS generation in cancer cells induced by NPs was analyzed with a DCFDA/H2DCFDA - cellular ROS assay kit (Abcam, USA). Precultured Lewis lung carcinoma (LLC) cells (2.5 x 10^5 cells mL^{-1}) were washed with PBS (-) once and cultured with NPs (20 mg mL^{-1}) for 6 h. Then, DCFDA (30 mM) was added, and the cells were cultured for another 45 min. Finally, the fluorescence of DCF (Ex/Em = 492 nm/530 nm) was measured using a microplate reader.

3.2.5.3 Oxygenation induced by NPs

The oxygenation induced by NPs was analyzed using an O_2 probe $[Ru(dpp)_3]Cl_2$ (RDPP, Santa Cruz Biotechnology, USA). NPs of different concentrations were dispersed in PBS (-) solution containing RDPP (3 mM). Then, H_2O_2 (50 mM) was

added. At determined time points, the fluorescence of RDPP (Ex/Em = 450 nm/630 nm) was measured using a microplate reader.

3.2.5.4 Cell-killing effect induced by NPs

The NP uptake by LLC cells was tested by confocal laser scanning microscopy (CLSM, Leica Confocal IP/FCS, German). Rhodamine B-conjugated NPs were prepared to track the location of the NPs. NPs, rhodamine B, and 3-triethoxysilylpropylamine (APTES, Aldrich) were mixed in anhydrous ethanol. After 48 h of stirring at room temperature, the mixed solution was centrifuged at 10 000 rpm for 5 min and washed with ethanol. After drying the obtained precipitant at room temperature, rhodamine B-conjugated NPs (NPs-RhB) were obtained. The NPs-RhB were used to culture with LLC cells (2 x 10^5 cells mL^{-1}) in a glass bottom plate overnight. Then, the cells were cultured with LysoTracker Green (50 nM) at 37 ^oC for 2h. After washing with the medium containing 90 vol% low-glucose Dulbecco's modified Eagle's medium (L-DMEM, Wako, Japan) and 10 vol% fetal bovine serum (FBS, Invitrogen, USA), the cells were further cultured with Hoechst (2.5 mg mL^{-1}) at 37 ^oC for 10 min. After being washed with PBS (-), the antifade reagent was added and cultured for 15 min on ice followed by observation of fluorescence using a confocal laser scanning microscope.

The cytotoxicity of the NPs was determined through the culture of LLC cells with NPs of different concentrations. LLC cells (4 x 10^4 cells mL^{-1}) were seeded in a 96-well plate and cultured overnight before being cultured with NPs. After being cultured

with NPs for 24h, the cell viability was measured using the cell counting kit-8 (CCK-8) assay.

3.2.5.5 Immune activation induced by NPs

The immunogenic activity of the NPs was analyzed by measuring the amount of tumor necrosis factor-a (TNF-a) secreted by macrophage-like cells co-cultured with NPs. First, human monocytic leukemia cells (THP-1: Riken BioResource Research Center, Japan) were cultured in a conditioned medium made up of 90 vol% RPMI 1640 (Invitrogen, USA), 10 vol% FBS and 0.5 mM phorbol 12-myristate 13-acetate (PMA, Sigma, USA) for 3 h, and the macrophage-like cells were obtained. Then, the obtained macrophage-like cells (2 x 10^6 cells mL^{-1}) were cultured overnight before being cultured with NPs (30 mg mL^{-1}). After culturing macrophage-like cells with NPs for 1d, the amount of TNF-a was measured using human-TNF-a kits (BD Biosciences, USA) in accordance with the manufacturer's instructions.

3.2.5.6 In vitro degradation

The in vitro degradation performance of the NPs was investigated by measuring the Si and Mn concentration after incubation in different solutions at determined timepoints. NPs were dispersed in $NaHCO_3$ solution (25 mM, 37 ºC) and $NaHCO_3$ solution (25 mM, 37 ºC) containing GSH (10 mM), respectively. At determined time points, the solution was centrifuged at 10 000 rpm for 10 min, the obtained supernatant was collected, and 1 mL of fresh solution was added. Finally, the concentration of Si and

Mn in the supernatant collected was measured by ICP-AES analysis. And the degradation of MSNs and MM NPs that are dispersed in $NaHCO_3$ solution containing GSH for 1d and 5d was further observed by TEM.

3.2.6 In vivo synergistic anticancer effect of NPs-enhanced chemo-immunotherapy in combination with the anti-CTLA-4 antibody

The animal experiments were approved by the Ethical Committee of the National Institute of Advanced Industrial Science and Technology (AIST). All of the animal experiments and feeding were carried out in accordance with the guidelines of the Ethical Committee of AIST, Japan.

Mice (C57BL/6JJcl, female, 7 weeks old, CLEA Inc., Japan) were randomly divided into six groups (n = 5). On day 0, the mice were subcutaneously injected with live LLC cells into the left flanks at a concentration of 5 x 10^5 cells per mouse to simulate the primary tumors. On days 6, 8, 10, 13, and 15, the mice were treated as follows. The mice in group 1 were treated with an intratumor injection of saline (100 mL). The mice in group 2 were treated with an intratumor injection of DOX (1 mg mL^{-1}) in 100 mL of saline. The mice in group 3 were treated with an intratumor injection of DOX (1 mg mL^{-1}) in 100 mL of saline and an intraperitoneal injection of the anti-CTLA-4 antibody (2 mg mL^{-1}) in 100 mL of saline. The mice in group 4 were treated with an intratumor injection of DOX (1 mg mL^{-1}) – MSNs (10 mg mL^{-1}) in 100 mL of saline and an intraperitoneal injection of the anti-CTLA-4 antibody (2 mg mL^{-1}) in 100 mL of saline. The mice in group 5 were treated with an intratumor injection of DOX (1 mg mL^{-1}) –

MM1 (10 mg mL^{-1}) in 100 mL of saline and an intraperitoneal injection of the anti-CTLA-4 antibody (2 mg mL^{-1}) in 100 mL of saline. The mice in group 6 were treated with an intratumor injection of DOX (1 mg mL^{-1}) – MM2 (10 mg mL^{-1}) in 100 mL of saline and an intraperitoneal injection of the anti-CTLA-4 antibody (2 mg $mL1^{-1}$) in 100 mL of saline. On day 16, the mice were subcutaneously injected with live LLC cells into the right flanks at a concentration of 1 x 105 cells per mouse to simulate the metastatic tumors. The tumor diameters on both flanks were measured using a caliper at determined time points.

The spleens were collected and digested for cytokine analysis at the endpoint. Then, the amounts of cytokines secreted were measured using mouse interferon-γ (IFN- γ) and interleukin-6 (IL-6) kits (BD Biosciences, USA) in accordance with the manufacturer's instructions.

3.3 Results

3.3.1 Characterization of NPs

As shown in Figure 3-1, MSNs, MM1, and MM2 showed similar morphologies. As shown in Figure 3-2 and Table 3-2, the Mn-doping induced a slight decrease in the specific surface area and a slight increase in the pore size. MSNs, MM1, and MM2 showed a specific surface area of 910.6 m^2 g^{-1}, 877.2 m^2 g^{-1}, and 845.9 m^2 g^{-1}, respectively. MSNs, MM1, and MM2 showed a pore size of 3.7 nm, 3.9 nm, and 4.1

nm, respectively. And MSNs, MM1, and MM2 showed a pore volume of 0.8 cm^3 g^{-1}, 0.9 cm^3 g^{-1}, and 0.9 cm^3 g^{-1}, respectively.

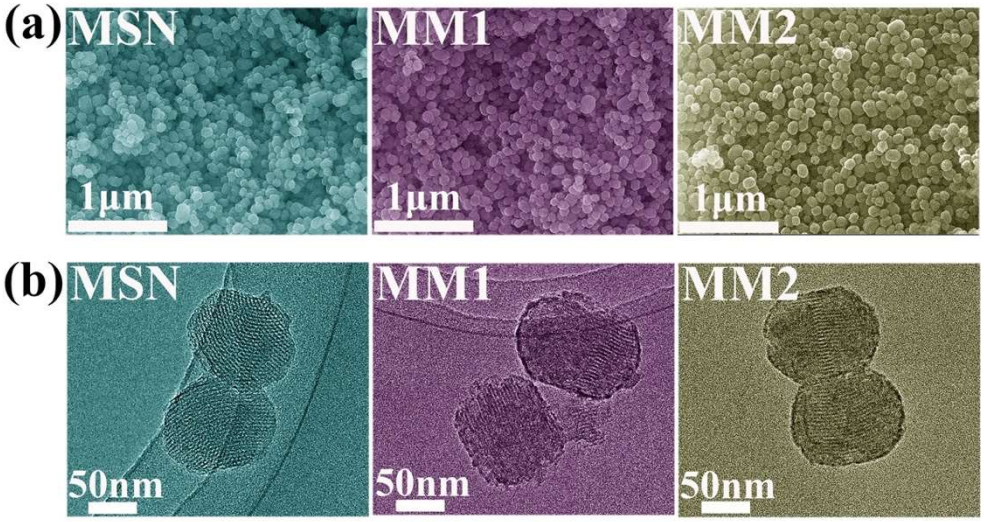

Figure 3-1 Morphology of different NPs. (a) SEM images; (b) TEM images.

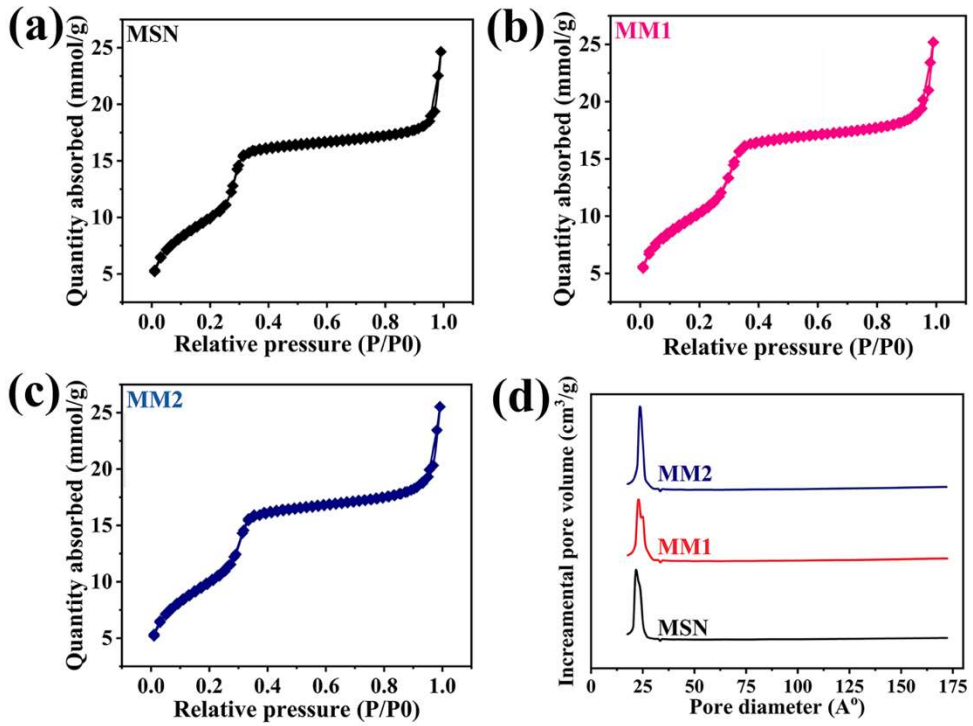

Figure 3-2 Analysis of specific surface area (a) N_2 adsorption–desorption isotherms of MSNs; (b) N_2 adsorption–desorption isotherms of MM1; (c) N_2 adsorption–desorption isotherms of MM2; (d) pore size distribution of the NPs.

Table 3-2 Surface areas, pore sizes, and pore volumes of MSNs, MM1, and MM2

NPs	MSNs	MM1	MM2
Surface area (m^2 g^{-1})	910.6	877.2	845.9
Pore size (nm)	3.7	3.9	4.1
Pore volume (cm^3 g^{-1})	0.8	0.9	0.9

Moreover, the successful doping of Mn into MSNs was confirmed by the EDS elemental mapping. As shown in Figure 3-3, MM NPs showed clear signals of Mn, and MM2 showed stronger signals of Mn than MM1. The quantification analysis of Mn concentration was performed by ICP analysis, which showed that the mass concentrations of Mn in MSNs, MM1, and MM2 were 0, 13.9 ± 3.1%, and 24.9 ± 1.1%, respectively (Table 3-3).

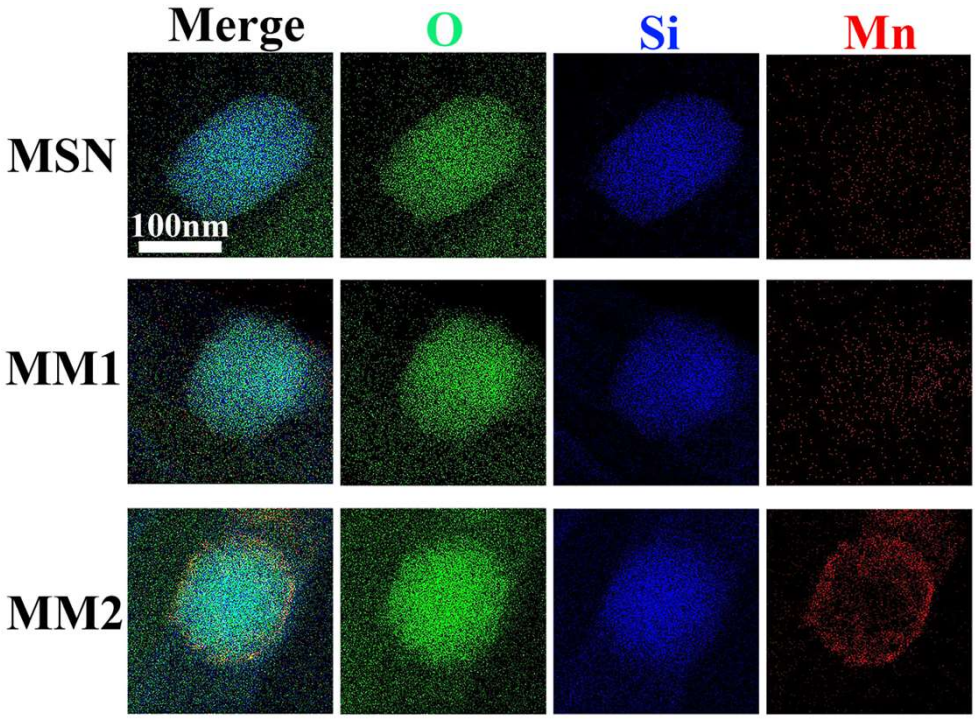

Figure 3-3 EDS elemental mapping of different NPs

Table 3-3 The mass concentrations of Mn doped into MSNs (%)

MSNs	MM1	MM2
0	13.9 ± 3.1%	24.9 ± 1.1%

The composition of the NPs was further analyzed by XRD and XPS analyses (Figure 3-4). As shown in the XRD patterns of the NPs (Figure 3-4a), all NPs showed a broad peak between 15 and 30°, which indicated the phase of amorphous silica. No obvious difference was observed for MSNs, MM1, and MM2. Then, the valence state of Mn in NPs was investigated by XPS analysis. As shown in the wide-scan XPS spectra of the NPs (Figure 3-4b), the peak of Si 2p was clearly observed, indicating the presence of the Si element in NPs. This was also confirmed in the high-resolution XPS spectra of Si 2p (Figure 3-4c). In addition, in the wide scan XPS spectra of MM NPs (Figure 3-4d), another peak of Mn 2p was clearly observed, indicating the presence of the Mn element in MM NPs. This was also confirmed by the high-resolution XPS spectra of Mn 2p, as shown in Figure 3-4d. Moreover, as shown in Table 3-4, the surface atomic concentration of Si 2p decreased and Mn 2p increased after Mn-doping. Moreover, in the fitted high-resolution XPS, spectra of Mn 2p for MM NPs, the Mn 2p1/2 and Mn 2p3/2 peaks were observed at binding energies of 643.65 eV and 656.36 eV, respectively, as shown in Figures 3-4(e-f). And the band gap value between Mn 2p3/2 and Mn 2p1/2 for MM NPs was about 11.8 eV, suggesting the presence of the MnO_2 phase in MM NPs [37-39].

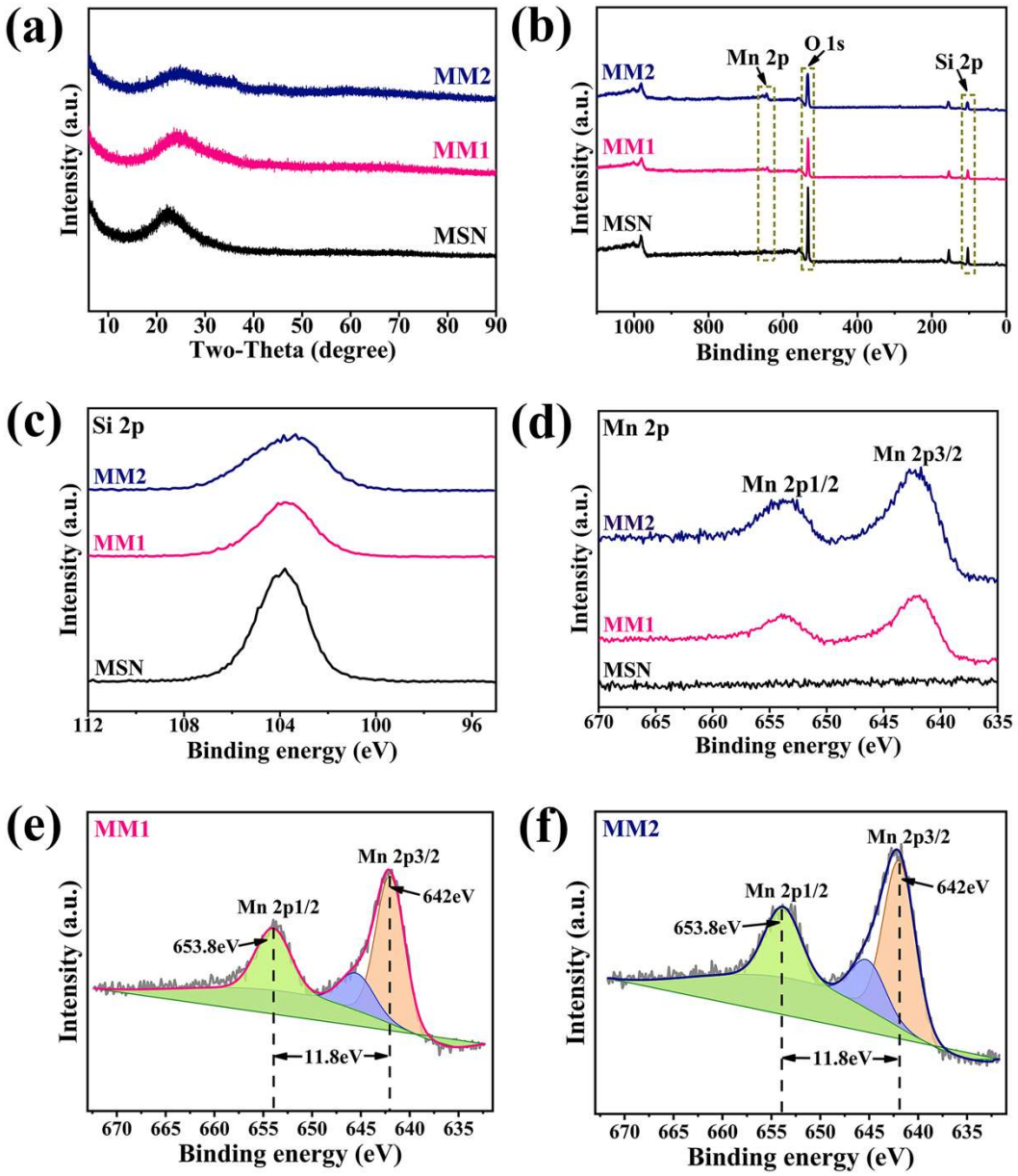

Figure 3-4 Analysis of phase and valence status of different NPs.(a) XRD patterns of the NPs; (b) Wide-scan XPS spectra of the NPs; (c) High-resolution XPS spectra of Si 2p; (d) High-resolution XPS spectra of Mn 2p; (e) Fitted high-resolution XPS spectra of Mn 2p in MM1; (f) Fitted high-resolution XPS spectra of Mn 2p in MM2.

Table 3-4 Surface atomic concentrations of NPs determined by XPS analysis (%)

	C 1s	O 1s	Si 2p	Mn 2p
MSNs	6.48	66.16	27.01	
MM1	12.26	61.24	23.62	2.89
MM2	6.9	65.25	23.71	4.14

Then, the surface charge of the NPs was assessed by zeta potential measurements. As shown in Figure 3-5, NPs showed different zeta potentials depending on the amount of Mn doped into MSNs and the pH of the buffer solution. MSNs, MM1, and MM2 were both negatively charged in PBS (-) and acetic acid buffer solution. And the zeta potential of the NPs decreased with an increase in the concentration of Mn doped into MSNs. Moreover, the DOX loading efficiency of MM NPs was measured. As shown in Table 3-5, MSNs, MM1, and MM2 showed DOX loading efficiencies of 54.4 ± 1.7%, 65.9 ± 2.7%, and 77.4 ± 1.9%, respectively.

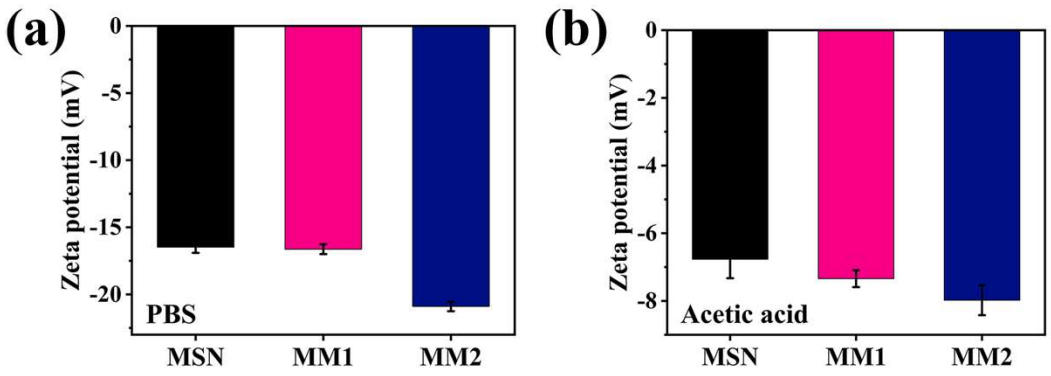

Figure 3-5 Analysis of zeta potential of different NPs in different solutions. (a) Zeta potential of the NPs in PBS (-) solution (n = 3); (b) Zeta potential of the NPs in acetic acid buffer solution (n = 3).

Table 3-5 DOX loading efficiency (%)

MSNs	MM1	MM2
54.4 ± 1.7	65.9 ± 2.7	77.4 ± 1.9

3.3.2 Regulation functions to TME

3.3.2.1 GSH depletion

As can be seen in Figure 3-6a, MM NPs induced obvious GSH depletion. The relative GSH level was detected as the generated TNB concentration [35], which was converted from DTNB by GSH. As shown in Fig. 3-6a, MM1 and MM2 showed a lower peak of TNB at 415 nm and a higher peak of DTNB at 325 nm compared with MSNs, indicating the enhanced GSH depletion capacity of MM NPs. With an extended reaction time, the peak of TNB at 415 nm and DTNB at 325 nm in MM NPs showed an obvious decrease and increase, respectively, indicating that MM NPs induced an obvious decrease in the GSH level. Whereas the peak of TNB at 415 nm or DTNB at 325 nm in MSNs showed no obvious change with an extended reaction time, indicating that MSNs showed no obvious influence on the GSH level. Moreover, MM2 showed a lower peak of TNB at 415 nm (57% and 40% of that in MSNs at 1 h and 2 h, respectively) than MM1 (72% and 63% of that in MSNs at 1 h and 2 h, respectively), indicating that MM2 showed a stronger GSH depletion capacity. To further confirm the reaction between NPs and GSH, the amount of Mn degraded from NPs was measured. As shown in Fig. 3-6b,

after reacting with GSH, an obvious release of Mn was observed in MM NPs, suggesting that Mn was degraded by GSH. Moreover, the degradation of Mn by GSH also improved the degradation of Si. As shown in Table 3-6, the concentrations of Si degraded from MSNs, MM1, and MM2 were 5.91 ± 0.03%, 6.83 ± 0.03%, and 7.77 ± 0.10% after reacting with GSH for 2 h, respectively.

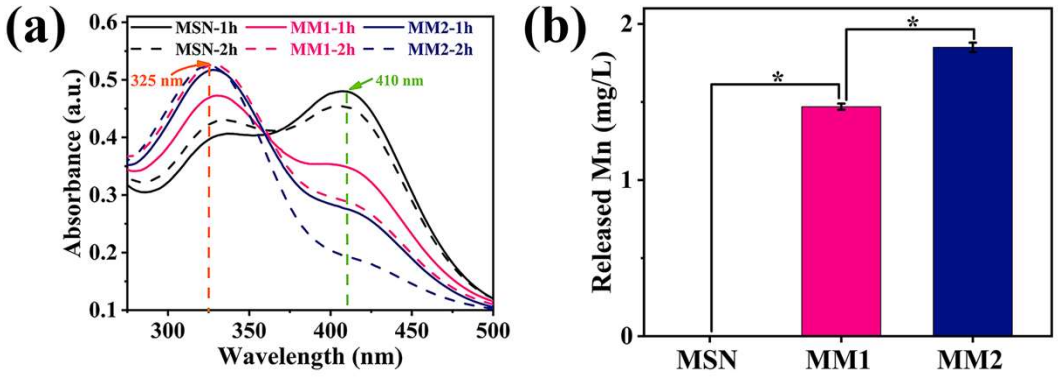

Figure 3-6 GSH depletion induced by MM NPs. (a) GSH depletion induced by NPs (n = 4) with different reaction times indicated by a decrease of the TNB concentration; (b) GSH depletion-induced Mn release from NPs (n = 3).

Table 3-6 Concentration of Si degraded (%)

MSNs	MM1	MM2
5.91 ± 0.03	6.83 ± 0.03	7.77 ± 0.1

3.3.2.2 ROS generation

As indicated in Figure 3-7, MM NPs induced obvious ROS generation in solutions and in LLC cells. The ROS generation induced by MM NPs was firstly investigated in $NaHCO_3$ solutions containing H_2O_2, in which Fenton-like reactions were induced by Mn^{2+} and H_2O_2, to generate •OH. The concentration of •OH was indicated by the degradation of MB as described in 3.2.2. As shown in Figure 3-7a, MSNs showed no obvious influence on the degradation of MB (the peak at 664 nm was 1.1, 1.1, and 1.0, respectively), which suggested that no •OH was generated. Whereas MM NPs induced a marked decrease in the peak of MB at 664 nm in a reaction time-dependent manner. After reaction for 0.5 h, MM1 and MM2 induced an obvious decrease in the peak of MB at 664 nm, which was 66% and 59% of that of MSNs, respectively. With the reaction time extended to 1.5 h, the peak of MB at 664 nm in MM1 and MM2 further decreased to 43% and 38% of that of MSNs, respectively. Then the ROS generation in LLC cells induced by MM NPs was investigated through measuring the fluorescence of intracellular DCF in LLC cells. As shown in Figure 3-7b, MSNs induced no increase in the intracellular ROS level, which had no significant difference from the control group. However, MM NPs induced an obvious increase in the intracellular ROS level compared with MSNs or the control group. The relative intracellular ROS levels enhanced by MM1 and MM2 were 10 times and 43 times higher than that in the control group, respectively. These results were consistent with the extracellular •OH generation results as shown in Figure 3-7a.

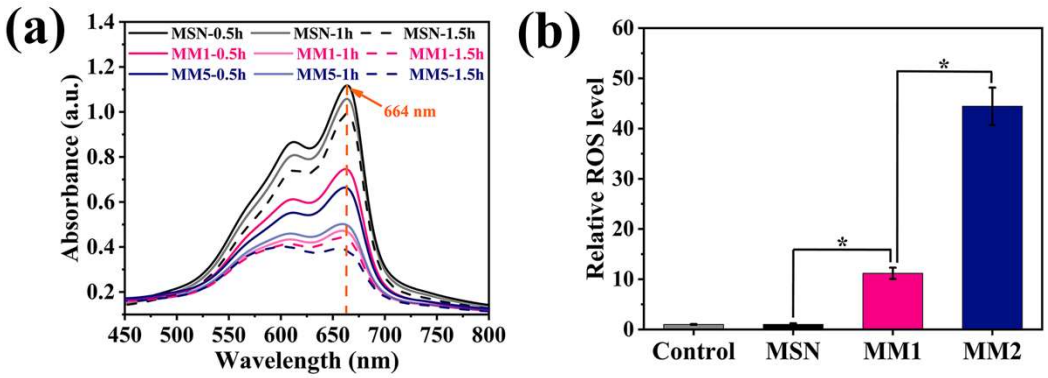

Figure 3-7 ROS generation induced by MM NPs. (a) ROS generation in solutions induced by NPs with different reaction times indicated by a decrease of the MB concentration; (b) Intracellular ROS generation induced by NPs (n = 10).

3.3.2.3 Oxygenation

MM NPs induced obvious oxygenation in solutions containing H_2O_2 as shown in Figure 3-8, The O_2 level was indicated as the decrease in the RDPP fluorescence intensity.28 As shown in Figure 3-8a, MM NPs at 100 mg mL^{-1} induced a clear decrease in the RDPP fluorescence intensity, suggesting an obvious generation of O_2. Notably, as shown in Figure 3-8b, MM NPs at 300 mg mL^{-1} induced a fast decrease in the RDPP fluorescence intensity in 15 min, which was faster than those at 100 mg mL^{-1}, whereas MSNs at both 100 mg mL^{-1} and 300 mg mL^{-1} induced no decrease in the RDPP fluorescence intensity. Notably, at the endpoint time, MM NPs at 100 mg mL^{-1} and 300 mg mL^{-1} induced a decrease in the RDPP fluorescence intensity by about 25% (Figure 3-8a) and 60% (Figure 3-8b), respectively.

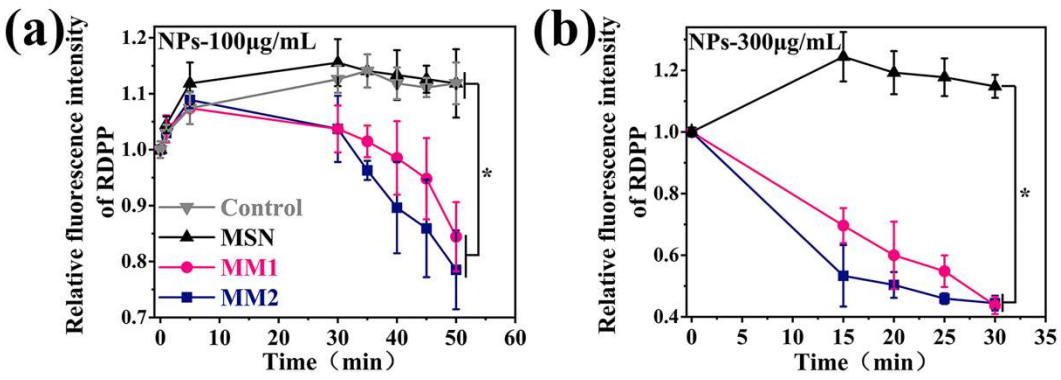

Figure 3-8 Oxygenation induced by MM NPs with different concentrations (n = 4). (a) NPs at 100 μg mL^{-1}; (b) NPs at 300 μg mL^{-1}.

3.3.2.4 Cell-killing enhancement

MM NPs showed good cellular uptake (Figure 3-9) and cell-killing effects (Figure 3-10). The cellular uptake was analyzed utilizing the rhodamine B-conjugated NPs (NPs-RhB). As shown in Figure 3-9, the distribution of the NPs-RhB fluorescence signals for MSNs, MM1, and MM2 overlapped almost completely with Lyso-Tracker green fluorescence signals, suggesting that MSNs, MM1, and MM2 were mainly localized in lysosomes after cellular internalization. Figure 3-10 showed the concentration-dependent cell-killing effect induced by MM NPs. As shown in Figure 3-10, MSNs showed no obvious cytotoxicity at a concentration of 40 mg mL^{-1}. Whereas MM NPs showed concentration-dependent cytotoxicity to LLC cells. MM1 and MM2 at a concentration of 40 mg mL^{-1} induced 10% and 51% cell death, respectively. MM2 at a concentration of 30 mg mL^{-1} also showed cytotoxicity, which induced about 15% cell death.

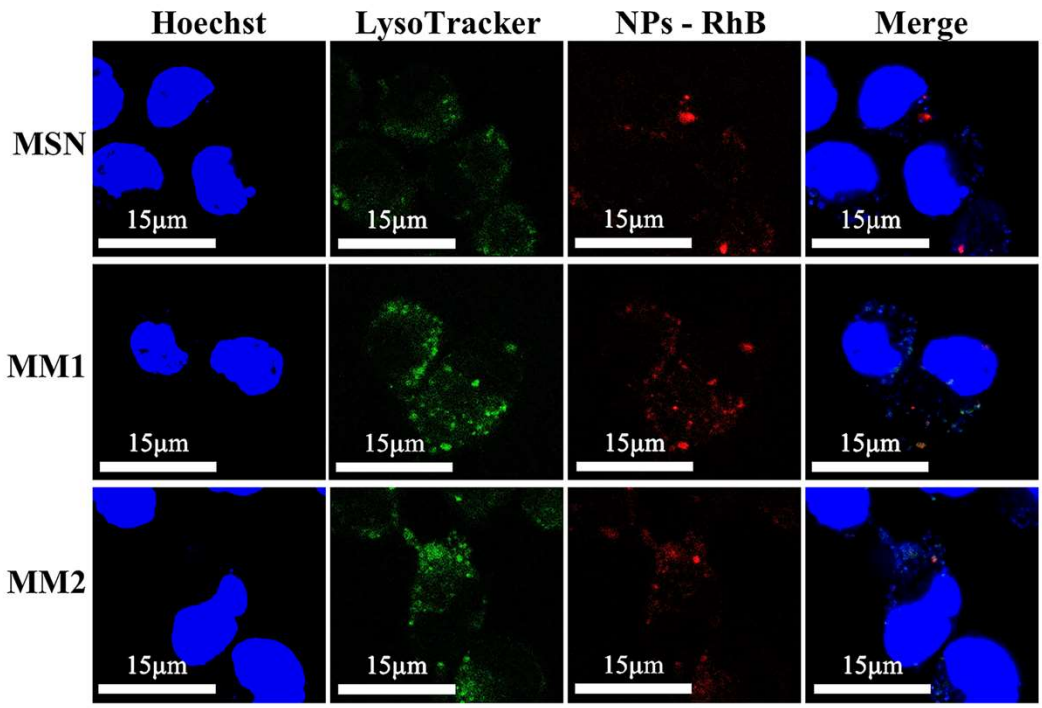

Figure 3-9 NPs uptake by LLC cells observed by CLSM

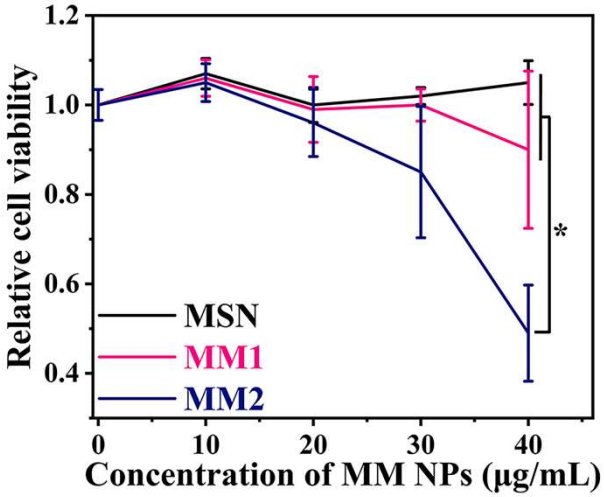

Figure 3-10 Cytotoxicity of the NPs with different concentrations (n = 7)

3.3.2.5 Immune activation

As revealed by the enhanced secretion of TNF-a (Figure 3-11), MM NPs showed obvious immune activation potential. In the process of the immune response, cytokines were related to the communication between immune cells, including macrophages. Therefore, the immune activation potential was investigated through measuring the cytokine secretion by macrophage-like cells incubated with NPs. As shown in Figure 3-11, MSNs, MM1, and MM2 showed the amount of TNF-a secreted by macrophage-like cells of 419.0 ± 30.03 pg mL^{-1}, 503.0 ± 13.4 pg mL^{-1}, and 491.9 ± 43.4 pg mL^{-1}, respectively, which was significantly higher than the control group (343.5 ± 22.0 pg mL^{-1}). Moreover, MM NPs showed a much higher amount of TNF-a secreted than MSNs, indicating the higher potential of immune activation by Mn-doping.

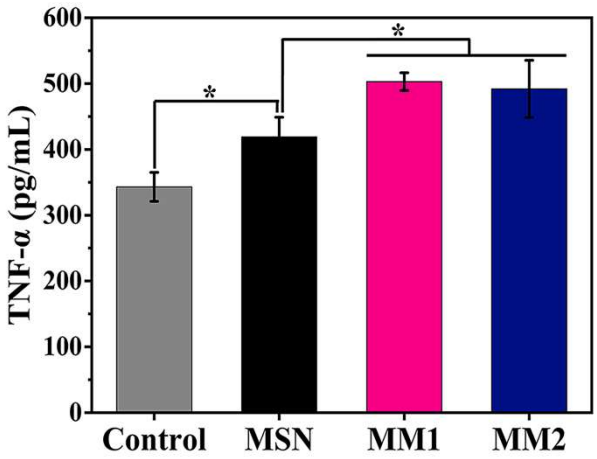

Figure 3-11 In vitro cytokine secretion by macrophage-like cells co-cultured with NPs

3.3.2.6 Degradation enhancements

As presented in Figure 3-12 and Figure 3-13, MM NPs showed improved degradation capacity compared with MSNs. The degradation performance of the NPs was carefully investigated by ICP analysis and TEM observation. The release profiles of Mn from NPs are shown in Figures 3-12(a-b). The obvious release of Mn was observed in MM NPs incubated in $NaHCO_3$ solution and $NaHCO_3$-GSH solution, which is consistent with the fact that MnO_2 was proved to be decomposed by reaction with H^+ or GSH in the TME [40]. The release of Mn from MM1 and MM2 after incubation in $NaHCO_3$ solution for 5d was 0.5 mg L^{-1} and 1.0 mg L^{-1}, respectively. Notably, the release of Mn from MM1 and MM2 after incubation in NaHCO3-GSH solution for 5 d was much faster than that in $NaHCO_3$ solution, the values of which are 12.6 mg L^{-1} and 13.4 mg L^{-1}, respectively. On the other hand, the degradation of Si was also enhanced as shown in Figures 3-12(c-d). The degradation concentration of Si in MM NPs was clearly higher than that in MSNs, which is 51.4 ± 1.2%, 62. 7 ± 0.8%, and 72.3 ± 2.3% for MSNs, MM1, and MM2 after 5 days of degradation, respectively, indicating that Mn-doping effectively enhanced the degradation of Si. Moreover, the degradation of MSNs, MM1 and MM2 was further confirmed by TEM. As shown in Figure 3-13, after incubation in GSH solutions for 1 d and 5 d, MSNs showed a little degradation, and the structure was still almost complete, whereas MM1 and MM2 incubated in GSH solution for 5 d showed faster degradation, and an obvious structural destruction was observed.

Moreover, MM2 incubated in GSH solution for 5d lost most of its structure and changed into pieces.

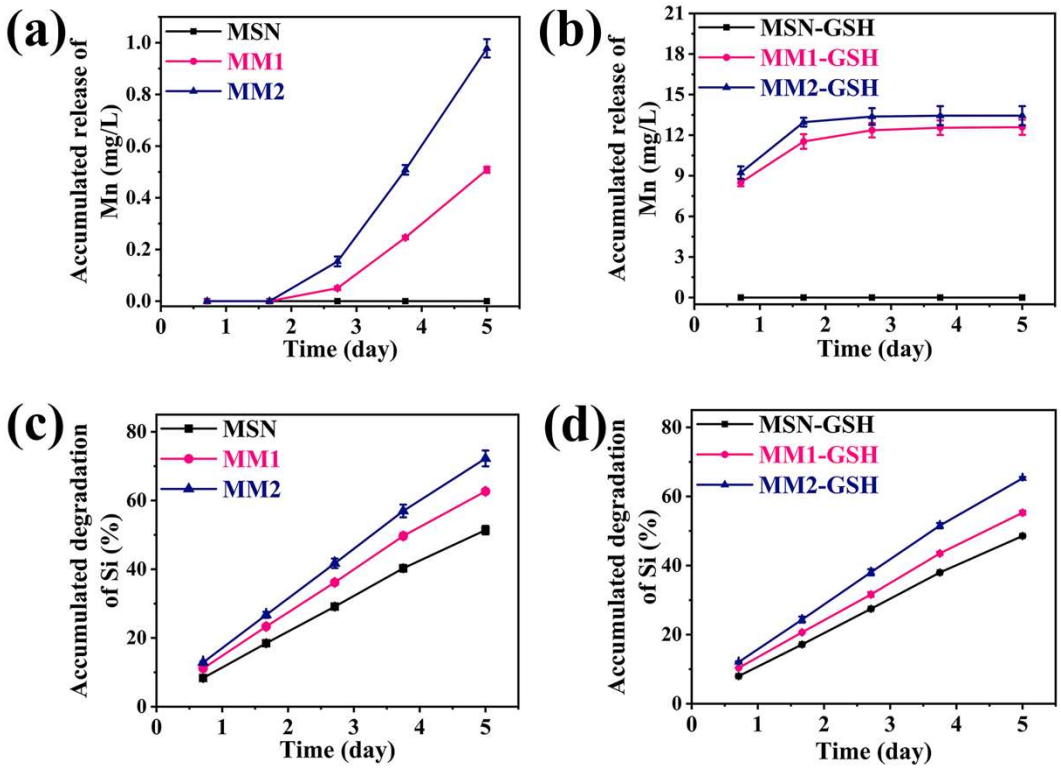

Figure 3-12 Enhanced degradation induced by Mn-doping (n=3). (a) Release of Mn from NPs incubated in $NaHCO_3$ solution; (b) Release of Mn from NPs incubated in $NaHCO_3$ solution containing 10 mM GSH; (c) Degradation of Si in NPs incubated in $NaHCO_3$ solution; (d) Degradation of Si in NPs incubated in $NaHCO_3$ solution containing 10 mM GSH.

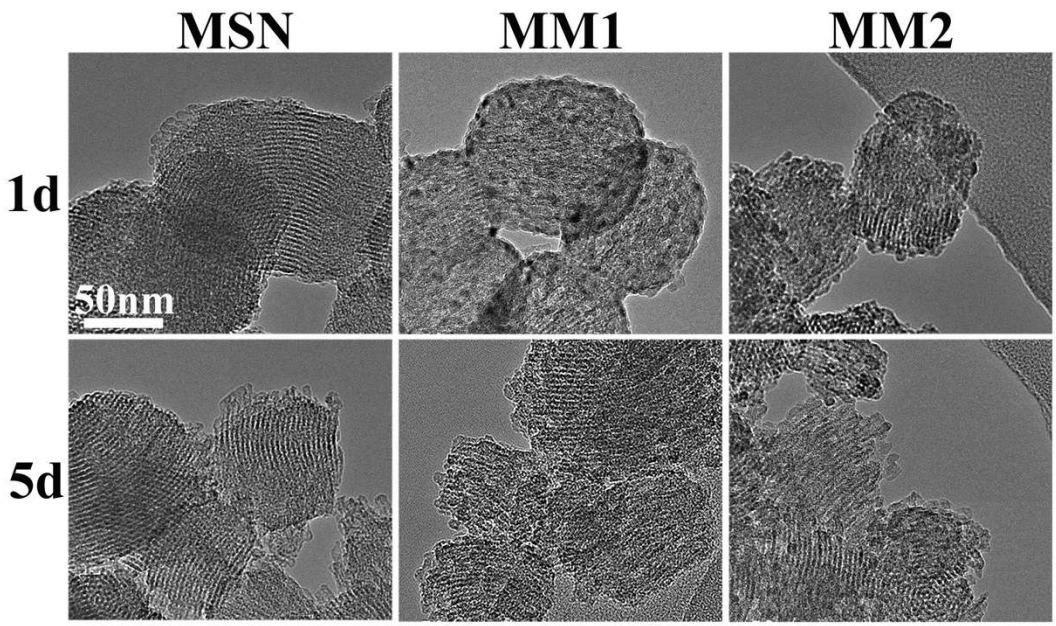

Figure 3-13 Mn-doping improved the degradation of Si observed by TEM.

3.3.3 In vivo anticancer effect

In vivo anticancer effect of chemo-immunotherapy induced by MM NPs was investigated utilizing a bilateral animal model (Figure 3-14a). As shown in Figure 3-14b, the growth of the primary tumors was clearly inhibited in the mice treated with saline, DOX alone, the combination of DOX and the anti-CTLA-4 antibody, the combination of DOX-MSNs and the anti-CTLA-4 antibody, the combination of DOX-MM1 and the anti-CTLA-4 antibody, and the combination of DOX-MM2 and the anti-CTLA-4 antibody. Whereas the growth of distant untreated tumors showed different growth depending on the treatments as shown in Figures 3-14(c-d). Specifically, the mice treated with saline, DOX alone, the combination of DOX and the anti-CTLA-4 antibody, the combination of DOX-MSNs and the anti-CTLA-4 antibody, the

combination of DOX-MM1 and the anti-CTLA-4 antibody, and the combination of DOX-MM2 and the anti-CTLA-4 antibody were tumor-free at percentages of 0%, 20%, 60%, 80%, 100%, and 100% at distant untreated sites, respectively. DOX alone showed rapid growth of tumors and a tumor-free ratio of 20%, indicating the low inhibitory effect on the growth of distant untreated tumors. The combination of DOX and the anti-CTLA-4 antibody inhibited the growth of distant untreated tumors and induced a tumor-free mice ratio of 60%, implying a certain degree of immune activation by the combination of DOX and the anti-CTLA-4 antibody. The combination of DOX-MSNs and the anti-CTLA-4 antibody showed a higher inhibitory effect on the growth of distant untreated tumors than DOX alone and the combination of DOX and the anti-CTLA-4 antibody, indicating the obvious enhancement of immune activation by MSNs. Notably, the mice treated with the combination of DOX-MM NPs and the anti-CTLA-4 antibody showed complete inhibition of distant untreated tumors with a tumor-free ratio of 100%, implying that Mn-doping further enhanced the immune activation capacity of MSNs.

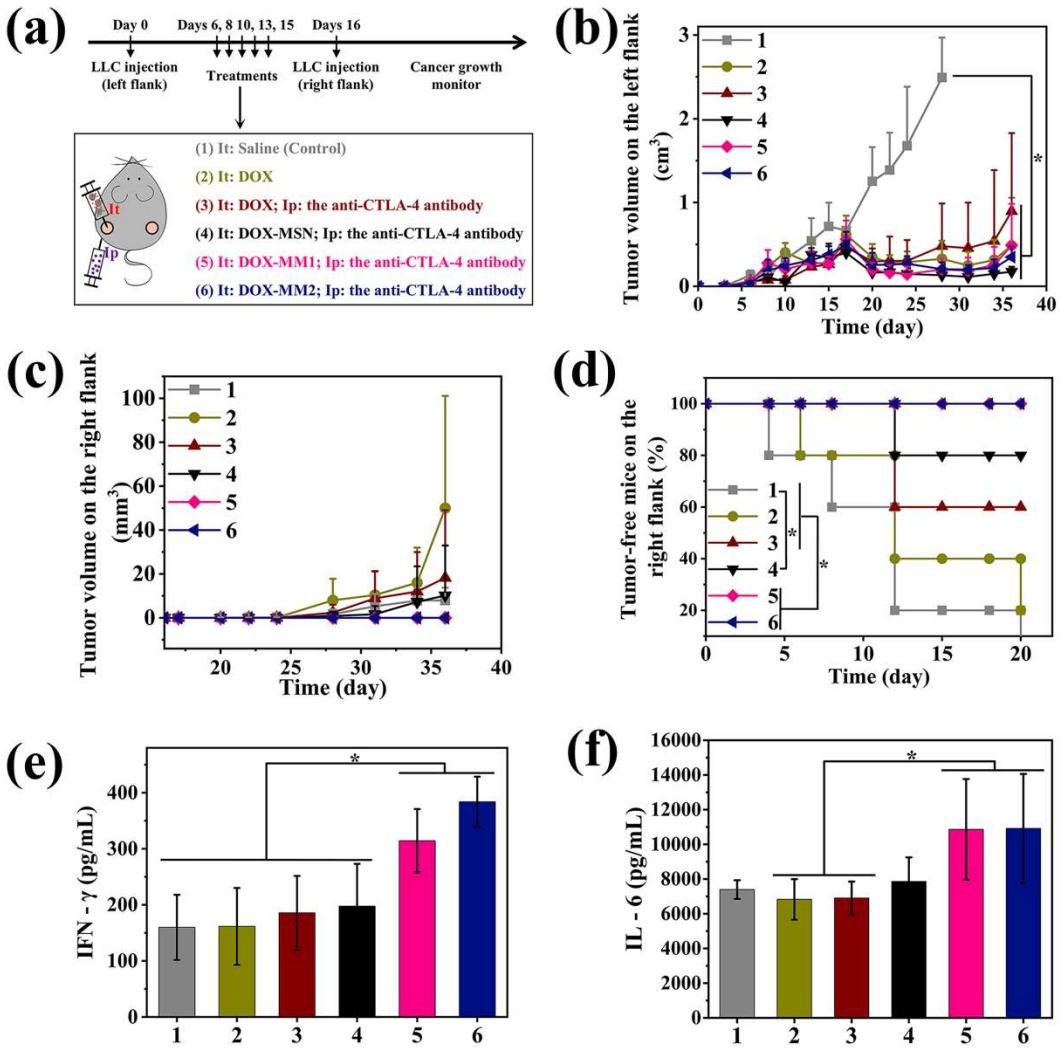

Figure 3-14 In vivo anticancer efficacy of MM NPs-enhanced chemo-immunotherapy in combination with the anti-CTLA-4 antibody (n = 5). (a) Illustration of different treatments; (b) The growth of primary tumors on the left flank; (c) The growth of distant untreated tumors on the right flank; (d) Ratio of tumor-free mice on the right flank; (e) Amounts of IFN-γ secreted from the splenocytes; (f) Amounts of IL-6 secreted from the splenocytes.

To further analyze the mechanisms of inhibitory effects on the distant untreated tumors by MM NPs, the amounts of cytokines secreted from the splenocytes of mice

were measured as shown in Figures 3-14(e-f). The mice treated with the combination of DOX-MM NPs and the anti-CTLA-4 antibody showed high amounts of IFN-γ and IL-6 secreted from the splenocytes of mice. The amounts of IFN-γ and IL-6 secreted from the splenocytes of mice treated with the combination of DOX-MM2 and the anti-CTLA-4 were about 2.1 times and 1.6 times that of mice treated with DOX alone, respectively. Moreover, the amounts of IFN-γ and IL-6 secreted from the splenocytes of mice treated with the combination of DOX-MM2 and the anti-CTLA-4 were about 1.9 times and 1.4 times that secreted from the splenocytes of mice treated with the combination of DOX-MSNs and the anti-CTLA-4, respectively, which contributed to the higher inhibition effect on distant untreated tumors as shown in Figure 3-14d.

3.4 Discussion

As shown in results from Figure 3-1 to Figure 3-5 and Table 3-2 to Table 3-5, Mn was successfully doped into MSNs through introducing $KMnO_4$ during the synthesis process of MSNs. Whereas the introducing of $KMnO_4$-induced Mn-doping caused no obvious influence on the morphology of MSNs as shown in Figure 3-1 but only influenced the concentration of Mn doped into MSNs, as shown in Table 3-3 and Table 3-4. According to the results of N_2 adsorption and desorption measurement and zeta potential analysis, Mn-doping induced a slight decrease in the specific surface area and increase in the pore size, as well as decrease in zeta potential. Moreover, the

mesoporous structure and the negatively charge was beneficial for drug loading [25]. Therefore, the Mn-doping slightly improved the drug loading efficiency of DOX compared with MSNs as shown in Table 3-5.

Due to the Mn-doping, MSNs were endowed with six new functions for TME regulation: GSH depletion (Figure 3-6), ROS generation (Figure 3-7), oxygenation (Figure 3-8), cell-killing effect (Figure 3-10), immune activation (Figure 3-11), and the degradation promotion (Figure 3-12).

(1) MM NPs induced an obvious GSH depletion as shown in Figure 3-6, which was induced by the reactions between GSH and MnO_2 [27], in which one molecule of –Mn–O– can consume two molecules of GSH [37]. Notably, the GSH played an important role in chemo-immunotherapy, which could potentially relieve the DOX resistance [38, 39], influence the DNA synthesis [35, 41], and increase the ROS level which can promote the maturation of dendritic cells (DCs), the activation and proliferation of effector T cells, the release of tumor-associated antigens (TAAs), and the exposure of damage-associated molecular patterns (DAMPs) [39]. Moreover, Mn-doping changed the Si–O–Si framework into the Si–O–Mn framework and thus accelerated the degradation of MSNs as shown in Table 3-6 [33], which was considered to be beneficial for decreasing the bio-accumulation of MSNs within the body and the potential bio-safety risks.

(2) MM NPs induced an obvious ROS generation, which showed a relation to the Mn concentration doped into MSNs as shown in Figure 3-7. On the one hand, Mn doped

into MSNs induced the Fenton-like reaction, which produced •OH in the presence of H_2O_2. On the other hand, Mn doped into MSNs also depleted GSH, one of the essential antioxidants in the powerful antioxidative systems that plays an important role in ROS consumption, which also contributed to the increase in ROS levels indirectly.

(3) MM NPs also induced obvious oxygenation in a concentration-dependent manner as shown in Figure 3-8, which was attributed to the high reactivity toward H_2O_2 to produce O_2. Notably, hypoxia was one of the limitations to the effect of chemo-immunotherapy, which contributed to drug resistance [42] and immunosuppression and metastasis [41, 43]. Therefore, the relief of hypoxia by MM NPs was considered to promote the synergistic efficiency of chemo-immunotherapy.

(4) MM NPs showed higher cytotoxicity to LLC cells compared with MSNs as shown in Figure 3-10, and the MM2 with higher concentration Mn showed the highest cytotoxicity to LLC cells, which was related to the increase in ROS levels caused by the Mn-doping induced GSH depletion and Mn-based Fenton-like reaction-induced ROS generation.

(5) MM NPs also improved the in vitro immune activation indicated by the enhanced secretion of cytokines by macrophage-like cells incubated with MM NPs as shown in Figure 3-11. In the process of the immune response, cytokines were related to the communication between immune cells, including macrophages. For example, TNF-a was important for cellular communication in many processes, including host defense and inflammation. Specifically, TNF-a was related to the DC maturation and CD8+ T

cell stimulation and activation of the inflammatory reactions of the innate immune system [44-46]. Moreover, previous research studies by our group showed that MSNs had the potential to activate immune responses by increasing the T helper (Th) 1 and Th 2 immune responses and promoting the accumulation of effector T cells [17-24]. And Mn ions were proved to activate immune responses by stimulating the cGAS/STING pathway [30].

(6) MM NPs also showed faster degradation behaviors in $NaHCO_3$ solution and $NaHCO_3$-GSH solution than MSNs, as shown in Figure 3-12 and Figure 3-13, which solved the problem of relatively low degradation of MSNs. Metal ion-doping has been proved to effectively weaken the Si–O–Si framework and promote the degradation of MSNs in our group's previous research studies [23]. Moreover, MnO_2 was decomposed by reactions with H^+ or GSH in the TME, in which two molecules of GSH was depleted by one molecule of -Mn-O- [40].

Based on the functions of GSH depletion, ROS generation, oxygenation, cell-killing effect, immune activation, and degradation promotion endowed by Mn-doping, MM NPs were further subjected to in vivo synergistic chemo-immunotherapy using a bilateral animal model (Figure 3-14a). the combination of DOX-MM NPs and the anti-CTLA-4 antibody obviously enhanced the synergistic efficiency of chemo-immunotherapy by inhibiting the growth of primary tumors and distant untreated tumors and enhancing the secretion of IFN-γ and IL-6 from the splenocytes. IFN-γ could enhance the activation of macrophages, promote the expression of major

histocompatibility (MHX) class I and II molecules and transcription factors, and induce the majority of antigen processing and presentation [47]. In our group's previous research studies, MSNs showed significant immunogenicity by promoting antigen presentation, cytokine secretion, CD 4+ and CD 8+ T cell proliferation, and effector memory T cell population [17-24]. Moreover, the new TME regulatory functions of GSH depletion, ROS generation, hypoxia relief, and immune activation endowed by Mn-doping synergistically contributed to furtherly improved immune responses [39, 42, 43]. And the Mn ions resulting from degrading MM NPs owing to the reactions with H^+ or GSH was also proved to activate the cGAS/STING pathway [30, 31], which was demonstrated to be critical in many anticancer therapies through the promotion of the tumor-specific antigen presentation and activation of cytotoxic T cells (CTLs) [48]. Taken together, the combination of MSNs, MnO_2, DOX, and the anti-CTLA-4 antibody synergistically contributed to the strong anticancer efficiency to inhibit both the growth of primary tumors and distant untreated tumors.

3.5 Conclusions

In this work, MM NPs with TME regulatory functions were constructed. Interestingly, MM NPs showed TME regulatory functions by inducing GSH depletion, ROS generation, oxygenation, cell-killing effect, immune activation, and degradation promotion. Moreover, the combination of DOX-MM NPs and the anti-CTLA-4 antibody induced higher immune responses than MSNs, which not only markedly

inhibited the growth of primary tumors but also showed a 100% tumor-free mice ratio at distant untreated sites and higher amounts of cytokines secreted from the splenocytes of mice in a bilateral animal model. This study suggested that MM NPs played an important role in improving the synergistic efficiency of chemo-immunotherapy by suppressing the growth of primary tumors and distant untreated tumors, which provided a potential method for cancer treatments. However, further studies on the detailed mechanistic analysis are required to explore the functions of MM NPs in chemo-immunotherapy.

Reference

1. Swartz MA, Iida N, Roberts EW, Sangaletti S, Wong MH, Yull FE, Coussens LM, DeClerck YA: **Tumor Microenvironment Complexity: Emerging Roles in Cancer TherapyTumor Microenvironment**. *Cancer research* 2012, **72**(10):2473-2480.

2. Chang C-H, Qiu J, O'Sullivan D, Buck MD, Noguchi T, Curtis JD, Chen Q, Gindin M, Gubin MM, Van Der Windt GJ: **Metabolic competition in the tumor microenvironment is a driver of cancer progression**. *Cell* 2015, **162**(6):1229-1241.

3. Liang K, Sun H, Yang Z, Yu H, Shen J, Wang X, Chen H: **Breaking the Redox Homeostasis: an Albumin-Based Multifunctional Nanoagent for GSH Depletion-Assisted Chemo-/Chemodynamic Combination Therapy**. *Advanced Functional Materials* 2021, **31**(22):2100355.

4. Qian C, Yu J, Chen Y, Hu Q, Xiao X, Sun W, Wang C, Feng P, Shen QD, Gu Z: **Light-activated hypoxia-responsive nanocarriers for enhanced anticancer therapy**. *Advanced materials* 2016, **28**(17):3313-3320.

5. Ye Y, Hu Q, Chen H, Liang K, Yuan Y, Xiang Y, Ruan H, Zhang Z, Song A, Zhang H: **Characterization of hypoxia-associated molecular features to aid hypoxia-targeted therapy**. *Nature metabolism* 2019, **1**(4):431-444.

6. Sangro B, Sarobe P, Hervás-Stubbs S, Melero I: **Advances in immunotherapy for hepatocellular carcinoma**. *Nature reviews Gastroenterology & hepatology*

2021, **18**(8):525-543.

7. Wang H, Mooney DJ: **Biomaterial-assisted targeted modulation of immune cells in cancer treatment**. *Nature materials* 2018, **17**(9):761-772.

8. Khalil DN, Smith EL, Brentjens RJ, Wolchok JD: **The future of cancer treatment: immunomodulation, CARs and combination immunotherapy**. *Nature reviews Clinical oncology* 2016, **13**(5):273-290.

9. Seidel J, Otsuka A, Kabashima K: **Anti-PD-1 and Anti-CTLA-4 Therapies in Cancer: Mechanisms of Action, Efficacy, and Limitations. Front Oncol. 8 (86): 1-14**. In.; 2018.

10. Chae YK, Arya A, Iams W, Cruz MR, Chandra S, Choi J, Giles F: **Current landscape and future of dual anti-CTLA4 and PD-1/PD-L1 blockade immunotherapy in cancer; lessons learned from clinical trials with melanoma and non-small cell lung cancer (NSCLC)**. *Journal for immunotherapy of cancer* 2018, **6**(1):1-27.

11. Salas-Benito D, Pérez-Gracia JL, Ponz-Sarvisé M, Rodriguez-Ruiz ME, Martínez-Forero I, Castañón E, López-Picazo JM, Sanmamed MF, Melero I: **Paradigms on immunotherapy combinations with chemotherapy**. *Cancer discovery* 2021, **11**(6):1353-1367.

12. Wu D, Fan Y, Yan H, Li D, Zhao Z, Chen X, Yang X, Liu X: **Oxidation-sensitive polymeric nanocarrier-mediated cascade PDT chemotherapy for synergistic cancer therapy and potentiated checkpoint blockade**

immunotherapy. *Chemical Engineering Journal* 2021, **404**:126481.

13. Chiu DK-C, Tse AP-W, Xu IM-J, Di Cui J, Lai RK-H, Li LL, Koh H-Y, Tsang FH-C, Wei LL, Wong C-M: **Hypoxia inducible factor HIF-1 promotes myeloid-derived suppressor cells accumulation through ENTPD2/CD39L1 in hepatocellular carcinoma**. *Nature communications* 2017, **8**(1):1-12.

14. Li Y, Patel SP, Roszik J, Qin Y: **Hypoxia-driven immunosuppressive metabolites in the tumor microenvironment: new approaches for combinational immunotherapy**. *Frontiers in immunology* 2018, **9**:1591.

15. Samanta D, Park Y, Ni X, Li H, Zahnow CA, Gabrielson E, Pan F, Semenza GL: **Chemotherapy induces enrichment of CD47+/CD73+/PDL1+ immune evasive triple-negative breast cancer cells**. *Proceedings of the National Academy of Sciences* 2018, **115**(6):E1239-E1248.

16. Zhou S, Zhong Q, Wang Y, Hu P, Zhong W, Huang C-B, Yu Z-Q, Ding C-D, Liu H, Fu J: **Chemically engineered mesoporous silica nanoparticles-based intelligent delivery systems for theranostic applications in multiple cancerous/non-cancerous diseases**. *Coordination Chemistry Reviews* 2022, **452**:214309.

17. Li X, Wang X, Qian G, Ito A: **Synergistical chemotherapy and cancer immunotherapy using dual drug-delivering and immunopotentiating mesoporous silica**. *Applied Materials Today* 2019, **16**:102-111.

18. Wang X, Li X, Ito A, Sogo Y, Ohno T: **Particle-size-dependent toxicity and**

immunogenic activity of mesoporous silica-based adjuvants for tumor immunotherapy. *Acta biomaterialia* 2013, **9**(7):7480-7489.

19. Wang X, Li X, Ito A, Sogo Y, Ohno T: **Pore size-dependent immunogenic activity of mesoporous silica-based adjuvants in cancer immunotherapy**. *Journal of Biomedical Materials Research Part A: An Official Journal of The Society for Biomaterials, The Japanese Society for Biomaterials, and The Australian Society for Biomaterials and the Korean Society for Biomaterials* 2014, **102**(4):967-974.

20. Wang X, Li X, Yoshiyuki K, Watanabe Y, Sogo Y, Ohno T, Tsuji NM, Ito A: **Comprehensive Mechanism Analysis of Mesoporous-Silica-Nanoparticle-Induced Cancer Immunotherapy**. *Advanced healthcare materials* 2016, **5**(10):1169-1176.

21. Wang X, Li X, Ito A, Watanabe Y, Sogo Y, Tsuji NM, Ohno T: **Stimulation of in vivo antitumor immunity with hollow mesoporous silica nanospheres**. *Angewandte Chemie* 2016, **128**(5):1931-1935.

22. Wang X, Li X, Ito A, Yoshiyuki K, Sogo Y, Watanabe Y, Yamazaki A, Ohno T, Tsuji NM: **Hollow structure improved anti-cancer immunity of mesoporous silica nanospheres in vivo**. *Small* 2016, **12**(26):3510-3515.

23. Wang X, Li X, Ito A, Sogo Y, Watanabe Y, Tsuji NM, Ohno T: **Biodegradable metal ion-doped mesoporous silica nanospheres stimulate anticancer Th1 immune response in vivo**. *ACS applied materials & interfaces* 2017,

9(50):43538-43544.

24. Wang X, Ihara S, Li X, Ito A, Sogo Y, Watanabe Y, Tsuji NM, Yamazaki A: **Si-doping increases the adjuvant activity of hydroxyapatite nanorods**. *Colloids and Surfaces B: Biointerfaces* 2019, **174**:300-307.

25. Yu L, Chen Y, Lin H, Gao S, Chen H, Shi J: **Magnesium-engineered silica framework for pH-accelerated biodegradation and DNAzyme-triggered chemotherapy**. *Small* 2018, **14**(35):1800708.

26. Bi H, Dai Y, Yang P, Xu J, Yang D, Gai S, He F, An G, Zhong C, Lin J: **Glutathione and H2O2 consumption promoted photodynamic and chemotherapy based on biodegradable MnO2–Pt@ Au25 nanosheets**. *Chemical Engineering Journal* 2019, **356**:543-553.

27. Chen H, Tian J, He W, Guo Z: **H2O2-activatable and O2-evolving nanoparticles for highly efficient and selective photodynamic therapy against hypoxic tumor cells**. *Journal of the American Chemical Society* 2015, **137**(4):1539-1547.

28. Liu J, Wu M, Pan Y, Duan Y, Dong Z, Chao Y, Liu Z, Liu B: **Biodegradable nanoscale coordination polymers for targeted tumor combination therapy with oxidative stress amplification**. *Advanced Functional Materials* 2020, **30**(13):1908865.

29. Liu Y, Zhou Z, Liu Y, Li Y, Huang X, Qian C, Sun M: **H 2 O 2-activated oxidative stress amplifier capable of GSH scavenging for enhancing tumor**

photodynamic therapy. *Biomaterials science* 2019, **7**(12):5359-5368.

30. Wang C, Guan Y, Lv M, Zhang R, Guo Z, Wei X, Du X, Yang J, Li T, Wan Y: **Manganese increases the sensitivity of the cGAS-STING pathway for double-stranded DNA and is required for the host defense against DNA viruses**. *Immunity* 2018, **48**(4):675-687. e677.

31. Lv M, Chen M, Zhang R, Zhang W, Wang C, Zhang Y, Wei X, Guan Y, Liu J, Feng K: **Manganese is critical for antitumor immune responses via cGAS-STING and improves the efficacy of clinical immunotherapy**. *Cell research* 2020, **30**(11):966-979.

32. Lin LS, Song J, Song L, Ke K, Liu Y, Zhou Z, Shen Z, Li J, Yang Z, Tang W: **Simultaneous Fenton-like ion delivery and glutathione depletion by MnO2-based nanoagent to enhance chemodynamic therapy**. *Angewandte Chemie* 2018, **130**(18):4996-5000.

33. Li X, Zhang X, Zhao Y, Sun L: **Fabrication of biodegradable Mn-doped mesoporous silica nanoparticles for pH/redox dual response drug delivery**. *Journal of Inorganic Biochemistry* 2020, **202**:110887.

34. Liu C, Cao Y, Cheng Y, Wang D, Xu T, Su L, Zhang X, Dong H: **An open source and reduce expenditure ROS generation strategy for chemodynamic/photodynamic synergistic therapy**. *Nature communications* 2020, **11**(1):1-9.

35. Markovic J, Borras C, Ortega A, Sastre J, Vina J, Pallardo FV: **Glutathione is**

recruited into the nucleus in early phases of cell proliferation. *Journal of Biological Chemistry* 2007, **282**(28):20416-20424.

36. Huang J, Huang Y, Xue Z, Zeng S: **Tumor microenvironment responsive hollow mesoporous Co9S8@ MnO2-ICG/DOX intelligent nanoplatform for synergistically enhanced tumor multimodal therapy**. *Biomaterials* 2020, **262**:120346.

37. Tang H, Li C, Zhang Y, Zheng H, Cheng Y, Zhu J, Chen X, Zhu Z, Piao J-G, Li F: **Targeted Manganese doped silica nano GSH-cleaner for treatment of Liver Cancer by destroying the intracellular redox homeostasis**. *Theranostics* 2020, **10**(21):9865.

38. Estrela JM, Ortega A, Obrador E: **Glutathione in cancer biology and therapy**. *Critical reviews in clinical laboratory sciences* 2006, **43**(2):143-181.

39. Xiong Y, Xiao C, Li Z, Yang X: **Engineering nanomedicine for glutathione depletion-augmented cancer therapy**. *Chemical Society Reviews* 2021, **50**(10):6013-6041.

40. Yang G, Xu L, Chao Y, Xu J, Sun X, Wu Y, Peng R, Liu Z: **Hollow MnO2 as a tumor-microenvironment-responsive biodegradable nano-platform for combination therapy favoring antitumor immune responses**. *Nature communications* 2017, **8**(1):1-13.

41. Wood GE, Hockings H, Hilton DM, Kermorgant S: **The role of MET in chemotherapy resistance**. *Oncogene* 2021, **40**(11):1927-1941.

42. Rankin EB, Giaccia AJ: **Hypoxic control of metastasis**. *Science* 2016, **352**(6282):175-180.

43. Gilkes DM, Semenza GL, Wirtz D: **Hypoxia and the extracellular matrix: drivers of tumour metastasis**. *Nature Reviews Cancer* 2014, **14**(6):430-439.

44. Balkwill F: **TNF-α in promotion and progression of cancer**. *Cancer and Metastasis Reviews* 2006, **25**(3):409-416.

45. Rincón M, Anguita J, Nakamura T, Fikrig E, Flavell RA: **Interleukin (IL)-6 directs the differentiation of IL-4–producing CD4+ T cells**. *The Journal of experimental medicine* 1997, **185**(3):461-470.

46. Locksley RM, Killeen N, Lenardo MJ: **The TNF and TNF receptor superfamilies: integrating mammalian biology**. *Cell* 2001, **104**(4):487-501.

47. Aindelis G, Tiptiri-Kourpeti A, Lampri E, Spyridopoulou K, Lamprianidou E, Kotsianidis I, Ypsilantis P, Pappa A, Chlichlia K: **Immune responses raised in an experimental colon carcinoma model following oral administration of Lactobacillus casei**. *Cancers* 2020, **12**(2):368.

48. Chen Q, Sun L, Chen ZJ: **Regulation and function of the cGAS–STING pathway of cytosolic DNA sensing**. *Nature immunology* 2016, **17**(10):1142-1149.

Chapter 4 Photo-immunotherapy enhanced by IMM

4.1 Introduction

Different cancers still cause a death rate of over 10 million every year around the world, indicating the urgent to develop new strategies to treat cancers [1]. Because the clinically used anticancer therapies have been limited by some drawbacks, such as the impossible to remove all cancer cells by surgery, and poor tumor-targeting capability, toxicity to healthy tissues, and multidrug resistance induced by chemotherapy and radiotherapy [2]. Therefore, many new anticancer therapies have been developed. For example, phototherapy, a strategy that applies the near-infrared light (NIR) wavelength (650nm-1350nm) to induce damage to tumor tissues [3], has drawn much attention due to its minimal invasiveness with good selectivity and nondrug resistance and has been also utilized to combine with immunotherapy to improve the anticancer effect [4, 5]. Phototherapy has two different mechanisms to induce cell death, which utilizes PA and PS drugs that can absorb NIR wavelength to produce heat through internal conversion and release ROS through intersystem crossing relaxation for the PTT and PDT, respectively [6]. For PTT, when the temperature of tissues irradiated exceeds 39 ^{o}C, protein aggregation even denaturation may occur. With a further increase in temperature, the cells may become inactivated and produce heat shock protein (HSP) to reduce the damage from heat. Then a further increase in temperature to about 43-45 ^{o}C may induce the acceleration of biochemical reactions and ROS generation, which

leads to protein denaturation and cell membrane disruption and thus induce cell death by necrosis. For PDT, PS drugs absorb photons and produce single oxygen ($^1O_2$) with the Type Ⅰ process or produce various ROS (superoxide anion radicals, H_2O_2, and •OH) with the Type Ⅱ process to induce apoptosis, necrosis, and autophagy [7].

Originally, phototherapy has been applied to destruct tumor tissues. Whereas eradication of primary tumors is far from enough for cancer treatments. Firstly, phototherapy may cause some side effect on the healthy tissue and its inhibitory effect on the growth of primary tumors is limited. For PTT, the increased temperature may not only damage tumor tissues but also has the potential to influence the surrounding healthy tissues due to the overheating [8-10]. For PDT, the hypoxic TME can influence the PDT-induced ROS generation efficiency, and the antioxidant molecules in TME can consume ROS generated, indicating that the complex TME may strongly limit the ROS-induced damage and the cell-killing effect of PDT [9]. Moreover, different PA and PS agents have shown some drawbacks, including photobleaching, poor solubility, and limited photothermal conversion efficiency. Secondly, phototherapy is also reported as not enough effective in inhibiting tumor metastasis, which is related to over 90% of death from different cancers [11]. Although it has been found that phototherapy can also induce ICD and activate immune systems through releasing DAMPs [12, 13]. For example, the PTT-induced increase in body temperature can promote the homing of immune cells, the activation of immune

cells of CTLs, DCs, and NK cells, and the inhibition of immune suppression [14]. And PDT can induce ROS generation after laser irradiation, which further induces ICD to enhance the antigen presentation and activate the T cells for killing the cancer cells, which is related to the release of calreticulin exposure and dying tumor cell debris [4]. However, the activation of immune responses by PDT or PTT is not enough [15]. The high temperature for rapid tumor ablation is unfavorable for immune activation. The tumor temperature above 45 ^{o}C may induce damage to vasculature, chemokines, and cytokines, thus influencing the strength of immune responses, which leads to a common case of relapse of large tumors [9].

Considering these limitations of phototherapy, different strategies have been developed, including loading PA and PS agents to nanoparticles to address the drawbacks of PA and PS agents, introducing nanomaterials to regulate TME, and combing it with other anticancer therapies. MSNs have been usually applied to load therapeutic drugs due to their facile functionalization and controllable shape, size, and pore structures [16] and to enhance the effect of immunotherapy due to their roles in activating immune responses [17-24]. Whereas the degradation speed of MSNs is relatively low due to the stable Si-O-Si framework and MSNs have no regulation functions to TME. Interestingly, Mn-doping has shown potential in improving the degradation speed of MSNs through weakening the stable Si-O-Si framework [25, 26]. Additionally, Mn-based nanomaterials have been widely studied on the application to regulate TME through relieving hypoxia and breaking redox balance, which can result

in enhanced effect of different anticancer therapies, including RT, chemotherapy, as well as phototherapy [26-30]. Moreover, Mn-based nanomaterials can also induce the CDT due to Fenton-like reactions [31, 32]. And CDT has no limitation in penetration depth, which is one of the big limitations in the efficiency of PDT or PTT. More importantly, Mn-based nanomaterials also have shown the potential for immune activation through increasing the sensitivity of the cGAS-STING pathway [33-37]. Whereas the research about the strategy of using nanomaterials to synergistically regulate the TME to meet the conditions needed for phototherapy and to enhance the immune activation in phototherapy, leading to the enhanced inhibitory effect on both tumor growth and tumor metastasis is still rare.

In this work, Mn-doped MSNs were first synthesized and used to load IR 780, and then coated with Mn to from IMM, which was further applied to enhance the synergistic efficiency of the combinational anticancer therapy of immunotherapy and phototherapy, as shown in Scheme 4-1. Compared with IR 780, IMM showed better photothermal capability indicated by the stable photothermal conversion efficiency even after receiving irradiation for 4 cycles of 10min or being stored in darkness for 2 weeks at room temperature, and better photodynamic capability indicated by the higher efficiency in producing $^1O_2$. Additionally, IMM also possessed chemodynamic effect due to the Mn-induced Fenton-like reactions with H_2O_2 and regulation functions to TME through oxygenation, ROS generation, and GSH depletion. Notably, in a bilateral animal model for the combinational anticancer therapy of phototherapy and

immunotherapy, the combination of an 808nm laser irradiation and IMM showed a better inhibitory effect on the growth of both primary tumors and distant untreated tumors, compared with the combination of an 808nm laser irradiation and IR 780. Therefore, it was considered that IMM with functions of TME regulation and immune activation may provide a strategy for the combinational anticancer therapy of phototherapy and immunotherapy to inhibit both tumor growth and tumor metastasis.

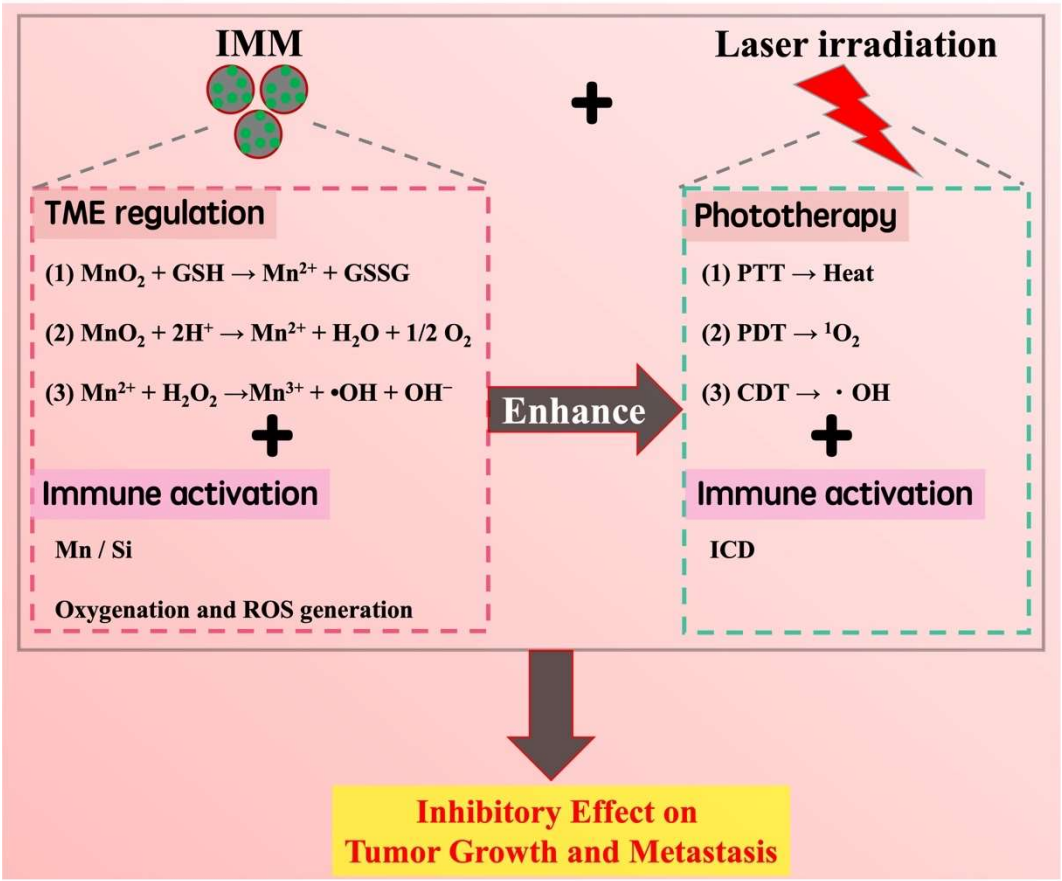

Scheme 4-1 Schematic illustration of IMM-enhanced synergistic inhibitory effect on tumor growth and metastasis

4.2 Materials and methods

4.2.1 Materials

Hexadecyltrimethylammonium bromide (CTAB), tetraethyl orthosilicate (TEOS), potassium permanganate ($KMnO_4$) were from Wako Chemical, Ltd. MB and hydrogen peroxide (H_2O_2, 30%) were from FUJIFILM Wako Pure Chemical Co. 5 mol L^{-1}-sodium hydroxide solution (NaOH) was from Nacalai Tesque, Inc. Glutathione reduced form (GSH) was from Tokyo Chemical Industry Co., Ltd. Liperfluo was from Dojindo Molecular Technologies, Inc. IR 780 was from Sigma-Aldrich Japan. Singlet oxygen sensor green probe was from Thermo Fisher Scientific Inc.

4.2.2 Synthesis of Mn-coated IR 780-loaded MM2 (IMM)

MM2 were synthesized as described before. MM2 were further used to load IR 780 and covered with Mn. Different nanoparticles with different Mn covering (loaded with IR 780 and without IR 780) were synthesized through changing the $KMnO_4$ content during the covering process as shown in Table 4-1.

In specifically, 1g of MM2 and 0.2mg of IR 780 were dispersed in 1mL of ultrapure water and shaken at a speed of 1000 rpm for 24 h in darkness after ultrasound for 1min. After centrifugated at a speed of 15000rpm for 10min, IR 780-loaded MM2 were obtained. Then, different concentrations of PEG and $KMnO_4$ were dispersed into IR 780-loaded MM2 solutions, and the solutions were further mixed using ultrasound for

2min. Finally, Mn-coated IR 780-loaded MM2 (IMM) were obtained after washing in water for once. And the IR 780 loading efficiency was defined as follows:

IR 780 loading efficiency (%) = 100 x (Amount of IR 780 added - Amount of IR 780 in the supernatant) / (Amount of IR 780 added).

Table 4-1 The process of IMM synthesis

	MM2 (g)	IR 780 (mg)	PEG (mL)	$KMnO_4$ (mg)
IMM1	1	0.2	0.2	0.2
IMM2	1	0.3	0.3	0.3
MM2-1	1	-	0.2	0.2
MM2-2	1	-	0.3	0.3

4.2.3 Characterization of IMM

The morphology of the NPs was observed by field emission scanning electron microscopy (FE-SEM, HITACHI, Japan) and field emission transmission electron microscopy (TEM-EDS, JEOL, Japan). The Si/Mn ratio and phase of the NPs were measured by inductively coupled plasma atomic emission spectroscopy (ICP-AES, SPS7800, Seiko Instruments, Japan) and X-ray diffractometry (XRD, RINT 2550, Rigaku, Japan), respectively. The chemical composition of the NPs was determined by X-ray photoelectron spectroscopy (XPS, PHI 5000 VersaProbe III, ULVAC-PHI, Japan).

4.2.4 Photothermal capability of IMM

The photothermal capability of IMM was investigated through changing the concentration of IR 780 and the power density of the laser. Firstly, IMM was dispersed into ultrapure water to prepare the IMM solutions with different concentrations of IR 780 (50, 100, and 200μg mL^{-1}), which were further exposed to the 808nm laser irradiation. And the temperature was measured at predetermined time points using a thermal imaging camera (FLIR-E63900). The photostability was analyzed through measuring the photothermal conversion efficiency of IMM and IR 780 exposed to an 808nm laser irradiation for 4 times (10min/time). The photostability was further confirmed through measuring the photothermal conversion efficiency of IMM and IR 780 after being stored in darkness for 2 weeks at room temperature.

4.2.5 Photodynamic capability of IMM

The photodynamic capability of IMM after 808nm laser irradiation was characterized through measuring the level of singlet oxygen ($^1O_2$) with a SOSG probe induced by IMM and IR 780 or IMM and IR 780 after being stored in darkness for 2 weeks at room temperature. Briefly, IMM with 100μg mL^{-1} of IR 780 and 2μL of SOSG (5mM) were added into a 96-well plate. Then the mixed solution was exposed to the 808nm laser irradiation with different power densities. Finally, the fluorescence at 492 nm/530 nm was measured immediately using a microplate reader.

4.2.6 TME regulation functions induced by IMM

4.2.6.1 Oxygenation

IMM was dispersed into ultrapure water to prepare different concentrations of IR 780 (10, 50, 100, and 200μg mL^{-1}). Then H_2O_2 (10mM) and RDPP (3μM) were added and the solution was incubated at 37°C for 10min. Then the fluorescence of RDPP (Ex/Em = 450nm/630nm) was measured using a microplate reader. Data were normalized to the control group.

The influence of oxygenation on photodynamic capability was analyzed. IMM with 100μg mL^{-1} IR 780 was covered by liquid paraffin to avoid the diffusion of O_2. Then SOSG and H_2O_2 were added into a 96-well plate before exposure to an 808nm laser irradiation with a power density of 0.75A. Finally, the fluorescence at 492 nm/530 nm was measured at determined time points using a microplate reader.

4.2.6.2 GSH depletion

GSH depletion induced by IMM was investigated using DTNB. The relative GSH level was detected as the generated TNB concentration, which was converted from DTNB by GSH. GSH (10 mM) and IMM with different concentrations of IR 780 (50, 250μg mL^{-1}) were mixed in ultrapure water and cultured at 37 °C. After 30min, the mixed solutions were centrifuged at 10000 rpm for 5 min. Then, the supernatants were mixed with DTNB (0.1 mg mL^{-1}) and reacted for 10 min. The solution absorbance of

TNB at 415 nm was measured after being diluted to 2 mL using a UV-vis absorption spectrometer (V-730, JASCO, Japan).

4.2.6.3 ROS generation

ROS generation induced by Fenton-like reactions was measured through the degradation of MB caused by the •OH generated. Briefly, IMM with IR 780 concentration of 10 μg mL^{-1} were firstly dispersed in 25 mM $NaHCO_3$ solution containing different concentrations of GSH (0, 10 mM) and H_2O_2 (10 mM) and incubated at 37 ºC for 30min. Then the mixed solutions were centrifuged at 10 000 rpm for 5 min. And the supernatants were mixed with MB (10 mg mL^{-1}), followed by incubation at 37 ºC for 30 min. Finally, the absorbance of MB at 664 nm was measured at determined time points using a UV-vis absorption spectrometer.

4.2.7 In vitro cell-killing effect induced by IMM

The invitro cell-killing effect induced by IMM with a concentration of IR 780 at 2.5μg mL^{-1} was first analyzed by staining the cells with using a calcein - AM (green fluorescence) / PI (red fluorescence) double staining kit. The in vitro cell-killing effect in different cancer cells incubated with IMM of different concentrations was further investigated using the CCK-8 assay. Different cancer cells (MOC and LLC cells) were seeded into a 48-well plate at a concentration of $2x10^4$ cells $well^{-1}$ and incubated overnight. Then IMM with different concentrations of IR 780 (2.5, 5, and 10μg mL^{-1}) was added. After incubation with cancer cells for 2h, cancer cells were exposed to the

808nm laser irradiation at the power densities of 0.75A for 10min. Finally, the cell viability was measured using the CCK-8 assay.

4.2.8 In vivo anticancer effect of the combinational anticancer therapy of immunotherapy with phototherapy

The animal experiments were approved by the Ethical Committee of the National Institute of Advanced Industrial Science and Technology (AIST). All of the animal experiments and feeding were carried out in accordance with the guidelines of the Ethical Committee of AIST, Japan.

Mice (C57BL / 6JJcl, female, 5 weeks old, CLEA, Japan) were randomly divided into seven groups (n = 5). On day 0, the mice were subcutaneously injected with live MOC cells into the left hind legs (10^6 cells mouse^{-1}) to simulate primary tumors. On days 3, 4, and 6, the mice were treated with different treatments as follows.

(1) Mice were treated with an intratumor injection of IMM1 with IR 780 concentration at 40 μg mouse^{-1} in saline (50 μL) and exposed to an 808nm laser irradiation with a power density of 0.75A for 10min.

(2) Mice were treated with an intratumor injection of IMM2 with IR 780 concentration at 40 μg mouse^{-1} in saline (50 μL) and exposed to an 808nm laser irradiation with a power density of 0.75A for 10min.

(3) Mice were treated with an intratumor injection of IR 780 at the concentration of 40 μg mouse^{-1} in saline (50 μL) and exposed to an 808nm laser irradiation with a power density of 0.75A for 10min.

(4) Mice were treated with an intratumor injection of IMM1 with IR 780 concentration at 40 μg mouse^{-1} in saline (50 μL).

(5) Mice were treated with an intratumor injection of IMM2 with IR 780 concentration at 40 μg mouse^{-1} in saline (50 μL)

(6) Mice were treated with an intratumor injection f IR 780 at a concentration of 40 μg mouse^{-1} in saline (50 μL).

(7) Mice were treated with an intratumor injection of saline (50 μL).

On day 7, the mice were subcutaneously injected with live MOC cells into the right hind legs (2×10^5 cells mouse^{-1}) to simulate the metastatic tumors. The tumor diameters on both sides of the hind legs were measured using a caliper at determined time points. On day 21, spleens were collected and digested with a tissue protein extraction reagent. The extract was centrifuged, and the supernatant was collected. The amounts of cytokines secreted were measured using mouse IL-6, IL-12, and TNF-α kits (BD Bioscience, USA) in accordance with the manufacturer's instructions.

4.3 Results

4.3.1 Characterization

As can be seen in the SEM images (Figure 4-1), an obvious difference in the surface of MM2-1 and MM2-2 was observed compared with MM2 (Figure 3-1), indicating that Mn-coated MM2 were successfully synthesized. Moreover, the element distribution was confirmed by EDS elemental mapping. As shown in Figure 4-2, MM2-1 and MM2-

2 showed clear signals of Mn, indicating the successful coating of Mn. Additionally, MM2-2 showed stronger signals of Mn than MM2-1.

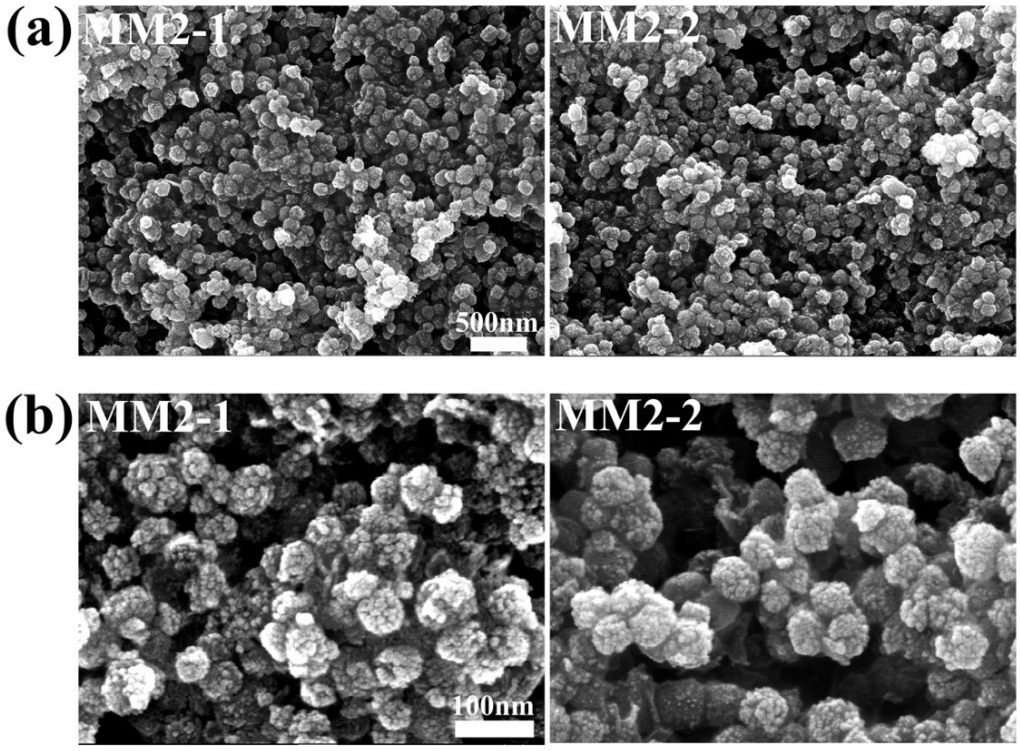

Figure 4-1 SEM images of NPs. (a) Images at a magnification of 30000; (b) Images at a magnification of 1000000.

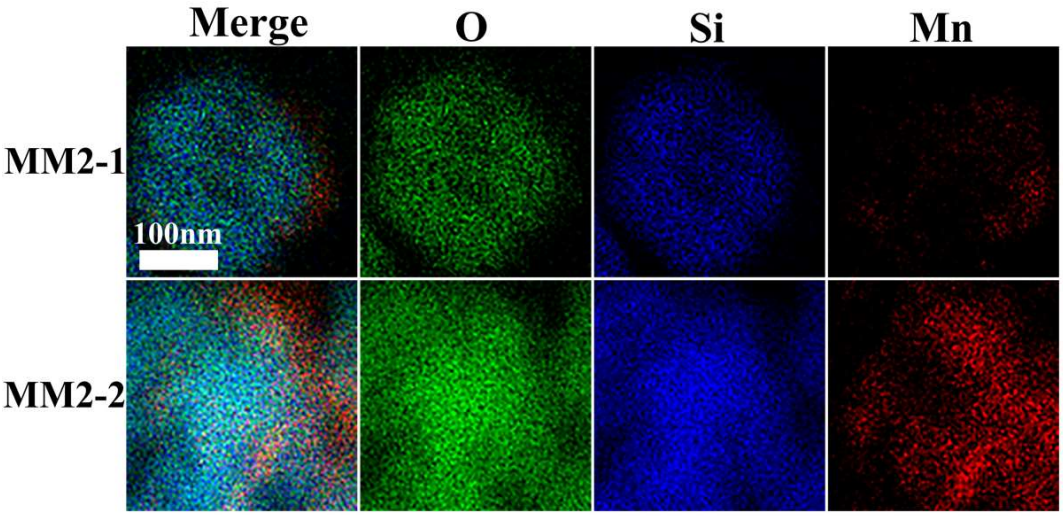

Figure 4-2 Element distribution of NPs.

As shown in the XRD patterns of the NPs (Figure 4-3a), all NPs showed a broad peak between 15 and 30°, which indicated the phase of amorphous silica in MM2. No obvious difference was observed for MM2, MM2-1, and MM2-2. As shown in Figure 4-3b, MM2-1 and MM2-2 showed the same XPS spectra with MM2, indicating the existence of the MnO_2 phase. As shown in the wide-scan XPS spectra (Figure 4-3b), the peak of Si 2p was clearly observed, indicating the presence of the Si element in MM2-1 and MM2-2. This was also confirmed in the high-resolution XPS spectra of Si 2p (Figure 4-3c). In addition, in the wide scan XPS spectra (Figure 4-3b), another peak of Mn 2p was observed, indicating the presence of the Mn element in MM NPs. This was also confirmed by the high-resolution XPS spectra of Mn 2p, as shown in Figure 4-3d.

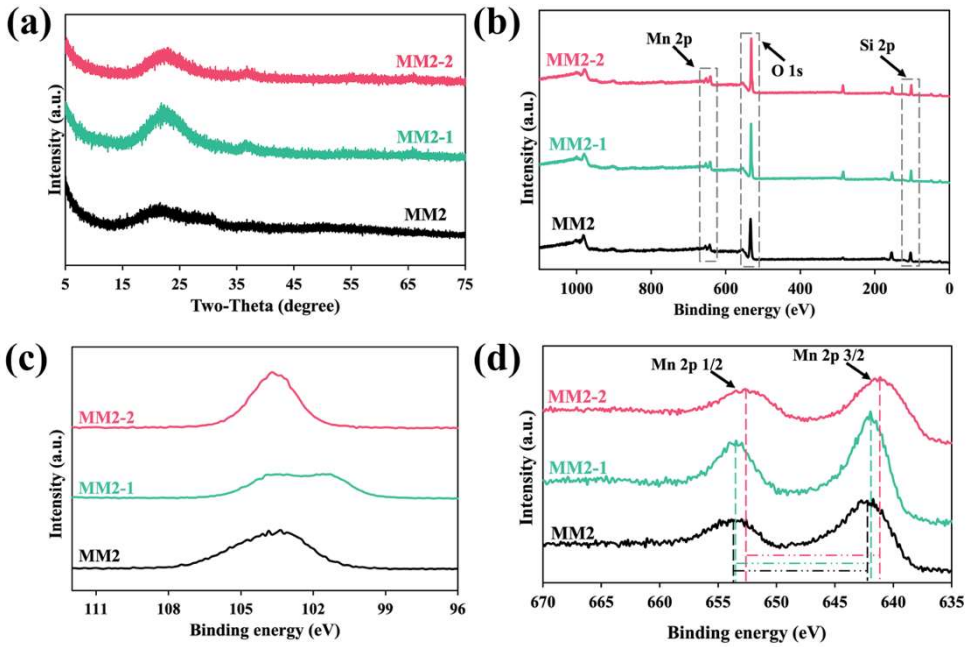

Figure 4-3 The phase and valence analysis. (a) XRD patterns; (b) Wide scan XPS spectra; (c) High-resolution XPS spectra of Si 2p; (d) High-resolution XPS spectra of Mn 2p.

The quantitative analysis of ICP (Table 4-2) showed that MM2-1 and MM2-2 showed the Mn/Si ratio of 0.2 and 0.4, respectively. Additionally, as shown in Table 4-3, MM2-1 and MM2-2 also showed high IR 780 loading efficiency, which was 85.8 ± 4.7% and 74.6 ± 5.9%, respectively.

Table 4-2 Mn/Si ratio from ICP analysis

	MM2-1	MM2-2
Mn/Si ratio	0.2± 0.04	0.4± 0.03

Table 4-3 IR 780 loading efficiency

	IMM1	IMM2
Drug loading efficiency (%)	85.8 ± 4.7	74.6 ± 5.9

4.3.2 photothermal capability of IMM

As shown in Figure 4-4a, IMM induced a slightly higher temperature of solution after being exposed to an 808nm laser than IR 780. After being exposed to an 808nm laser for 10min, IR 780, IMM1, and IMM2 induced an increase in the temperature of solutions by 19 ºC, 22 ºC, and 23 ºC, respectively. Whereas, after being exposed to an 808nm laser for another 3 cycles, a more obvious difference between IR 780, IMM1, and IMM2 was observed, as shown in Figures 4-4(b-d). After 4 cycles of exposure to an 808nm laser for 10min, IR780, IMM1, and IMM2 decreased the temperature

increase in solutions from 19 ºC to 7 ºC, 22 ºC to 13 ºC, and 22 ºC to 24 ºC, respectively. Additionally, IMM1 and IMM2 also showed a better capacity in increasing temperature than IR 780 after stored in darkness for 2 weeks at room temperature, as shown in Figure 4-5.

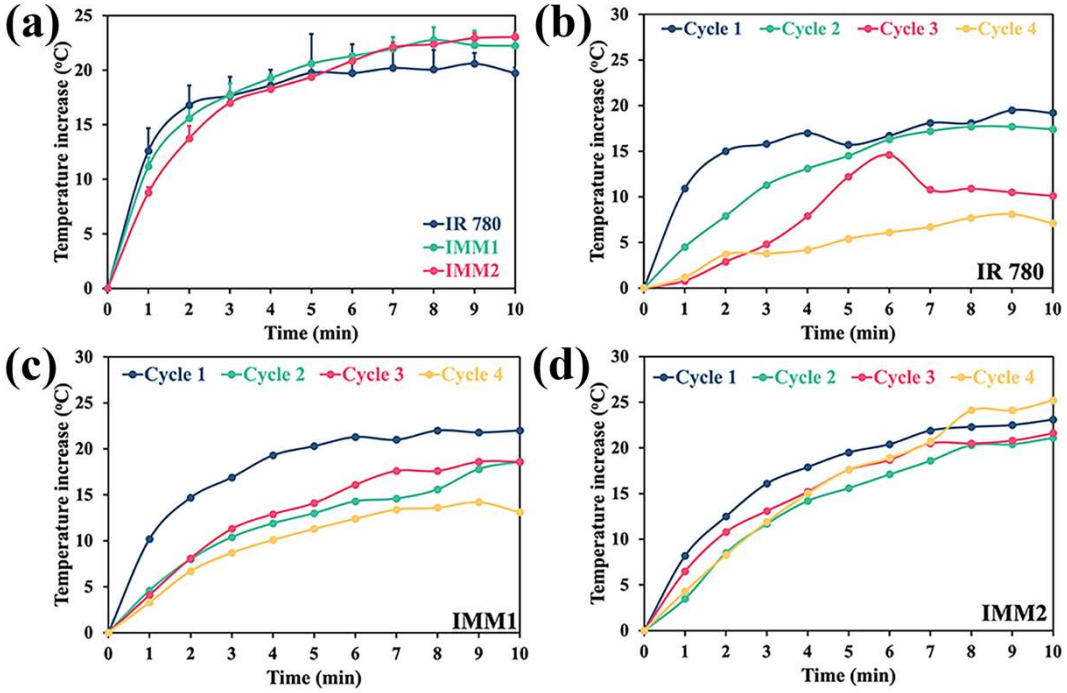

Figure 4-4 Analysis of photothermal capability. (a) The photothermal capability of IMM (n=3); The photothermal capability of (b) IR 780, (c) IMM1, and (d) IMM2 after 4 cycles of laser irradiation.

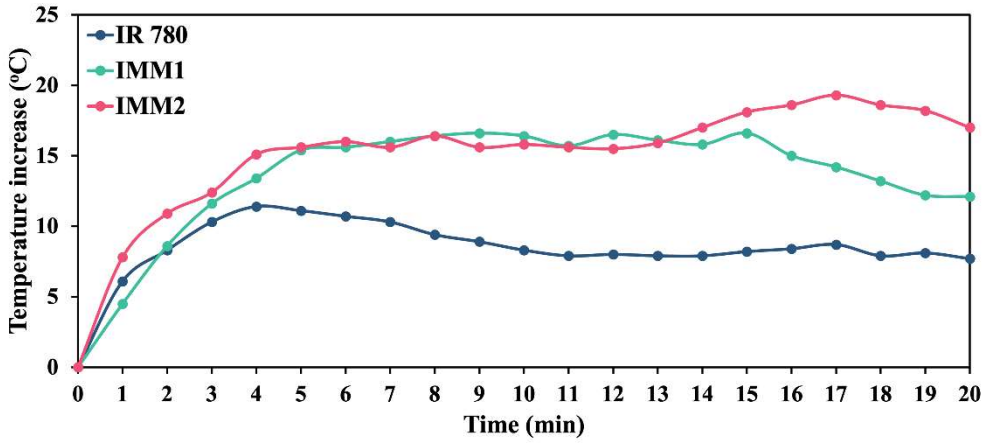

Figure 4-5 The photothermal capability of IMM and IR 780 stored in darkness for 2 weeks at room temperature.

Moreover, the concentration of IR 780 in IMM and the power density of the laser influenced the increase in solution temperature, as shown in Figure 4-6. As shown in Figures 4-6(a-b), with the increase of concentration of IR 780 in IMM from 50 μg/mL to 200 μg/mL, the temperature of the solution after being exposed to an 808nm laser for 10min increased from 13 °C to 23 °C, and 14 °C to 23 °C for IMM1 and IMM2, respectively. As shown in Figures 4-6(c-d), with the increase of power density of laser from 0.5A to 0.75A, the temperature of the solution after being exposed to 808nm laser for 10min increased from 13 °C to 23 °C, and 14 °C to 23 °C for IMM1and IMM2, respectively.

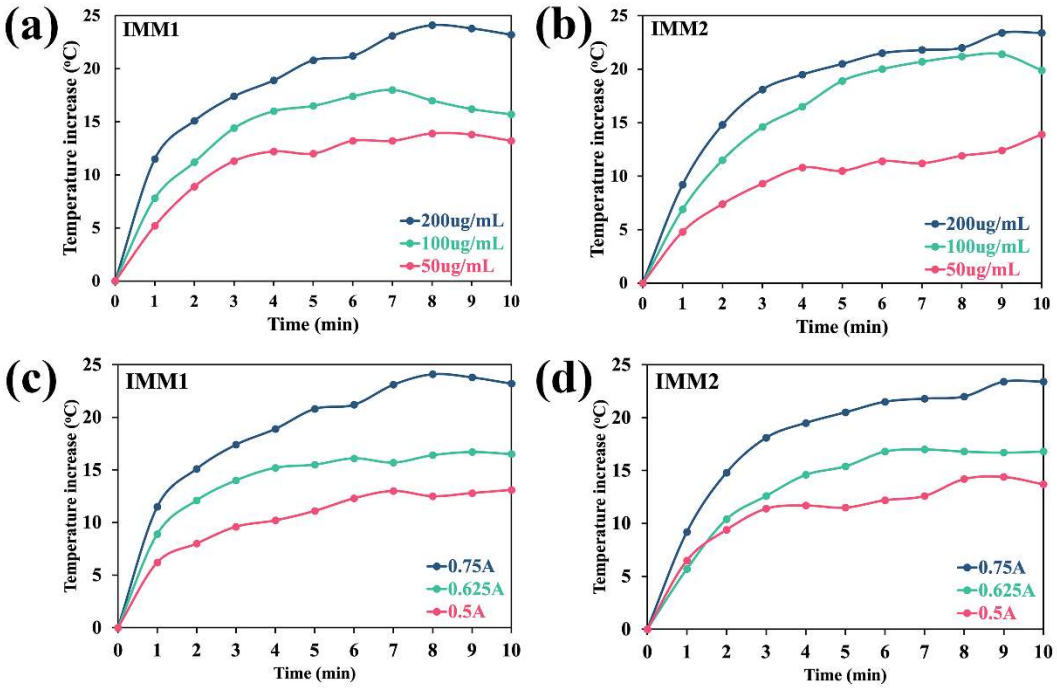

Figure 4-6 Influential factors on the photothermal capability. The photothermal capability of (a) IMM1 and (b) IMM2 with different concentrations of IR 780; The photothermal capability of (c) IMM1 and (d) IMM2 after laser irradiation of different power densities.

4.3.3 Photodynamic capability of IMM

As shown in Figure 4-7a, IMM showed an obviously better capability in the generation of $^1O_2$ after exposure to an 808nm laser than IR 780, which was indicated by the higher fluorescence intensity of SOSG. Firstly, the laser irradiation time showed an obvious influence on the generation of $^1O_2$. With irradiation time increasing from 5min to 10min, IR 780, IMM1, and IMM2 induced an increase in fluorescence intensity of SOSG from 175 to 199, 1518 to 1867, and 771 to 1045, respectively. Moreover, the power density of the laser also influenced the generation of $^1O_2$, as shown in Figure 4-

7b. Increasing the power density from 0.5A to 0.75A induced an increase in the fluorescence intensity of SOSG from 1095 to 1518, and 527 to 771, respectively. Additionally, IMM1 and IMM2 also induced much higher increase in fluorescence intensity of SOSG than IR 780 stored in darkness for 2 weeks at room temperature, as shown in Figure 4-8.

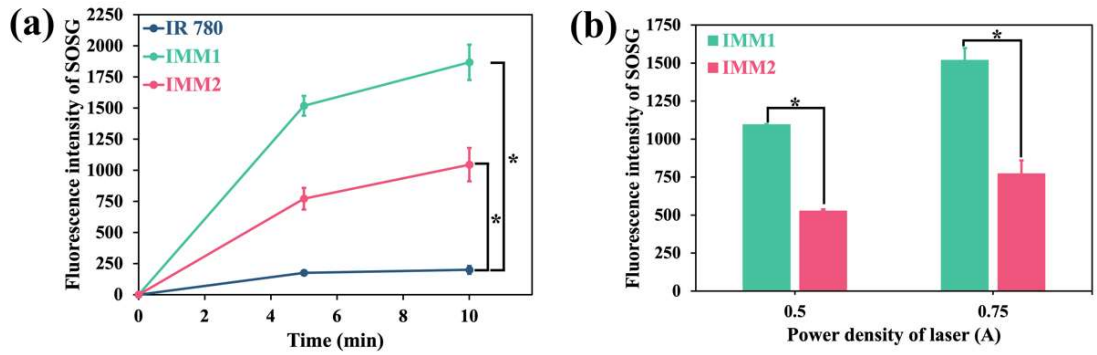

Figure 4-7 Analysis of photodynamic capability. (a) $^1O_2$ generation with different laser irradiation times; (b) $^1O_2$ generation with different laser power densities.

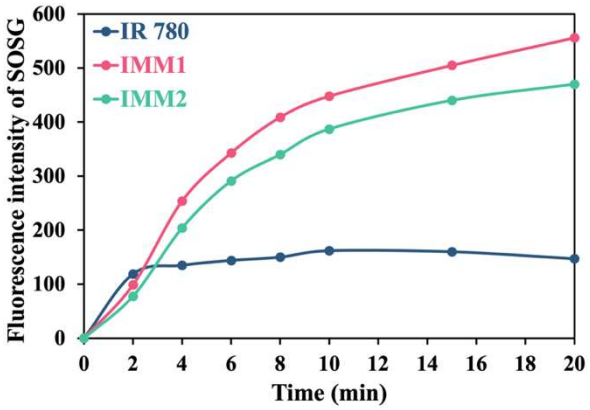

Figure 4-8 The photodynamic capability of IMM and IR 780 stored in darkness for 2 weeks at room temperature.

4.3.4 TME regulation functions

Due to the confirmed TME regulation functions of MM2, IMM were also carefully investigated from different aspects of TME regulation, including oxygenation, Fenton-like reaction-induced •OH generation, and GSH depletion, which were measured with similar methods in Chapter 2 and 3.

(1) As shown in Figure 4-9a, IMM1 and IMM2 induced obvious oxygenation in a concentration-dependent manner. Increasing the concentration of IMM from 0 μg/mL to 200 μg/mL induced a similar decrease in the relative fluorescence intensity of RDPP for IMM1 and IMM2 from 100% to 10%, indicating the increase of O_2 level in solutions. The influence of IMM-induced oxygenation on the photodynamic capability was further investigated through measuring the laser irradiation-induced $^1O_2$ generation in solutions containing H_2O_2. As shown in Figure 4-9b, in the presence of H_2O_2, the IR 780-induced photodynamic capability was very limited and an obvious decrease in the level of $^1O_2$ generated with adding of H_2O_2 was observed. Whereas IMM induced a clear increase in the level of $^1O_2$ generated after adding H_2O_2. And the IMM2 showed a higher increase in the level of $^1O_2$ generated after adding H_2O_2 than IMM1.

(2) The Fenton-like reaction-induced •OH generation was indicated by the degradation of MB as shown in Figure 4-10. IMM induced a slight degradation of MB in the solutions containing H_2O_2, which showed an absorbance peek at 664nm of 0.529, 0.481, and 0.499 for Control, IMM1, and IMM2, respectively. Moreover, IMM1 and

IMM2 showed a much lower absorbance peak at 664nm in the solutions containing H_2O_2 and GSH, which is 0.220, and 0.168, respectively.

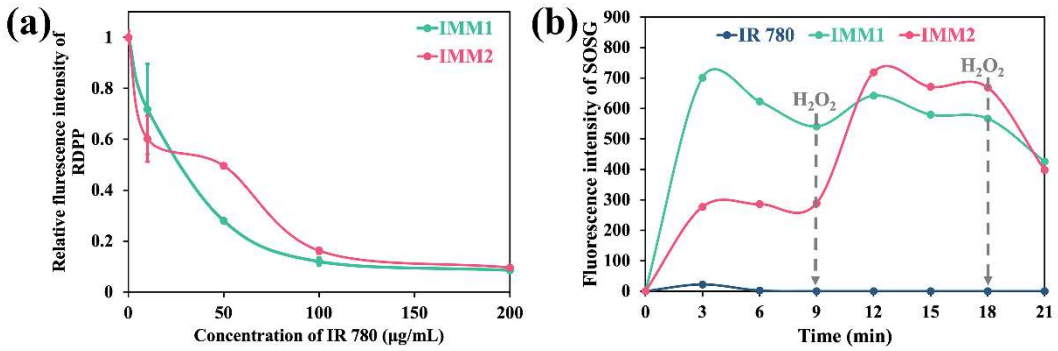

Figure 4-9 TME regulation functions of oxygenation. (a) Oxygenation at different concentrations of IMM; (b) Influence of oxygenation on photodynamic capability.

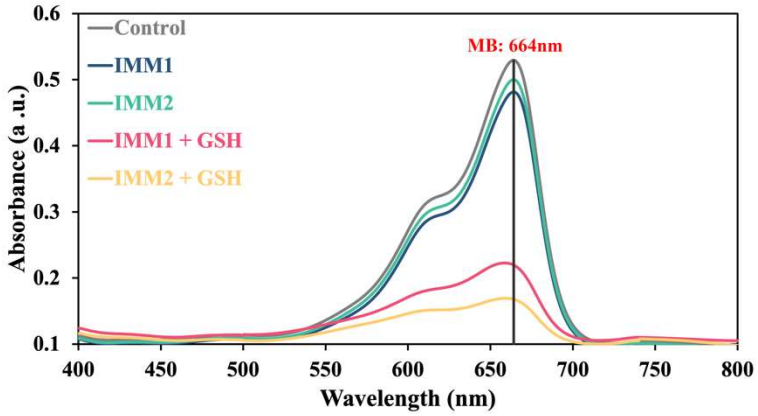

Figure 4-10 TME regulation functions of •OH generation.

(3) The GSH concentration was evaluated through measuring the conversion of DTNB to TNB, which has an absorbance peak at 415nm. As shown in Figure 4-11, GSH showed a high absorbance peak at 415nm, indicating the obvious conversion of DTNB to TNB. After mixing GSH with IR 780, no obvious difference was observed, indicating that IR 780 has no influence on the GSH concentration. Whereas, after

mixing GSH with IMM1 or IMM2, a much lower absorbance peak at 415nm for TNB was observed, suggesting that IMM1 and IMM2 depleted GSH and thus inducing low conversion of DTNB to TNB.

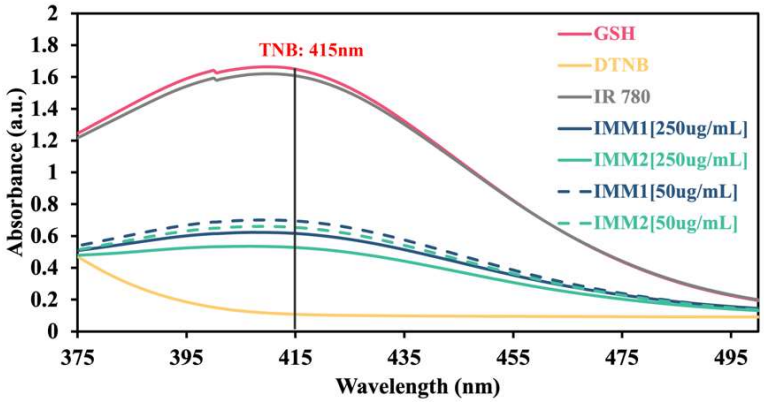

Figure 4-11 GSH depletion induced by IMM with different concentrations

4.3.5 Cell-killing effect

The in vitro phototherapy effect enhanced by IMM was investigated through measuring the cell viability of different cancer cells (MOC and LLC), which were incubated with IMM and IR 780 before being exposed to an 808 nm laser with different power densities and irradiation times.

Compared with IR 780, IMM1 and IMM2 induced higher cell-killing effect after exposure to laser irradiation, as indicated by the live/dead cell staining images in Figure 4-12. Moreover, as shown in Figure 4-13, IMM1 and IMM2 induced higher cell-killing effects to both MOC and LLC after being exposed to an 808nm laser compared with cells without exposure to an 808nm laser. Increasing IMM concentration from 2.5 μg/mL to 10 μg/mL clearly increased the cell-killing effect.

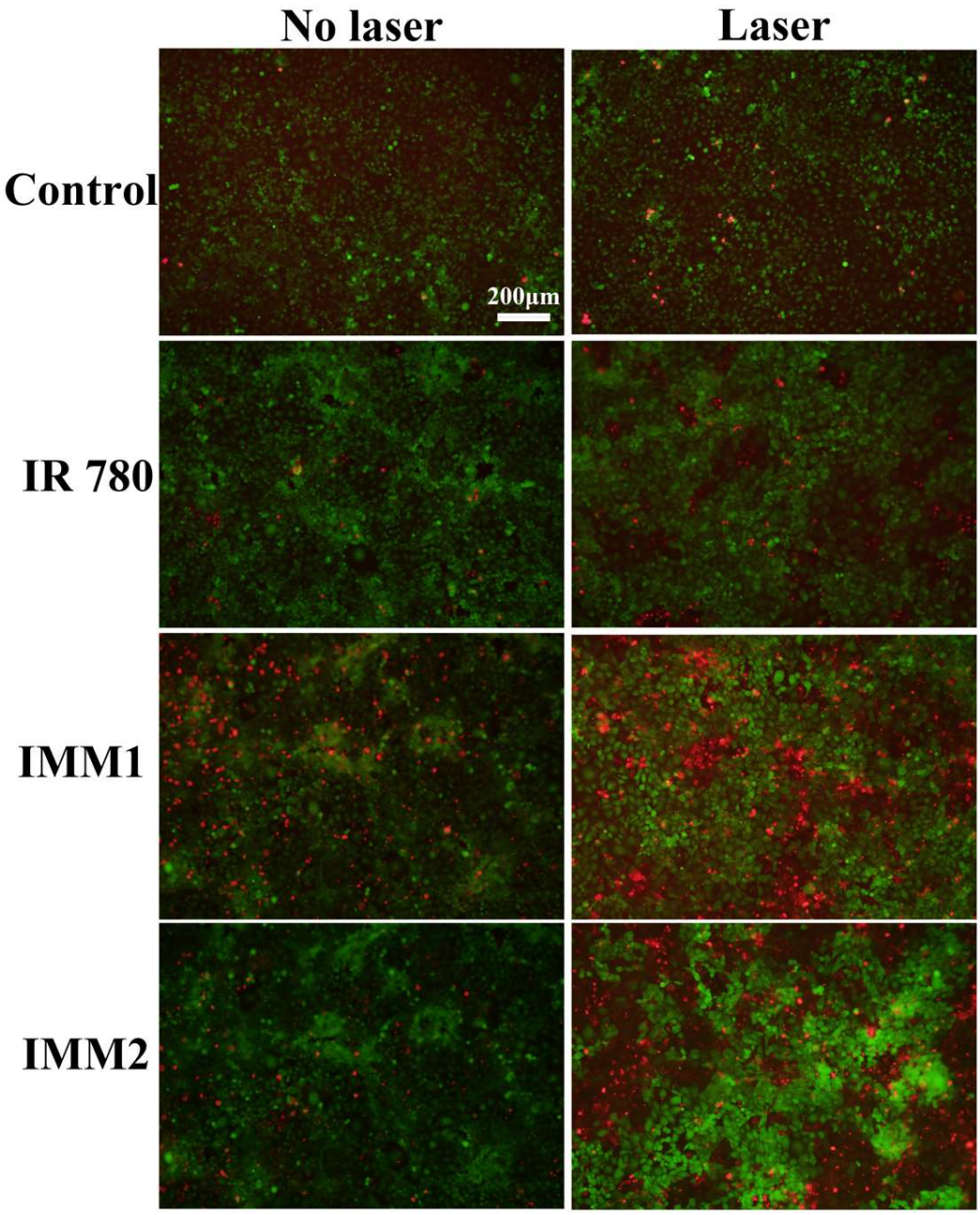

Figure 4-12 Fluorescence images of calcein - AM (green fluorescence) / PI (red fluorescence) - stained MOC cells treated with the combination of an 808nm laser radiation at power density of 0.75A for 10 min and IMM with a concentration of IR 780 at 2.5 μg mL^{-1}

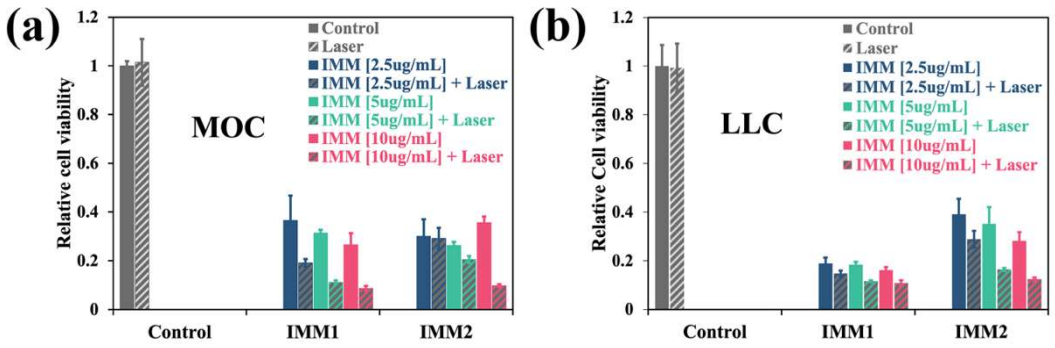

Figure 4-13 In vitro cell-killing effect of IMM with different concentrations of IR 780. (a) In vitro cell-killing effect to MOC; (b) In vitro cell-killing effect to LLC.

4.3.6 In vivo anticancer effect of combinational anticancer therapy of immunotherapy with phototherapy

As shown in Figure 4-14, the combination of an 808nm laser irradiation and IMM obviously enhanced the inhibitory effect on the growth of primary tumors and distant untreated tumors. Firstly, mice treated with the combination of an 808nm laser irradiation and IMM or IR 780 showed obviously inhibited growth of primary tumors on the left leg compared with mice treated with IMM or IR 780 alone, as shown in Figure 4-14b. Moreover, the combination of an 808nm laser irradiation and IMM showed a higher inhibitory effect on primary tumors on the left leg than the combination of an 808nm laser irradiation and IR 780, as shown in Figure 4-14 (b-c). On day 21, mice treated with the combination of an 808nm laser irradiation and IMM1 and the combination of an 808nm laser irradiation and IMM2 both showed a ratio of mice with tumors of 0%. Whereas mice treated with the combination of an 808nm laser irradiation and IR 780 showed a ratio of mice with tumors of 40%, which is obviously higher than

the combination of an 808nm laser irradiation and IMM1 and the combination of an 808nm laser irradiation and IMM2. Secondly, mice treated with the combination of an 808nm laser irradiation and IMM1 and the combination of an 808nm laser irradiation and IMM2 showed a better inhibitory effect on the growth of distant untreated tumors on the right leg compared with mice treated with the combination of an 808nm laser irradiation and IR 780, as shown in Figure 4-14 (d-e). Moreover, mice treated with the combination of an 808nm laser irradiation and IMM2 showed a better inhibitory effect on the growth of distant untreated tumors than mice treated with the combination of an 808nm laser irradiation and IMM1. Additionally, the amounts of cytokine secreted from splenocytes were improved, including IL-6, IL-12, and TNF-α, as shown in Figure 4-15.

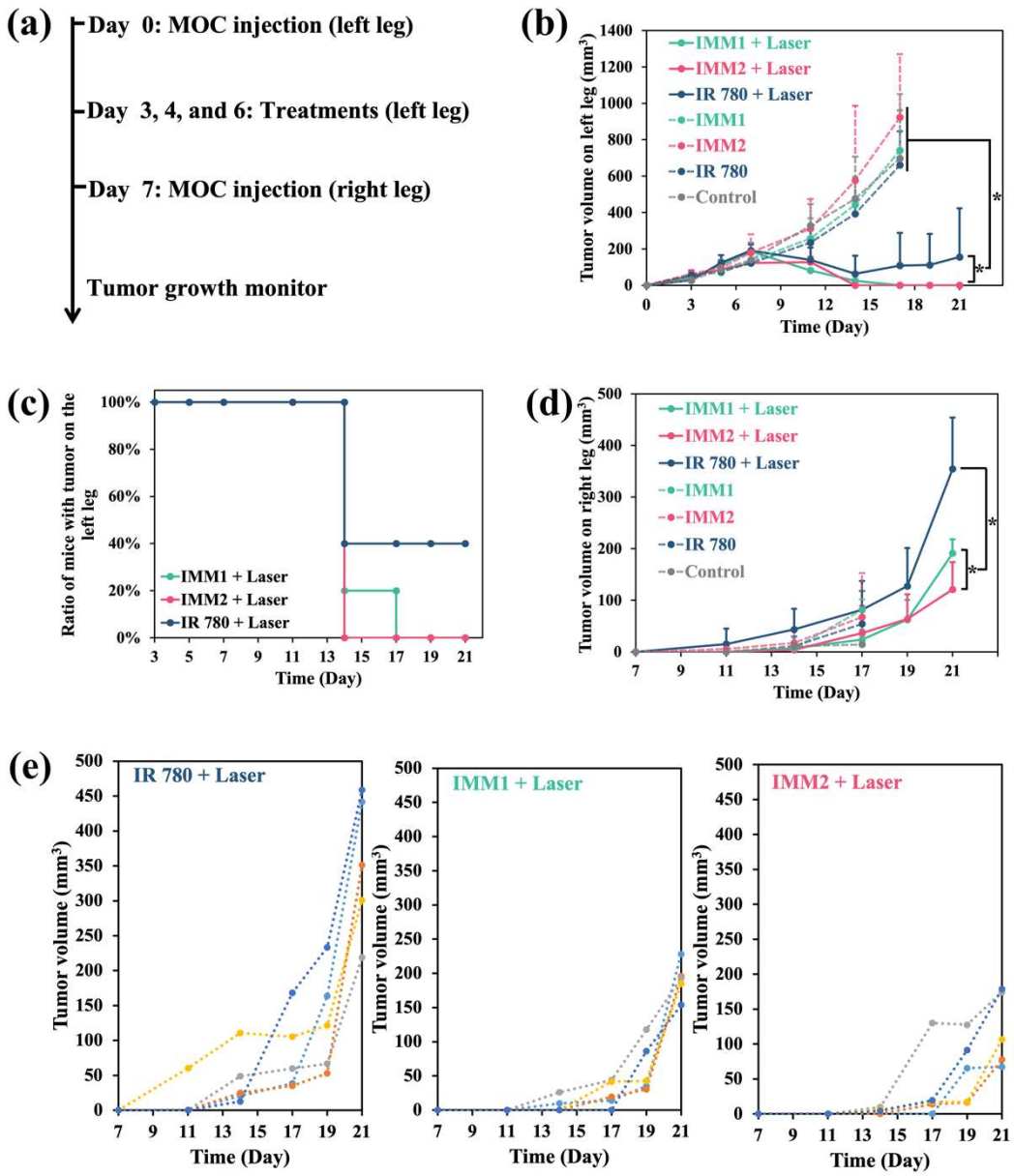

Figure 4-14 In vivo anticancer efficacy of IMM-enhanced Photo-immunotherapy (n = 5). (a) The scheme of the experimental schedule of photo-immunotherapy; (b) Average tumor growth curves of primary tumors in the hind legs on the left side; (c) The ratio of tumor-free mice in the hind legs on the left side; (d) Average tumor growth curves of metastatic tumors in the hind legs on the right side; (e) Corresponding individual growth curves of tumors in the hind legs on the right side.

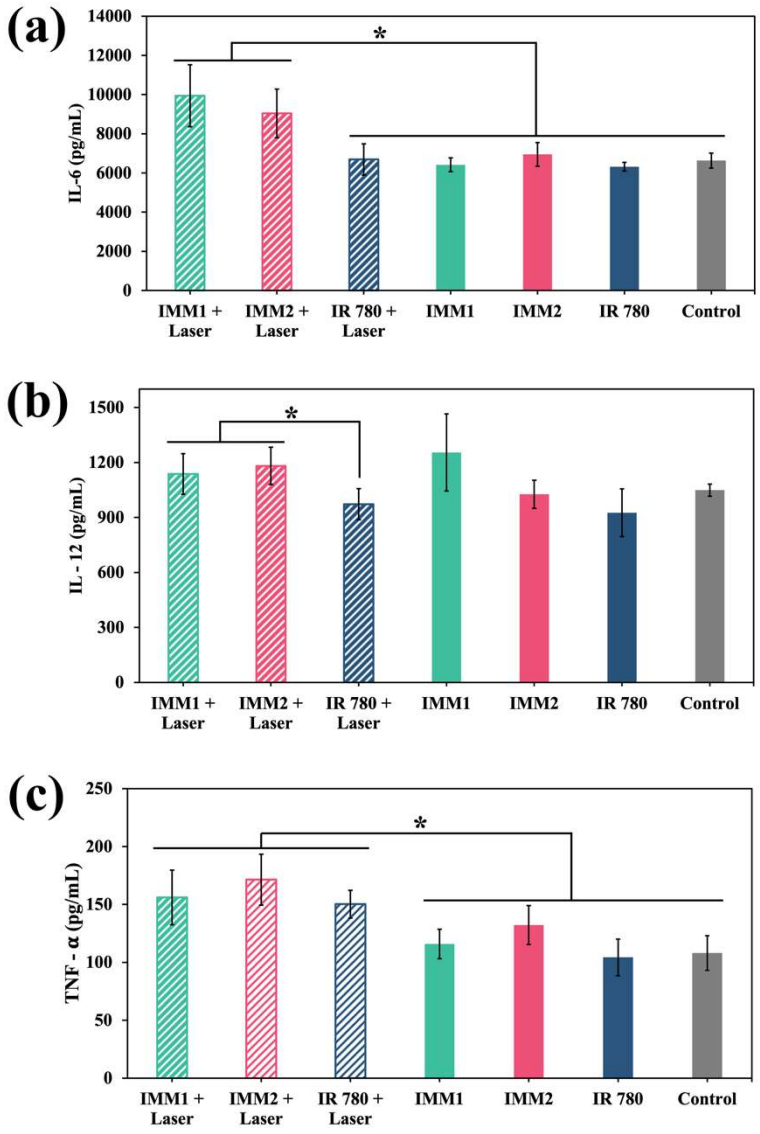

Figure 4-15 Amounts of cytokine secreted from splenocytes in the in vivo experiments (n = 5). (a) IL-6; (b) IL-12; (c) TNF-α.

4.4 Discussion

Based on the results of SEM (Figure 4-1), element mapping (Figure 4-2), XRD and XPS analysis (Figure 4-3), and ICP quantification analysis (Table 4-2), it was obvious that Mn was successfully coated to MM2 through using PEG to reduce $KMnO_4$ and the

content of Mn coated onto MM2 was adjusted through changing the $KMnO_4$ and PEG content during the coating process.

Compared with IR 780 alone, IMM1 and IMM2 loaded with IR 780 showed better photostability. IMM1 and IMM2 showed better photothermal capability, indicated by a much more stable temperature increase after repeated laser irradiation than IR 780 as shown in Figure 4-4. Additionally, IMM1 and IMM2 also showed higher photodynamic capability, indicated by the higher $^1O_2$ level generated after an 808nm laser irradiation than IR 780 as shown in Figure 4-7a. It has been reported that the low photostability due to the easy degradation of PA and PS agents has been one of the obstacles to the clinical application of phototherapy [38]. Therefore, format of IMM1 and IMM2 protected IR 780 from degradation after repeated laser irradiation, thus improving the photostability of IR 780 in heat generation and $^1O_2$ generation. Additionally, the power density and laser irradiation time were important in adjusting the efficiency of phototherapy as shown in Figure 4-6 and Figure 4-7b. The easy adjusting of heat generation and $^1O_2$ generation made the PTT highly controllable.

Moreover, IMM, containing Mn-based nanomaterials, also showed obvious tumor regulation functions, including oxygenation (Figure 4-9), highly cytotoxic ROS of •OH generation (Figure 4-10), and GSH depletion (Figure 4-11):

(1) Oxygenation.

As presented in Figure 4-9a, with the increase in the concentration, an obvious decrease in the RDPP intensity was observed, indicating that IMM increased the O_2

level clearly in a concentration-dependent manner. The IMM-induced oxygenation was attributed to the existence of MnO_2 as shown in XPS analysis results (Figure 4-3). Due to the catalytic activity to H_2O_2 and produce O_2, MnO_2 has been widely applied to relieve hypoxia in TME in different anticancer therapies, which not only limited the efficiency of PDT in generating $^1O_2$ [39], but also influenced the immune responses [40, 41]. IR 780 induced $^1O_2$ generation after exposure to an 808nm laser irradiation through interacting with oxygen [7]. As shown in Figure 4-9b, the oxygenation induced by the reactions between IMM and H_2O_2 improved the efficiency of $^1O_2$ generation. During the period of 0-9min after the first time of H_2O_2 addition, IMM1 induced a high level of $^1O_2$ but an obvious decrease with irradiation time increased, during which H_2O_2 influenced the protection of Mn cover, and the efficiency of IR 780 vindicated by the low generation of $^1O_2$ induced by IR 780. Whereas IMM2 induced a more stable generation of $^1O_2$ with irradiation time increased, which was attributed to the thicker protection of Mn cover. And after the second time of H_2O_2 addition, IMM2 induced a higher level of $^1O_2$ than IMM1 due to the oxygenation induced by the remained Mn cover. The level of $^1O_2$ induced by laser irradiation was reported to determine the efficiency of PDT [40].

(2) ROS generation.

As suggested by Figure 4-10, IMM induced an obvious generation of •OH, and showed a higher level of •OH generated in solutions containing GSH. The reactions between GSH/H^+ and MnO_2 induced the generation of Mn^{2+} which was suggested to

induce CDT and produce ROS (equations 1-3) without limitation from laser irradiation, which is one of the big challenges for the PDT-induced ROS generation [41]. The CDT-induced ROS was generated through utilizing the over-produced H_2O_2 and acidic pH in TME to induce the ion-mediate Fenton reactions or Fenton-like reactions and generate highly cytotoxic ROS of •OH [42]. Compared with other ion-mediate Fenton reactions or Fenton-like reactions, Mn-based nanomaterials possess some advantages. For example, Fe^{2+}-induced Fenton reactions require a pH range of 2~4. whereas, Mn^{2+} was proven to induce Fenton-like reactions in the entire pH range and showed the best catalytic activity at pH 5 [43]. The highly cytotoxic ROS of •OH generation combined with the PDT-induced $^1O_2$ generation enhanced the oxidative damage after laser irradiation [44].

(1) $MnO_2 + GSH \rightarrow Mn^{2+} + GSSG$

(2) $MnO_2 + 2H^+ \rightarrow Mn^{2+} + H_2O + 1/2\ O_2$

(3) $Mn^{2+} + H_2O_2 \rightarrow Mn^{3+} + \bullet OH + OH^-$

3) GSH depletion.

As shown in Figure 4-11, IMM induced an obvious depletion of GSH due to the reaction between MnO_2 and GSH as shown in the above equation (1). GSH, as one of the main antioxidants in TME, was reported to greatly weaken the efficiency of PDT through consuming the $^1O_2$ generated after laser irradiation [45, 46]. The GSH depletion induced by IMM can lead to a decrease in ROS consumption and an increase in ROS level, which also enhanced oxidative damage after laser irradiation.

Based on these properties of IMM, an obvious cell-killing effect (Figure 4-3) and in vivo anticancer effect were observed (Figure 4-14).

In in vitro experiments, an obvious death was observed in cells treated with IMM alone and the combination of an 808nm laser irradiation and IMM. IMM alone induced the Mn-based Fenton-like reactions to generate highly cytotoxic ROS of •OH in MOC and LLC cells and caused an obvious cell-killing effect [32]. The combination of an 808nm laser irradiation and IMM induced a higher cell-killing effect than IMM alone due to the effect of IMM-enhanced phototherapy, including oxygenation, ROS generation, and GSH depletion.

In the bilateral animal model, the combination of an 808nm laser irradiation and IMM induced an obvious inhibitory effect on not only the primary tumors but also distant untreated tumors as shown in Figure 4-14, as well as induced high secretion of cytokines as shown in Figure 4-15. IL-6 is important for the development of antigen-specific cytotoxic T lymphocytes and the memory of cytolytic T cells, and the cytolytic capability of natural killer cells [47, 48]. IL-12 is produced by antigen-presenting cells in mice, which plays an important role in both innate and adaptive lymphoid cells, including natural killer (NK) cells and CD 8+ cytotoxic T lymphocytes [49, 50]. TNF-α is important for cellular communication in many processes, including host defense and inflammation, as well as be related to the DC maturation and CD8+ T cell stimulation and activation of the inflammatory reactions of the innate immune [51].

Compared mice treated with an 808nm laser irradiation with mice treated without an 808nm laser irradiation, an obvious inhibitory effect on the growth of primary tumors on the left leg was observed as shown in Figure 4-4b, suggesting the effectiveness of phototherapy on primary tumors. Moreover, comparing in vivo anticancer effect among mice treated with IMM1, IMM2, and IR 780, mice treated with IMM1 and IMM2 showed a better inhibitory effect on the growth of primary tumors on the left leg, and distant untreated tumors on the right leg, which can be attributed to three factors.

(1) The process of loading IR 780 into MM2 and further blocking IR 780 with another layer of Mn covering protected IR 780 from degradation after an 808nm laser irradiation and showed an enhanced photostability as shown in Figure 4-4. The better photostability endowed IMM1 and IMM2 with better photothermal capability (Figure 4-4) and photodynamic capability (Figure 4-7) than IR 780, which contributed to the enhanced inhibitory effect on the growth of primary tumors.

(2) IMM possessed regulation functions to TME, including oxygenation, Fenton-like reaction-induced ROS generation, and GSH depletion, as shown in results from Figure 4-9 to Figure 4-11. Firstly, PDT efficiency was dependent on laser irradiation, PS agent, and O_2. IMM-induced oxygenation improved the O_2 level (Figure 4-9), which had the potential to lead to a higher generation of ROS of $^1O_2$. Secondly, PDT-induced ROS generation was usually restricted by the tissue penetration depth of laser irradiation [41]. Whereas IMM-induced ROS generation on the basis of Mn-induced Fenton-like reactions can make up this deficiency, which can generate ROS without tissue

penetration depth limitation and produce highly cytotoxic ROS of •OH (Figure 4-10). Thirdly, the GSH in antioxidant systems was reported to consume ROS generated and weaken the efficiency of PDT [46]. Whereas IMM showed obvious GSH depletion capacity as shown in Figure 4-11, which contributed to an indirect increase in the different kinds of ROS levels. In conclusion, the IMM-induced regulation functions to TME from different aspects led to the enhanced oxidative damage of ROS generated from PDT and CDT, which contributed to the enhanced inhibitory effect on the growth of primary tumors.

(3) Si/Mn-based nanomaterials were reported to activate immune responses [17-24, 33-37]. Although PTT and PDT were proven to induce ICD and activate immune responses, their effects were still far from satisfaction [4, 14]. Interestingly, Si/Mn-based nanomaterials showed potential in activating immune responses. In previous studies, Si-based nanomaterials were found to influence macrophage polarization and further influence immune responses, upregulate the level of MHC-II, CD 80, and CD 86 in DCs, and activate p38 and NF-κB. And Mn-based nanomaterials were found to enhance the activation of the cGAS/STING pathway through stimulating cGAS to synthesize 2′3′ - cyclic GMP-AMP (cGAMP) and augmenting cGAMP-STING binding affinity. The immune activation efficiency of Mn-Si composite nanomaterials was also proven in chapter 2 and 3, which showed an obvious inhibitory effect on the distant untreated tumors when combined with RT and chemotherapy. Additionally, IMM-induced regulation functions to TME also contributed to the activation of immune

responses. Hypoxia was reported to induce an immunosuppressive TME, which can induce cellular responses of the HIF activation to further induce the recruitment of tumor-associated macrophage, and the suppression of cytotoxic CD 8-T and NK cells [52], and form the acidic pH value of TME due to the lactic accumulation from hypoxia-induced glycolysis to impedes the normal immune cells [53]. ROS also played an important role in immune responses, which was reported to promote the maturation of DCs, induce the activation and proliferation of effector T cells, and cause ICD [54, 55]. The immune activation induced by phototherapy, Mn-Si-based nanomaterials, and regulated TME synergistically contributed to enhance the inhibitory effect on the growth of primary tumors and distant untreated tumors.

4.5 Conclusions

In this work, IR 780 was loaded into Mn-doped MSNs (MM2) and further blocked by another layer of Mn covering, which formed the IMM and applied to the combinational anticancer therapies of immunotherapy with phototherapy. Compared with IR 780, IMM showed better photostability, which induced better photothermal capability and photodynamic capability. Moreover, IMM regulated TME to a status beneficial for the combinational anticancer therapies of immunotherapy with phototherapy through producing O_2 in situ to relieve hypoxia and generating •OH and depleting GSH to increase ROS levels. Notably, the combination of an 808nm laser irradiation and IMM not only inhibited the growth of primary tumors, but also

suppressed the growth of distant untreated tumors. Taken together, these results demonstrated that the application of IMM may provide an effective choice for the combinational anticancer therapy of immunotherapy and phototherapy. However, further research studies to analyze in detail the mechanism by which IMM functions in the combinational anticancer therapy of immunotherapy and phototherapy are required.

Reference

1. Zaimy M, Saffarzadeh N, Mohammadi A, Pourghadamyari H, Izadi P, Sarli A, Moghaddam L, Paschepari S, Azizi H, Torkamandi S: **New methods in the diagnosis of cancer and gene therapy of cancer based on nanoparticles**. *Cancer Gene Therapy* 2017, **24**(6):233-243.
2. Abrahamse H, Kruger CA, Kadanyo S, Mishra A: **Nanoparticles for advanced photodynamic therapy of cancer**. *Photomedicine and laser surgery* 2017, **35**(11):581-588.
3. Zhu H, Cheng P, Chen P, Pu K: **Recent progress in the development of near-infrared organic photothermal and photodynamic nanotherapeutics**. *Biomaterials science* 2018, **6**(4):746-765.
4. Zou J, Li L, Yang Z, Chen X: **Phototherapy meets immunotherapy: A win–win strategy to fight against cancer**. *Nanophotonics* 2021.
5. Cheng L, Wang C, Feng L, Yang K, Liu Z: **Functional nanomaterials for phototherapies of cancer**. *Chemical reviews* 2014, **114**(21):10869-10939.
6. Shibu ES, Hamada M, Murase N, Biju V: **Nanomaterials formulations for photothermal and photodynamic therapy of cancer**. *Journal of Photochemistry and Photobiology C: Photochemistry Reviews* 2013, **15**:53-72.
7. Dolmans DE, Fukumura D, Jain RK: **Photodynamic therapy for cancer**. *Nature reviews cancer* 2003, **3**(5):380-387.
8. Dewey WC: **Arrhenius relationships from the molecule and cell to the clinic**.

International journal of hyperthermia 1994, **10**(4):457-483.

9. Xie Z, Fan T, An J, Choi W, Duo Y, Ge Y, Zhang B, Nie G, Xie N, Zheng T: **Emerging combination strategies with phototherapy in cancer nanomedicine**. *Chemical Society Reviews* 2020, **49**(22):8065-8087.

10. Zhu X, Feng W, Chang J, Tan Y-W, Li J, Chen M, Sun Y, Li F: **Temperature-feedback upconversion nanocomposite for accurate photothermal therapy at facile temperature**. *Nature communications* 2016, **7**(1):1-10.

11. Schroeder A, Heller DA, Winslow MM, Dahlman JE, Pratt GW, Langer R, Jacks T, Anderson DG: **Treating metastatic cancer with nanotechnology**. *Nature Reviews Cancer* 2012, **12**(1):39-50.

12. Kaczmarek A, Vandenabeele P, Krysko DV: **Necroptosis: the release of damage-associated molecular patterns and its physiological relevance**. *Immunity* 2013, **38**(2):209-223.

13. Panzarini E, Inguscio V, Fimia GM, Dini L: **Rose Bengal acetate photodynamic therapy (RBAc-PDT) induces exposure and release of damage-associated molecular patterns (DAMPs) in human HeLa cells**. *PloS one* 2014, **9**(8):e105778.

14. Yagawa Y, Tanigawa K, Kobayashi Y, Yamamoto M: **Cancer immunity and therapy using hyperthermia with immunotherapy, radiotherapy, chemotherapy, and surgery**. *Journal of Cancer Metastasis and Treatment* 2017, **3**:218-230.

15. Haynes NM, van der Most RG, Lake RA, Smyth MJ: **Immunogenic anti-cancer chemotherapy as an emerging concept**. *Current opinion in immunology* 2008, **20**(5):545-557.

16. Zhou S, Zhong Q, Wang Y, Hu P, Zhong W, Huang C-B, Yu Z-Q, Ding C-D, Liu H, Fu J: **Chemically engineered mesoporous silica nanoparticles-based intelligent delivery systems for theranostic applications in multiple cancerous/non-cancerous diseases**. *Coordination Chemistry Reviews* 2022, **452**:214309.

17. Wang X, Li X, Yoshiyuki K, Watanabe Y, Sogo Y, Ohno T, Tsuji NM, Ito A: **Comprehensive Mechanism Analysis of Mesoporous-Silica-Nanoparticle-Induced Cancer Immunotherapy**. *Advanced healthcare materials* 2016, **5**(10):1169-1176.

18. Wang X, Li X, Ito A, Yoshiyuki K, Sogo Y, Watanabe Y, Yamazaki A, Ohno T, Tsuji NM: **Hollow structure improved anti-cancer immunity of mesoporous silica nanospheres in vivo**. *Small* 2016, **12**(26):3510-3515.

19. Wang X, Li X, Ito A, Watanabe Y, Sogo Y, Tsuji NM, Ohno T: **Stimulation of in vivo antitumor immunity with hollow mesoporous silica nanospheres**. *Angewandte Chemie* 2016, **128**(5):1931-1935.

20. Wang X, Li X, Ito A, Sogo Y, Watanabe Y, Tsuji NM, Ohno T: **Biodegradable metal ion-doped mesoporous silica nanospheres stimulate anticancer Th1 immune response in vivo**. *ACS applied materials & interfaces* 2017,

9(50):43538-43544.

21. Wang X, Li X, Ito A, Sogo Y, Watanabe Y, Hashimoto K, Yamazaki A, Ohno T, Tsuji NM: **Synergistic effects of stellated fibrous mesoporous silica and synthetic dsRNA analogues for cancer immunotherapy**. *Chemical Communications* 2018, **54**(9):1057-1060.

22. Wang X, Li X, Ito A, Sogo Y, Ohno T: **Pore size-dependent immunogenic activity of mesoporous silica-based adjuvants in cancer immunotherapy**. *Journal of Biomedical Materials Research Part A: An Official Journal of The Society for Biomaterials, The Japanese Society for Biomaterials, and The Australian Society for Biomaterials and the Korean Society for Biomaterials* 2014, **102**(4):967-974.

23. Wang X, Li X, Ito A, Sogo Y, Ohno T: **Particle-size-dependent toxicity and immunogenic activity of mesoporous silica-based adjuvants for tumor immunotherapy**. *Acta biomaterialia* 2013, **9**(7):7480-7489.

24. Wang X, Ihara S, Li X, Ito A, Sogo Y, Watanabe Y, Tsuji NM, Yamazaki A: **Si-doping increases the adjuvant activity of hydroxyapatite nanorods**. *Colloids and Surfaces B: Biointerfaces* 2019, **174**:300-307.

25. Li X, Zhang X, Zhao Y, Sun L: **Fabrication of biodegradable Mn-doped mesoporous silica nanoparticles for pH/redox dual response drug delivery**. *Journal of Inorganic Biochemistry* 2020, **202**:110887.

26. Yu X, Wang X, Yamazaki A, Li X: **Tumor microenvironment-regulated**

nanoplatforms for the inhibition of tumor growth and metastasis in chemo-immunotherapy. *Journal of Materials Chemistry B* 2022, **10**(19):3637-3647.

27. Zhu W, Dong Z, Fu T, Liu J, Chen Q, Li Y, Zhu R, Xu L, Liu Z: **Modulation of hypoxia in solid tumor microenvironment with MnO2 nanoparticles to enhance photodynamic therapy**. *Advanced Functional Materials* 2016, **26**(30):5490-5498.

28. Prasad P, Gordijo CR, Abbasi AZ, Maeda A, Ip A, Rauth AM, DaCosta RS, Wu XY: **Multifunctional albumin–MnO2 nanoparticles modulate solid tumor microenvironment by attenuating hypoxia, acidosis, vascular endothelial growth factor and enhance radiation response**. *ACS nano* 2014, **8**(4):3202-3212.

29. Tang H, Li C, Zhang Y, Zheng H, Cheng Y, Zhu J, Chen X, Zhu Z, Piao J-G, Li F: **Targeted Manganese doped silica nano GSH-cleaner for treatment of Liver Cancer by destroying the intracellular redox homeostasis**. *Theranostics* 2020, **10**(21):9865.

30. Yu X, Wang X, Sun L, Yamazaki A, Li X: **Tumor microenvironment regulation-enhanced radio-immunotherapy**. *Biomaterials Advances* 2022:212867.

31. Lin LS, Song J, Song L, Ke K, Liu Y, Zhou Z, Shen Z, Li J, Yang Z, Tang W: **Simultaneous Fenton-like ion delivery and glutathione depletion by MnO2-based nanoagent to enhance chemodynamic therapy**. *Angewandte Chemie*

2018, **130**(18):4996-5000.

32. Gao F, Sun M, Zhang J, Chang Y, Gao W, Ma G, Ma X, Guo Y: **Fenton-like reaction and glutathione depletion by chiral manganese dioxide nanoparticles for enhanced chemodynamic therapy and chemotherapy**. *Journal of Colloid and Interface Science* 2022, **616**:369-378.

33. Lv M, Chen M, Zhang R, Zhang W, Wang C, Zhang Y, Wei X, Guan Y, Liu J, Feng K: **Manganese is critical for antitumor immune responses via cGAS-STING and improves the efficacy of clinical immunotherapy**. *Cell research* 2020, **30**(11):966-979.

34. Wang C, Guan Y, Lv M, Zhang R, Guo Z, Wei X, Du X, Yang J, Li T, Wan Y: **Manganese increases the sensitivity of the cGAS-STING pathway for double-stranded DNA and is required for the host defense against DNA viruses**. *Immunity* 2018, **48**(4):675-687. e677.

35. Song Y, Liu Y, Teo HY, Hanafi ZB, Mei Y, Zhu Y, Chua YL, Lv M, Jiang Z, Liu H: **Manganese enhances the antitumor function of CD8+ T cells by inducing type I interferon production**. *Cellular & Molecular Immunology* 2021, **18**(6):1571-1574.

36. Wang C, Sun Z, Zhao C, Zhang Z, Wang H, Liu Y, Guo Y, Zhang B, Gu L, Yu Y: **Maintaining manganese in tumor to activate cGAS-STING pathway evokes a robust abscopal anti-tumor effect**. *Journal of Controlled Release* 2021, **331**:480-490.

37. Hou L, Tian C, Yan Y, Zhang L, Zhang H, Zhang Z: **Manganese-based nanoactivator optimizes cancer immunotherapy via enhancing innate immunity**. *ACS nano* 2020, **14**(4):3927-3940.

38. Lu Y-J, Chuang C-C, Chen J-P: **Liposomal IR-780 as a Highly Stable Nanotheranostic Agent for Improved Photothermal/Photodynamic Therapy of Brain Tumors by Convection-Enhanced Delivery**. *Cancers* 2021, **13**(15):3690.

39. Wan Y, Fu LH, Li C, Lin J, Huang P: **Conquering the hypoxia limitation for photodynamic therapy**. *Advanced Materials* 2021, **33**(48):2103978.

40. Ma S, Zhou J, Zhang Y, Yang B, He Y, Tian C, Xu X, Gu Z: **An oxygen self-sufficient fluorinated nanoplatform for relieved tumor hypoxia and enhanced photodynamic therapy of cancers**. *ACS applied materials & interfaces* 2019, **11**(8):7731-7742.

41. Wang P, Liang C, Zhu J, Yang N, Jiao A, Wang W, Song X, Dong X: **Manganese-based nanoplatform as metal ion-enhanced ROS generator for combined chemodynamic/photodynamic therapy**. *ACS applied materials & interfaces* 2019, **11**(44):41140-41147.

42. Tang Z, Liu Y, He M, Bu W: **Chemodynamic therapy: tumour microenvironment-mediated Fenton and Fenton-like reactions**. *Angewandte Chemie International Edition* 2019, **58**(4):946-956.

43. Urandur S, Banala VT, Shukla RP, Gautam S, Marwaha D, Rai N, Sharma M,

Sharma S, Ramarao P, Mishra PR: **Theranostic lyotropic liquid crystalline nanostructures for selective breast cancer imaging and therapy**. *Acta Biomaterialia* 2020, **113**:522-540.

44. Liu Y, Zhen W, Jin L, Zhang S, Sun G, Zhang T, Xu X, Song S, Wang Y, Liu J: **All-in-one theranostic nanoagent with enhanced reactive oxygen species generation and modulating tumor microenvironment ability for effective tumor eradication**. *ACS nano* 2018, **12**(5):4886-4893.

45. Jiang F, Robin A, Katakowski M, Tong L, Espiritu M, Singh G, Chopp M: **Photodynamic therapy with photofrin in combination with Buthionine Sulfoximine (BSO) of human glioma in the nude rat**. *Lasers in medical science* 2003, **18**(3):128-133.

46. Fan H, Yan G, Zhao Z, Hu X, Zhang W, Liu H, Fu X, Fu T, Zhang XB, Tan W: **A smart photosensitizer–manganese dioxide nanosystem for enhanced photodynamic therapy by reducing glutathione levels in cancer cells**. *Angewandte Chemie International Edition* 2016, **55**(18):5477-5482.

47. Galandrini R, Cernetti C, Albi N, Dembech C, Terenzi A, Grignani F, Velardi A: **Interleukin-6 is constitutively produced by human CTL clones and is required to maintain their cytolytic function**. *Cellular immunology* 1991, **138**(1):11-23.

48. Bass H, Yamashita N, Clement L: **Heterogeneous mechanisms of human cytotoxic T lymphocyte generation. II. Differential effects of IL-6 on the**

helper cell-independent generation of CTL from CD8+ precursor subpopulations. *The Journal of Immunology* 1993, **151**(6):2895-2903.

49. Dunn GP, Koebel CM, Schreiber RD: **Interferons, immunity and cancer immunoediting**. *Nature Reviews Immunology* 2006, **6**(11):836-848.

50. Colombo MP, Trinchieri G: **Interleukin-12 in anti-tumor immunity and immunotherapy**. *Cytokine & growth factor reviews* 2002, **13**(2):155-168.

51. Locksley RM, Killeen N, Lenardo MJ: **The TNF and TNF receptor superfamilies: integrating mammalian biology**. *Cell* 2001, **104**(4):487-501.

52. Peng G, Liu Y: **Hypoxia-inducible factors in cancer stem cells and inflammation**. *Trends in pharmacological sciences* 2015, **36**(6):374-383.

53. Lardner A: **The effects of extracellular pH on immune function**. *Journal of leukocyte biology* 2001, **69**(4):522-530.

54. Green DR, Ferguson T, Zitvogel L, Kroemer G: **Immunogenic and tolerogenic cell death**. *Nature Reviews Immunology* 2009, **9**(5):353-363.

55. Xiong Y, Xiao C, Li Z, Yang X: **Engineering nanomedicine for glutathione depletion-augmented cancer therapy**. *Chemical Society Reviews* 2021, **50**(10):6013-6041.

Chapter 5 General Summary

The present thesis described the applications of Mn-Si-based nanomaterials to the combinational anticancer therapies of immunotherapy and different anticancer therapies, including RT, chemotherapy, and phototherapy. The in vitro regulation functions to TME and immune activation capability, and in vivo anticancer effect of inhibiting the growth of primary tumors and distant untreated tumors were carefully investigated. The contents of each chapter are summarized as follows.

In chapter 2, Mn-coated SiO_2 NPs (SM NPs) were synthesized to enhance the combinational anticancer therapy of immunotherapy and radiotherapy. SM NPs showed obvious regulation functions to TME, induced higher DNA damage levels and cell-killing effects, and enhanced cytokine secretion. In a bilateral animal model, the combinational treatment of radiation and SM NPs and the combinational treatment of radiation, SM NPs, and the anti-CTLA-4 antibody showed a better inhibitory effect on the growth of primary tumors and distant untreated tumors than the single treatment of radiation and the combinational treatment of radiation and the anti-CTLA-4 antibody, respectively.

In chapter 3, Mn-doped MSNs (MM NPs) were synthesized to enhance the combinational anticancer therapy of immunotherapy and chemotherapy. Mn-doping endowed MSNs with regulation functions to TME, enhanced the immune activation capacity of MSNs, and improved the degradation of MSNs, one of the limitation of MSNs' application to clinical use. In a bilateral animal model, the combinational

treatment of DOX, MM NPs, and the anti-CTLA-4 antibody showed a better inhibitory effect on the growth of primary tumors and distant untreated tumors than the combinational treatment of DOX and the anti-CTLA-4 antibody.

In chapter 4, MM NPs loaded with phototherapy agent of IR 780 and covered with Mn (IMM) were synthesized to enhance the combinational anticancer therapy of immunotherapy and phototherapy. IMM improved the photostability of IR 780 and showed more stable photothermal capability and more efficient photodynamic capability. Additionally, IMM showed obvious regulation functions to TME. In a bilateral animal model, the combinational treatment of an 808nm laser irradiation and IMM showed a better inhibitory effect on the growth of primary tumors and distant untreated tumors than the combinational treatment of an 808nm laser irradiation and IR 780.

On the basis of the findings obtained from the works mentioned above, it is concluded that Mn-Si-based nanomaterials enhanced the anticancer effect of the combinational anticancer therapy of immunotherapy and other kinds of exiting anticancer therapies. Mn-Si-based nanomaterials showed regulation functions to TME, which limited the effect of many exiting anticancer therapies. Moreover, Mn-Si-based nanomaterials showed the capacity of activating immune responses, which enhanced the limited immune responses activated by anticancer therapies themselves. The regulation functions to TME and activation of immune responses synergistically contributed to the enhanced in vivo anticancer effect on inhibiting the growth of

primary tumors and distant untreated tumors. Therefore, the application of Mn-Si-based nanomaterials to the combinational anticancer therapy of immunotherapy and other kinds of anticancer therapies can provide a potential strategy to enhance the exiting anticancer therapies' effect on the primary tumors' growth and metastasis.

Figure List

Table List

Acknowledgements

Time flies. I have been living in Japan for three and a half years. It was really an unforgettable experience in my life. Sincerely, life has been very tough for everyone since the pandemic of Covid-19. For me, too. Because it was the first time for me to separate from my family for such a long time without meeting them in person. Fortunately, I had good teachers, colleagues, and friends and I got understanding and support from my family. Thanks to them being with me throughout, I could finish my thesis.

Firstly, the works in the present thesis were carried out under the direction of Professor Atsushi Yamazaki at the Department of Earth Sciences, Resources and Environmental Engineering, Graduate School of Creative Science and Engineering, Waseda University. I would like to express my deepest appreciation to Professor Atsushi Yamazaki for giving me the opportunity to study further in research, and also for his patient guidance and valuable advice.

Secondly, I would like to express my special gratitude to Chief Senior Researcher Xiupeng Wang at Health and Medical Research Institute, National Institute of Advanced Industrial Science and Technology (AIST) for his relentless efforts in training and guiding me with great patience. I would also like to express my gratitude to Researcher Lue Sun at Health and Medical Research Institute, AIST and Senior Researcher Xia Li at Smart Polymers Group, National Institute for Materials Science (NIMS) for their helpful advice and comment. Also, I would like to express my

gratitude to all the researchers and staff at Health and Medical Research Institute, AIST for their assistance.

Thirdly, I am also thankful to all my friends for their company, care, and encouragement when I was worried about my life and studies in Japan. And I want to say thanks to Ken Mace for his general English advice.

Finally, I would like to express my hearty gratitude to my family for believing in me, supporting me, and encouraging me throughout all my life.

February 2023

Xueping Yu

List of research achievements for application of Doctor of Engineering, Waseda University

Full Name : 余　雪萍　　seal or signature YU XUEPING

Date Submitted(yyyy/mm/dd): 2023/1/30

種類別 (By Type)	題名、 発表・発行掲載誌名、 発表・発行年月、 連名者（申請者含む） (theme, journal name, date & year of publication, name of authors inc. yourself)
Academic papers	○"Tumor microenvironment regulation - enhanced radio - immunotherapy", Biomaterials Advances, July 2022, Volume 138, 212867. Xueping Yu, Xiupeng Wang, Lue Sun, Atsushi Yamazaki, Xia Li.
Academic papers	○"Tumor microenvironment-regulated nanoplatforms for the inhibition of tumor growth and metastasis in chemo-immunotherapy". Journal of Materials Chemistry B, March 2022, Volume 10, Issue 19, 3637-3647. Xueping Yu, Xiupeng Wang, Atsushi Yamazaki, Xia Li.
Lectures	"Tumor Microenvironment-Responsive Radiotherapy", The 43rd Annual Meeting of the Japanese Society for Biomaterials and the 8th Asian Biomaterials Congress,2021. Xueping Yu, Atsushi Yamazaki, Xiupeng Wang. [AO-2E22]
Lectures	"Manganese-based Tumor Microenvironment-Responsive Radiotherapy", Tsukuba Biomedical Engineering Forum 2022, 2022. Xueping Yu, Atsushi Yamazaki, Xiupeng Wang. [O-C-16]
Lectures	"Manganese-doped mesoporous silica for chemotherapy and immunotherapy", Annual Meeting 2022 of The Ceramic Society of Japan, 2022. Xueping Yu, Atsushi Yamazaki, Xiupeng Wang. [3F03]
Lectures	"Tumor microenvironment regulation-enhanced photo-immunotherapy", Tsukuba Biomedical Engineering Forum 2023, 2023. Xueping Yu, Xiupeng Wang, Atsushi Yamazaki.[O2-07]

List of research achievements for application of Doctor of Engineering, Waseda University

Full Name： 余　雪萍　　seal or signature

Date Submitted(yyyy/mm/dd): 2023/1/30

種類別 (By Type)	題名、 発表・発行掲載誌名、　　発表・発行年月、　　連名者（申請者含む） (theme, journal name, date & year of publication, name of authors inc. yourself)
Academic papers	○"Tumor microenvironment regulation - enhanced radio - immunotherapy", Biomaterials Advances, July 2022, Volume 138, 212867. Xueping Yu, Xiupeng Wang, Lue Sun, Atsushi Yamazaki, Xia Li.
Academic papers	○"Tumor microenvironment-regulated nanoplatforms for the inhibition of tumor growth and metastasis in chemo-immunotherapy". Journal of Materials Chemistry B, March 2022, Volume 10, Issue 19, 3637-3647. Xueping Yu, Xiupeng Wang, Atsushi Yamazaki, Xia Li.
Lectures	"Tumor Microenvironment-Responsive Radiotherapy", The 43rd Annual Meeting of the Japanese Society for Biomaterials and the 8th Asian Biomaterials Congress,2021. Xueping Yu, Atsushi Yamazaki, Xiupeng Wang. [AO-2E22]
Lectures	"Manganese-based Tumor Microenvironment-Responsive Radiotherapy", Tsukuba Biomedical Engineering Forum 2022, 2022. Xueping Yu, Atsushi Yamazaki, Xiupeng Wang. [O-C-16]
Lectures	"Manganese-doped mesoporous silica for chemotherapy and immunotherapy", Annual Meeting 2022 of The Ceramic Society of Japan, 2022. Xueping Yu, Atsushi Yamazaki, Xiupeng Wang. [3F03]
Lectures	"Tumor microenvironment regulation-enhanced photo-immunotherapy", Tsukuba Biomedical Engineering Forum 2023, 2023. Xueping Yu, Xiupeng Wang, Atsushi Yamazaki.[O2-07]